Structure and interaction studies of beta-amyloid in the search for new lead compounds for the treatment of Alzheimer’s disease

A thesis submitted in partial fulfillment of the requirements for the degree

of

Master of Science in Bioinformatics and Computational Molecular Biology

(Coursework and Thesis)

of

RHODES UNIVERSITY, SOUTH AFRICA

Research Unit in Bioinformatics (RUBi)

DEPARTMENT OF BIOCHEMISTRY AND MICROBIOLOGY

Faculty of Science

By

ONKE MTINI

DECEMBER 2019

RUBi
Research Unit in Bioinformatics

RHODES UNIVERSITY
Where leaders learn

water & sanitation
Department:
Water and Sanitation
REPUBLIC OF SOUTH AFRICA

Abstract:

Alzheimer’s disease (AD) is the most devastating neurodegenerative disorder that effects the aging population worldwide. In this study three hypotheses of AD are explored, the β-amyloid cascade hypothesis, the β-amyloid metal binding hypothesis and the oxidative stress hypothesis are explored. In the first case compounds from the South African Natural Compounds Database (SANCDB) are docked to models of β-amyloid fibrils and the properties of these fibrils under pulling simulations are compared to a known small molecule disruptor of β-amyloid, wgx-50. In these simulations SANCDB compounds are identified that disrupt β-amyloid in a similar manner to wgx-50. In these simulations the disruption to the free energy of binding of chains to the fibrils is quantified. For metal binding and oxidative stress hypotheses, problems in simulation arise due to only fragments of β-amyloid being present in the Research Collaboratory for Structural Bioinformatics protein data bank (RCSB PDB), as determined from NMR experiments. In this work, β-amyloid is set up under periodic boundary conditions to simulate a fibril under reasonable computational time. Within these periodic boundary conditions, β-amyloid has been solvated in copper and zinc rich environments and diffusion of these metals around the fibrils has been explored. The localization of these metals (in simulation only using van der Waal’s and electrostatic terms) around the fibril has led us to explore other possible metal binding sites. Metal bound to the infinite fibril has been optimized at the QM/MM level and some of the reactive oxygen species in the presence of the fibril are quantified.

DECLARATION

I, **Onke Mtini**, hereby declare that this thesis submitted to Rhodes University is my original work and has never been submitted to this or any institution for a degree or diploma. All sources, references, and literature used during preparation of this work are properly cited and listed in complete reference to the due source.

……………………………… ………………………....

Signature Date

TABLE OF CONTENTS

LIST OF ABBREVIATIONS

ABBREVIATION	MEANING
ACH	Acetylcholine
AD	Alzheimer's disease
ADAS-COG	Alzheimer's disease assessment scale-cognitive subscale
ADME	Absorption, distribution, metabolism and excretion
AFM	Atomic force microscopy
AMP	Adenosine monophosphate
APOE*E4	Apolipoprotein E
APP	Amyloid precursor protein
ASO	Antisense oligonucleotides
AB	Beta-amyloid
BBB	Blood brain barrier
BDNF	Brain-derived neurotropic factor
BOMD	Born-Openheimer molecular dynamics
CHARMM	Chemistry at Harvard macromolecular mechanics
CNS	Central nervous system
CREB	Cyclic adenosine monophosphate response element binding
CSF	Cerebrospinal fluid
CU	Copper
DFT	Density function theory
DSV	Discovery studio visualizer
ETC	Electron transport chain
FE	Iron
GCP	Glutamate carboxypeptidase
HBA	Hydrogen bond acceptor
HBD	Hydrogen bond donor
IDE	Insulin-degrading enzyme
ISF	Interstitial fluid
KNIME	Konstanz information miner
LOGP	Lipophilicity partition coefficient
LRP	Lipoprotein receptor
MAP	Microtubule associated protein
MEM	Memantine
MM	Molecular mechanics
MMP	Matrix metalloproteinase
MRNA	Messenger Ribonucleic Acid
MUSCLE	Multiple sequence comparison by log expectation
NEP	Neprilysin
NFT	Neurofibrillary tangles
NGF	Nerve growth factor

NMDAR	N-Methyl-D-aspartate receptor
NMR	Nuclear magnetic resonance
NSAID	Non-steroidal anti-inflammatory drugs
PBC	Periodic boundary conditions
PES	Potential energy surface
PHF	Paired helical filament
PHM	Peptidylyine a-Hydroxylating Monooxygenase
PMF	Potential of mean force
QM	Quantum mechanics
RCSB	Research collaboratory for structural bioinformatics
ROS	Reactive oxygen specie
SIRNA	Small interfering Ribonucleic Acid
SPC	Simple point charge
SSNMR	Solid-state Nuclear magnetic resonance
TPSA	Topological polar surface area
US	Umbrella Sampling
VLDLR	Very low-density lipoprotein receptor
VMD	Visual molecular dynamics
WGX-50	N-[2-(3,4-dimethoxyphenyl) ethyl]-3-phenyl-arcylamide
WHAM	Weighted histogram analysis method
ZN	Zinc

LIST OF FIGURES

LIST OF AMINO ACIDS

AMINO ACID	1-LETTER	3-LETTER
ALANINE	**A**	**Ala**
ARGININE	**R**	**Arg**
ASPARGINE	**N**	**Asn**
ASPARTIC ACID (ASPARTATE)	**D**	**Asp**
CYSTEINE	**C**	**Cys**
GLUTAMIC ACID (GLUTAMATE)	**E**	**Glu**
GLUTAMINE	**Q**	**Gln**
GLYCINE	**G**	**Gly**
HISTIDINE	**H**	**His**
ISOLEUCINE	**I**	**Ile**
LEUCINE	**L**	**Leu**
LYSINE	**K**	**Lys**
METHIONINE	**M**	**Met**
PHENYLALANINE	**F**	**Phe**
PROLINE	**P**	**Pro**
SERINE	**S**	**Ser**
THREONINE	**T**	**Thr**
TRYPTOPHAN	**W**	**Trp**
TYROSINE	**Y**	**Tyr**
VALINE	**V**	**Val**

LIST OF TABLES

Acknowledgments:

Firstly, I would like to thank, Prof. Kevin A. Lobb, my supervisor for supporting me throughout the course of the year. Prof. Lobb is one of the best supervisors I have worked with, he is always available to provide assistance and give feedback, He also has great ideas and insightful opinions on my research.

I would like to thank Prof. Ozlem T. Bishop who has given me the opportunity to be part of the wonderful group of Bioinformaticians (RUBi). She is an inspiration to all of us in the unit.

I would will forever be thankful to my family who always support me throughout my life. To my mother Veronica N. Mtini and my father Mothela N. Mtini your guidance and everyday prayers have carried me thus far.

To my master's class, I am so glad that I have met each one of you, I would have not been able to get through this year without each one of you. You are all stars worthy to be recognized. Keep shinning and keep on being amazing souls the world needs each one of you.

Thank you so much to the Department of water and sanitation affairs for funding me.

Last but not least, I want to thank everyone at RUBi for all the support, words of encouragement and all the constructive feedback during presentations.

Chapter 1: Introduction

1.1 Alzheimer’s disease

The World Health Organization defines Alzheimer’s disease (AD) as a neurodegenerative disease of unknown aetiology, characterised by progressive memory and cognitive impairment. It accounts for 50% to 75% of all cases of dementia (Jia *et al*., 2016). Dementia is defined as the loss of cognitive function sufficient to interfere with social and occupational functioning (American psychiatric association, 1994). Alzheimer’s diseases (AD) is reported as the most frequent form of dementia in adults with at least 65 years of age (Riverol and Lopez, 2011). AD is thought to begin at 20 or more years of age before symptoms arise (Villemagne *et al*, 2013, Braak *et al*, 2011). Symptoms occur because nerve cells in parts of the brain involved in thinking, learning and memory have been damaged, persons in the final stages of AD require constant care and are bed-bound (Gaugler *et al*., 2019). Multiple risk factors have been identified, including female sex, age, low education, the apolipoprotein *(APOE*E4)* allele, smoking, obesity and diabetes mellitus (Jia *et al*., 2016). AD affects patients and their families on a mental, psychological, social and financial level, resulting in millions of households living below the poverty line (George-Carey *et al*, 2012). The *World Alzheimer report 2019*, reported that over 50 million people lived with dementia; Asia contributed the highest number of people and Africa had the least contribution in the global impact (Fig 1.).

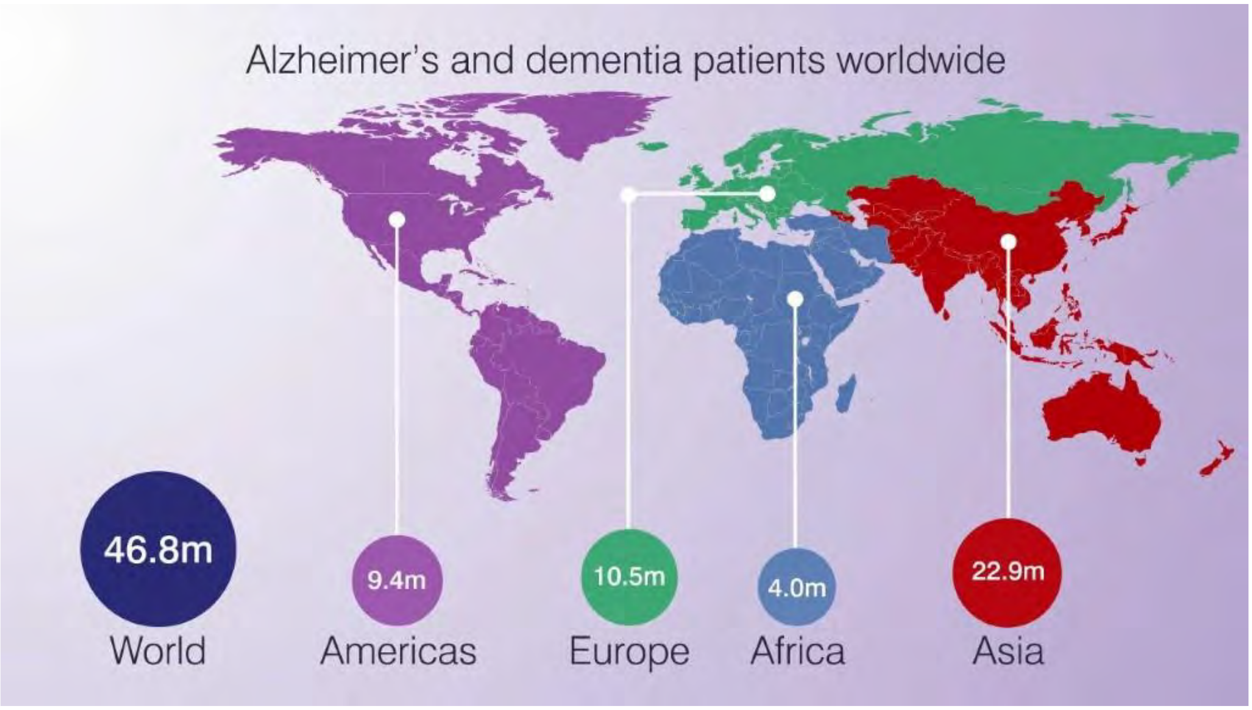

Figure 1: The number of people living with Alzheimer's disease and other dementia in the world. Data was extracted from *world Alzheimer's disease report 2015*.

The prevalence of AD worldwide was estimated to be as high as 24.2 million, considering that both developed and developing countries are rapidly aging, the frequency is expected to double every 20 years until 2040 (Ferri *et al*., 2005, Mayeux and Stern, 2012). North America and Western Europe have at age 60 years the highest prevalence of AD, followed by Latin America and China (Mayeux and Stern, 2012). In the United States of America, an estimated 5.8 million people are living with AD in 2019, This number includes an estimated 5.6 million people age 65 and older (Hebert *et al*, 2013). The number of cases and projected prevalence are similar in Europe (Thies and Bleiler, 2011, Wimo *et al*, 2003). This number is expected to grow rapidly as the population of Americans age 65 and older is projected to grow from 55 million in 2019 to 88 million by 2050 (Feng *et al*, 2016, West *et al*., 2014).

China has the largest population in the world, the number of Chinese aged 60 years and above was 159.89 million in 2008 (Jia *et al*., 2014). This suggest that in time it will have the greatest number of cases with AD in the world (Ferri *et al*., 2005). It was reported that the prevalence of AD was 3.21% among people aged 65 years and older, and more than 7 million Chinese people lived with AD in 2014 (Jia *et al*., 2014). The rapid growth of the elderly population poses tremendous challenges to the national health-care system and to the sustainable development of the national economy (Ji *et al*., 2015). The total prevalence of people living with AD in Africa was 2.76 million and 2.1 million of the afflicted individuals were from Sub-Saharan Africa in 2010 (George-Carey *et al*., 2012). There is limited research data concerning AD prevalence in South Africa (De jager *et al*., 2017). A study of 200 individuals was conducted in Bloemfontein, it identified 6% prevalence of AD in the black community assessed. Mixed-race people above the age of 65 years accounted for 8.6% of patients with possible AD, the 2016 world Alzheimer's report approximated that 4.4 million individuals above the age of 60 years living in South Africa, of this figure almost 187,000 living with AD. (Van der Poel *et al*., 2012, Ben-Arie *et al*., 1983, Alzheimer's disease international, 2016). This number is predicted to rise to 250,000 by 2030, with a concurrent increase in the number of people aged 60 years or older to 7 million (Alzheimer's disease international, 2016). This ensures that it is a necessary to determine not only the burden of AD in the country but also the services required to maintain, support and care for the affected individuals, their families and care-givers (De jager *et al*., 2017).

Economic costs of AD are significant for the health systems given the resources used to prevent, diagnose, treat and manage dementia (Castro *et al*., 2010). AD is the third most expensive disorder in the United States of America and with the aging society will likely become more significant

(Meek *et al*., 1998). The physical and psychological toll of care-giving can increase health risk for the care-givers and increase their own medical costs, this is because care-givers are an integral part for treatment of patients with AD (Zhu and Sano, 2006). The total worldwide societal cost was estimated to be US$ 315 million in 2005 with about 70% of cost occurring in developed countries (Wimo *et al*., 2010). The median survival of patients with AD is 9 years for persons diagnosed at age 65 years and 3 years for persons diagnosed at 90 years of age (Brookmeyer *et al*., 1998).
It is vital to study AD to improve pharmacological treatment and management of AD may help control health-care costs and improve the quality of life of patients and families.

1.2 Treatment of Alzheimer's disease

Despite the significant global health issue that AD poses, only five medical treatments have been approved. These treatments act to control symptoms rather than alter the course of the disease (Briggs *et al*., 2016). Although drug discovery, informed by preclinical models for AD, has resulted in large efforts to produce drugs that significantly alter the course of the disease, not a single drug proposed has achieved these outcomes (Salomone *et al*., 2012). Current clinical treatments of AD focus on the use of cholinesterase inhibitors, and drugs that target memantine, and tau. In Fig.2 various mechanisms have been proposed to explain the underlying pathology of AD. Current and future treatments are based on the modification of these pathways (Briggs *et al*., 2016).

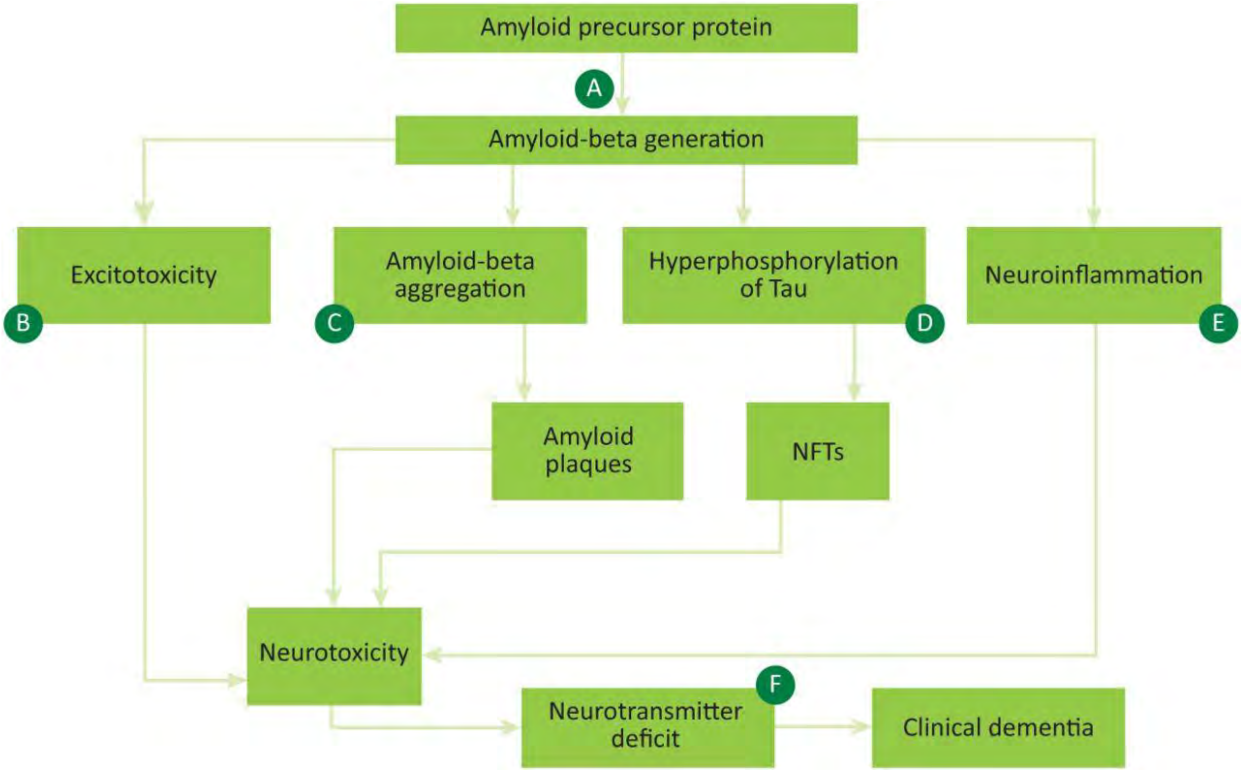

Figure 2: Aetiology of Alzheimer's disease with therapeutic targets (Briggs *et al*., 2016 open access).

1.2.1 Tau-targeted therapy

Tau neurofibrils are found in neurons, while β-amyloid (Aβ) fibrils are found as plaques in AD patients. Since tau is not directly toxic to cells and is a mediator to Aβ toxicity, reducing tau levels is a therapeutic approach to AD (Bi *et al*., 2011). Tau-targeted therapy treatment strategies uses agents to prevent hyperphosphorylation (a process that moves tau away from its microtubule stabilization function, allowing for formation of tau fibrils), as well as targeting microtubule stability and aggregation (Wischik *et al*., 2014). Tau expression can be reduced with small interfering RNA (siRNA) or antisense oligonucleotides (ASOs) (Congdon and Sigurdsson, 2018). Guo *et al*., 2018 found that in cell and animal models, siRNA reduced tau pathology and associated functional impairments. Phosphorylation of the tau protein affects its ability to bind tubulin and the adult form of tau promote microtubule assembly (Lindwall and Cole, 1984). In AD the pattern of phosphorylation changes as the disease progresses (Bi *et al*., 2011). The pattern of phosphorylation differs between tauopathies and familial tauopathies. In familial tauopathies the causative mutations induce conformational changes that make tau a more favourable substrate for specific kinases (Noble *et al*., 2013). Lithium and valproic acid can be used to inhibit tau phosphorylation (Tariot and Aisen, 2009). Epithilone D were identified as antifungal agents, however they were later discovered to be microtubules stabilizers (Bollag *et al*., 1995). Brunden *et al*., 2010 and Zhang *et al*., 2012, found that in preclinical testing, epithilone D increased microtubule numbers and decreased axons with abnormal morphology both in young and aged tau transgenic mice respectively. Methylene blue blocks the polymerization of tau in vitro (Bi *et al*., 2011). It achieves this by trapping the tau monomer in aggregation incompetent conformation (Panza *et al*., 2016, Wischik *et al*., 1996).

1.2.2 Cholinesterase inhibitors

Within the first generation of cholinesterase inhibitors was Tacrine, however with hepatoxic side effects (Manning, 1994). The most used agent currently is Donepezil (Briggs *et al*., 2016). Donepezil is prescribed at an initial dose of 5 mg in the evening, increased to 10 mg after one month (National institute for health and care excellence, 2011). It is recommended that patients should have electrocardiogram prior to commencing a cholinesterase inhibitor due to risk of sinus syndrome and other conduction abnormalities (Briggs *et al*., 2016). Cholinesterase inhibitors do not achieve the minimum clinically important drug-placebo of 4 points on the Alzheimer's disease assessment scale-cognitive subscale (ADAS-cog) (Schneider *et al*., 2014).

1.2.3 Memantine

Memantine (MEM) is a low-affinity voltage-dependent uncompetitive antagonist of N-Methyl-D-aspartate receptor (NMDAR) (Schneider *et al*., 2014). It blocks the NMDAR, and, due to being low-affinity is rapidly displaced from NMDAR. This displacement prevents prolonged receptor blockade and associated negative side effects on learning and memory that have been observed in high affinity NMDAR antagonists (Folch *et al*., 2018). MEM has adequate treatment thresholds of protection and tolerability. It has been shown mild to extreme AD benefits (Atri *et al*., 2013). Only when it is pathologically active, that's when it interacts with the channel. Preclinical data indicated that other receptors, including nicotinic, acetylcholine, and sigma-1 receptors could be blocked by MEM (Allgaier M and Allgaier C, 2014, Buisson and Bertrand, 1998).

1.3 Causes of Alzheimer's disease

At early stages of the disease, medical diagnosis of AD are extremely difficult (Zverova, 2019). This is due to extensive examinations to exclude any other probable dementia (Houmani *et al*., 2018). A clinical diagnosis is at times based on medical reports, neuroimaging, physical and neurological examination, neuropsychological assessment, collateral history from family and laboratory tests (Zverova, 2019). The exact cause of the disease is not yet evident. However, the available literature propose that AD is more than a neurodegenerative brain disorder (Zverova, 2018). There are numerous theories postulated that attempting to pinpoint the root cause and origin of AD, these include β-amyloid (Aβ) overproduction and clearance, acetylcholine deficiency, the tau hypothesis, brain-derived neurotropic factor (BDNF) deficit, mitochondrial dysfunction and neuroenergetic hypothesis, nerve growth factor (NGF) deficit, etc. (Zverova, 2019).

1.3.1 Acetylcholine deficiency

The first neurotransmitter to be identified was acetylcholine (ACh) (Loewi *et al*., 1921). It is used by all cholinergic neurons and is vital in peripheral and central nervous systems (CNSs) (Ferreira-Vieira, 2016). Since ACh has importance in cognitive processes, this suggests that the cholinergic system plays a vital role in the AD (Muir, 1997). It was thought that the depletion of cholinergic neurons and the resultant failure of dopaminergic production could be the main factor underlying psychiatric symptoms associated with AD (Martorana and Koch, 2014). Mesulam, 2013 supported this hypothesis, by demonstrating that dopamine efflux is significantly increased in M4 knockout mice. The findings reported by Mesulam suggest that cholinergic neuronal projections to the nucleus accumbens from laterodorsal tegmental nucleus and pedunculopontinus nucleus can control dopamine by M4 autoreceptor (Sarter *et al*., 2001).

1.3.2 Tau hypothesis

Tau proteins belong to the microtubule-associated family (Weingarten *et al*., 1975). They are involved in microtubule assembly and stabilization, in humans they are found in neurons (Gu *et al*., 2009). In the adult brain, six tau isoforms are produced from a single gene, located on chromosome 17q21 by alternative mRNA splicing (Delacourte *et al*., 2003). There are four repeats and two inserts in the CNS of the longest isoform, whereas the smallest isoform has three repetitions and no inserts (Mohandas *et al*., 2009). The tau hypothesis states that abnormal phosphorylation of tau results in the transformation of normal adult tau into paired helical filaments (PHF-tau) and intracellular neurofibrillary tangles (NFTs). The six tau isoforms are mostly found in a hyperphosphorylated state in paired helical filaments from AD (Mohandas *et al*., 2009). Mutations that change tau's function and isoforms expression result in hyperphosphorylation. The tau aggregation mechanism is not clear in the absence of mutation, but may result from hyperphosphorylation, the action of proteases or the presence of stabilizing polyanions, such as glycosaminoglycans (Iqbal and Grundeke-Iqbal, 2008). Hyperphosphorylated tau disassembles microtubules and sequesters normal tau, microtubule associated protein1 (MAP 1), MAP 2, and ubiquitin into tangles of PHFs. This insoluble structure damages cytoplasmic functions and interferes with axonal transport, which leads to cell death (Mudher and Lovestone, 2002).

1.3.3 Brain-derived neurotropic factor deficit

BDNF is important for the survival of entorhinal cortex, whose early impairments leads to the initial loss of short-term memory in AD (Nagahara *et al*., 2009). BDNF deficiency stems from a number of different factors, including metal dyshomeostasis, lack of nerve growth factor (NGF) support, degradation of usable Aβ monomers, and the presence of harmful Aβ oligomers (Zimbone *et al*., 2018). The cyclic AMP reaction element-binding protein (CREB) cannot be triggered by Aβ monomers and thus prevent BDNF transcription and release (Zimbone *et al*., 2018).

1.3.4 Mitochondrial dysfunction and neuroenergetic hypothesis

Mitochondria are genetically inherited intracellular organelles with critical roles such as energy metabolism and second messenger signalling through to programmed cell death (Ortiz and Swerdlow, 2019). Several of the first hints to mitochondria dysfunction in AD, were obtained from observations of regional hypometabolism findings in AD subjects on brain images (Foster *et al*., 1983). AD brains appear to account for hypometabolism of glucose by switching into amino and fatty acids as an alternative sources of energy (Teledo *et al*., 2018). Such findings certainly suggested improvements in the fuel metabolic pathways in AD (Ortiz and Swerdlow, 2018). It is thought that the observed metabolic changes consider impaired mitochondrial functions (Ortiz and Swerdlow, 2019). Mitochondrial dysfunction may play a significant role in increasing AD susceptibility accompanying aging (Chetelat *et al*., 2013). The aging brain has lower energy consumption, lower glucose usage and decreased respiratory capacity (De Santi *et al*., 2007). Mitochondrial electron transport chain (ETC) complexes I and IV functions decrease with age (Navarro and Boveris, 2007). A main pathogenic finding is that Aβ accumulation in the OXYS rat model is followed by mitochondrial dysfunction (Stefanova *et al*., 2019). A series of experiments found a more direct link between mitochondrial function and aging, whereby dampening the development of mitochondrial ROS increased the lifetime of mice (Schriner *et al*., 2003).

The neuroenergetic theory attempts to explain the AD process as a consequence of persistent reduction in usable metabolizable energy resources, mainly CNS glucose (Blonz, 2017). This age-related, gradual reduction in the scope of metabolic implications is compatible with current theories epidemiological observations (Quistorff *et al*., 2008)

1.3.5 Amyloid cascade hypothesis

The Aβ cascade hypothesis was proposed in 1992 by Hardy and Higgins (Hardy and Higgins, 1992). They postulated that accumulation of $A\beta_{42}$, is the starting point for neurodegeneration (Yoon and Ahn Jo, 2012). Aβ is produced during neuronal activity from amyloid precursor protein (APP) (Bero, *et al*., 2011). In non-pathological conditions, APP is cleaved off by α-secretase which precludes formation of Aβ, and the resulting carboxy-terminal fragment is then cleaved by γ-secretase (Chow *et al*., 2010). If APP is cleaved by β-secretase 1 instead of α -secretase, the subsequent γ-secretase cleavage will result in soluble monomeric Aβ (Zheng *et al*., 2013). The most common soluble monomeric isoforms of Aβ are $A\beta_{40}$, $A\beta_{38}$, and $A\beta_{42}$ (Morris *et al*., 2014).

Aβ_{42} has two additional amino acids, making it more hydrophobic than other isoforms and, thus, capable of forming insoluble aggregates (Dawkins and Small, 2014).

This pathway and these enzymes have been the subject of scientific research for a long time in order to produce AD drugs. In the light of the weight of previous studies of Aβ, a new proposal regarding Aβ plaque formation has recently appeared in the literature. This concept leans towards Aβ clearance rather than synthesis thereof (Yoon and Ahn Jo, 2012). There are various processes through which Aβ may be cleared from the brain; these include both enzymatic and non-enzymatic pathway (Tarasoff-Conway., 2015). The latter pathway includes bulk flow of the interstitial fluid (ISF) into cerebrospinal fluid (CSF) followed by ISF drainage pathway through perivascular basement membranes, the uptake by microglial or astrocytes phagocytosis, and the transport across the blood vessel walls into the blood vessel which is mediated by a series of clearance receptors such as low-density lipoprotein receptor related protein 1 (LRP1), very low-density lipoprotein receptor (VLDLR) and P-glycoprotein localized predominantly on the abluminal side of the cerebrum (Shibata *et al*., 2000, Deane *et al*., 2004). While the enzymatic clearance involves several proteases, including neprilysin (NEP), insulin-degrading enzyme (IDE), matrix metalloproteinase (MMP)-9 and glutamate carboxypeptidase II (GCPII) (Yoon and Ahn Jo, 2012).

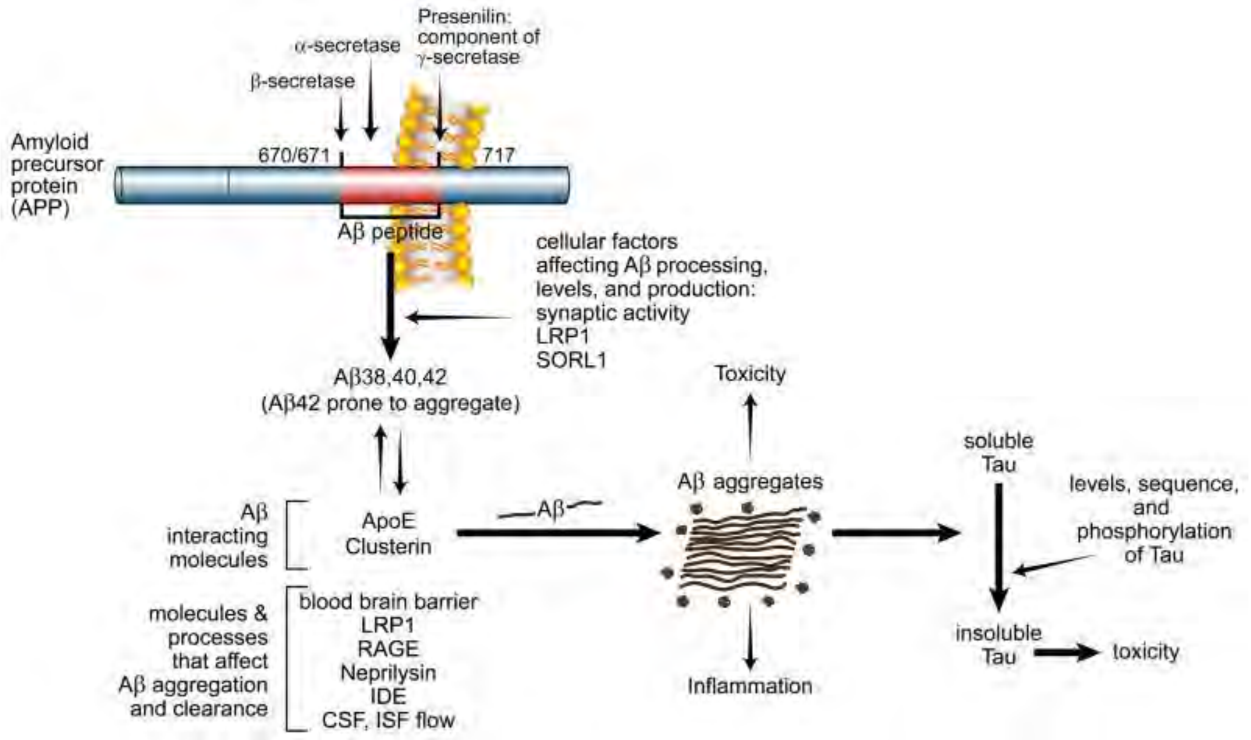

Figure 3: Model of AD pathophysiology (Holtzman *et al*., 2012).

Figure 3 summarizes some of these discussed hypotheses. All computational studies performed in this thesis are based on the amyloid cascade hypothesis that Aβ is the target for AD drug design.

1.3.5.1 Beta-amyloid peptides

APP is a neuron's transmembrane protein that alters the structure and function of synapse in a cultured hippocampal neuron. APP has three major isoforms APP_{695}, APP_{751}, and APP_{770} that are abundant in the hippocampus and cerebellum. There are multiple varying pathways that exist for APP proteolysis. All of the pathways may be categorised in to two pathways namely, the amyloidogenic pathway which leads to a production of Aβ peptides, and the non-amyloidogenic pathway (Priller *et al*., 2006).

It is proposed that about 90% of secreted peptides are $A\beta_{40}$, while $A\beta_{42}$ accounts for less than 10% of secreted Aβ. However, $A\beta_{42}$ is more neurotoxic as it aggregates faster. The sequence of $A\beta_{42}$ is:

DAEFR^{5}HDSGY^{10}EVHHQ^{15}KLVFF^{20}AEDVG^{25}SNKGA^{30}IIGLM^{35}VGGVV^{40}IA. $A\beta_{40}$ has the same sequence as $A\beta_{42}$, but the last two residues are not present. $A\beta_{42}$ and $A\beta_{40}$ are fitted with same hydrophilic N-terminal from residue 1 to 15. Residues 17-21 are the central hydrophobic center, and residues 22-28 are included in the turn region. In $A\beta_{42}$ and $A\beta_{40}$, the hydrophobic C-terminal has 13 residues 30-42 and 11 residues 30-40 respectively (Querfurth and Laferla, 2010).

The structural details of $A\beta_{42}$ are poorly defined, despite rigorous efforts (Lührs *et al.*, 2005). The high misfolding propensity of $A\beta_{42}$ fibrils show structural and morphological heterogeneity, limiting subsequent analyses (Masuda *et al.*, 2009). In this thesis three structures are used with Protein Data Bank (PDB) identification (ID) 2MXU ($A\beta_{11-42}$), 2BEG ($A\beta_{17-42}$), and 2NAO ($A\beta_{1-42}$). All these amyloid fibril atomic models are based on liquid NMR (2NAO) or solid-state NMR (ssNMR). 2MXU has 12 S-shape chains in fibrillar state and contains a triple parallel-β-motif (Xiao *et al.*, 2015). The 2BEG is a U-shaped pentamer, forming intermolecular β-sheets structures between neighboring peptides in this PDB (Okumura and Itoh, 2016). The 2NAO is composed of two molecules per fibril layer, with residues 15-42 forming a double-horseshoe-like cross-β-sheet (Walti *et al.*, 2016).

1.4 β-amyloid as a drug target

Amyloid plaques in the brain are one of the major symptoms of AD, these consist mainly of fibrils of the amyloid-β peptide (Monsonego *et al.*, 2003). There are various targeting candidates that have been proposed to disrupt or prevent Aβ aggregation. These include antibodies, peptide inhibitors, and non-peptide small molecules (Fan *et al*., 2015). A hypothesis that the interaction between resveratrol derivatives and Aβ could shift the equilibrium of Aβ polymorphism from β-sheets into disordered monomers was proposed by Riviere *et al*. in 2002. This was due to in vitro studies that have suggested some polyphenolic compounds from red wine and green tea may bind to Aβ, inhibit Aβ aggregation, and destabilize preformed fibrils (Ono *et al*., 2003, Hamaguchi *et al*., 2010). *In vivo* experiments on an Alzheimer's mouse model reported a lower level of amyloid plaque and improved memory and cognitive ability after feeding of red wine (Hamaguchi *et al*., 2010). Curcumin and ibuprofen have also been shown to inhibit the Aβ peptide aggregation in vitro and in vivo (Choi *et al*., 2014). Similarly, β-sheet breakers have been identified, which can inhibit Aβ peptide aggregation (Lemkul *et al*., 2010). Arginine was also observed to have a role as an aggregation suppressor to increase the solubility of the Aβ peptide in aqueous medium (Das *et al*., 2001). It was proposed that a hybrid peptide inhibitor containing an aromatic ring and arginine may be good candidates to inhibit Aβ peptide aggregation.

1.4.1 Drugs that interact with fibrils

N-[2-(3,4-dimethoxyphenyl) ethyl]-3-phenyl-arcylamide (wgx-50) is a potent drug candidate for AD that has been developed in recent years (Tang *et al*., 2013). Wgx-50 was shown to pass through the blood brain barrier (BBB), boosting mice's cognitive ability, and decrease Aβ oligomer aggregation in the cerebral cortex. These conclusions were drawn from performing in vivo experiments, such as pharmacokinetic assays, cognitive abilities tests, and immunohistochemical analysis of the brain section of the transgenic mouse model (Gu and Wei, 2017). Wgx-50 was also shown to disassemble Aβ oligomers, inhibit Aβ-induced neuronal apoptosis, and has anti-inflammatory effects by counteracting Aβ-triggered microglial overaction. In vitro experiments, such as atomic force microscopy (AFM) of Aβ oligomers and cell apoptosis assay provided proof for these conclusions (Gu and Wei, 2017). Tang *et al*., 2013 found that wgx-50 also inhibits Aβ peptide-induced ion conductance. They observed this by pre-treating neurons with wgx-50 before adding Aβ amyloids, this inhibited accumulation of calcium ions (Ca^{2+}) at the cytoplasmic side and reduced neuronal calcium toxicity. Fan *et al*., 2015 found that wgx-50 can disrupt the Aβ protofibril structures by breaking the Aspartic acid 23, Lysine 28 (Asp23-Lys28) salt bridges found in the interior of the Aβ protofibrils.

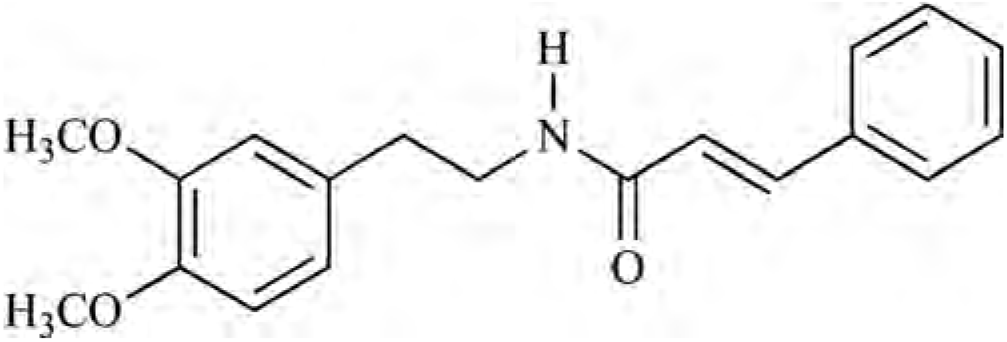

Figure 4: Molecular structure of wgx-50, obtained from Hou *et al*., 2017.

Non-steroidal anti-inflammatory drugs (NSAIDs) have been identified as Aβ aggregation inhibitors (Azam *et al*., 2018). This is due to AD brain is marked with chronic inflammatory status of the activated glial cells and elevated release reactive oxygen species (ROSs), inflammatory cytokines, chemokines and organisms (Dumont and Beal, 2011). The correlation between AD and inflammation indicates that NSAIDs may be helpful AD therapy (Deardorff and Grossberg, 2016). Gilgun-Sherki *et al*., 2006, reported that NASIDs minimize the threat of AD, prolong dementia development, decrease the frequency of mental symptoms. These can also change the conformation of anti-aggregation of Aβ peptides exerting anti-aggregation and cause the development of amyloid-binding proteins (Gasparini *et al*., 2004).

1.4.2 Challenges generated by β-amyloid

Amyloid plaques are accumulations of molecules in the extracellular space of the brain (Holtzman *et al*., 2012). The principal component of these plaques is the Aβ peptide (Golde *et al*., 2000). Amyloid plaques are widely accepted as dynamic and serve as a reservoir of different forms of Aβ and other bioactive molecules (Haass and Selkoe, 2007). They can induce many downstream changes, including microgliosis and dystrophy (Shankar *et al*., 2008). Over the past two decades, therapeutic strategies have been developed aiming to reduce amyloid plaques (Xiong *et al*., 2019). These attempts, however, have failed to show substantial efficacy in clinical trials (Wang *et al*., 2014) even though they yielded promising effects in mouse models (Cummings *et al*., 2014).

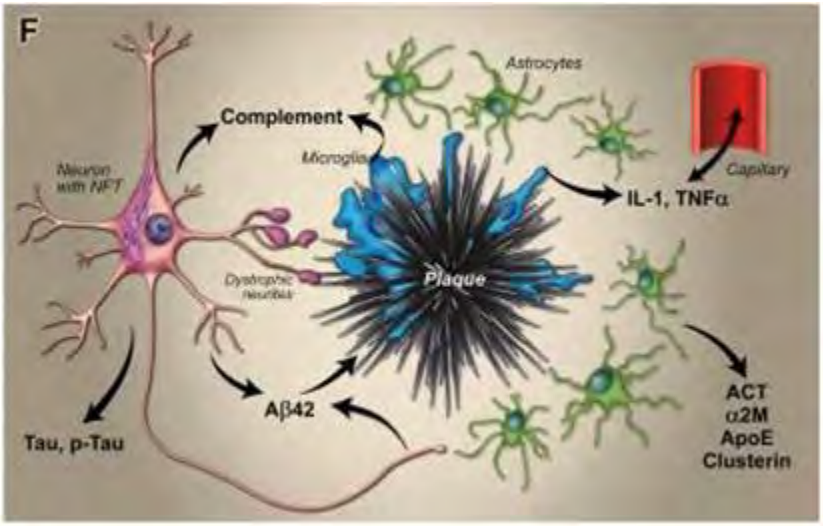

Figure 5: Aβ aggregates in the extracellular space of the brain to form plaques (Holtzman *et al*., 2012).

Aβ is capable of generating reactive oxygen species (ROS) in conjunction with certain redox-active transition metal ions (Mayes *et al*., 2014). Hung *et al*., 1999, reported direct production of two key ROS, hydrogen peroxide (H_2O_2) and hydroxyl ($\cdot OH$), during Aβ *in vitro* incubation. They also stated that Aβ binds strongly to Copper (Cu), Iron (Fe) and Zinc (Zn) ions and that when bound, Aβ reduces Cu(II) to Cu(I) and Fe(III) to Fe(II), and the resulting complex of peptide-metal ions is redox-active. This is essential because Cu(I) and Fe(II) ions will reduce molecular oxygen to H_2O_2 and (·OH) when bound to Aβ (Mayes, 2014). Higher levels of these metals are identified in the brains of individuals with AD located in the amyloid plaque deposits (Lovell *et al.*, 1999).

1.5 Metal binding to β-amyloid

Metals are thought to play a role in AD's pathogenesis (Atwood *et al.*, 1999). Cu and Zn have been documented to accumulate in and around amyloid plaques. (Sayre *et al.*, 2000, Dong and Chen, 2003). Aβ possesses selective high and low affinity Cu^{2+} and Zn^{2+} binding sites (Atwood *et al.*, 1998). The sites mediate aggregation of Aβ by interacting with Zn^{2} and Cu^{2+} in vitro (Bush *et al.*, 1994). Curtain *et al.*, 2001 proposed a model of monomer Aβ binding to a Cu ion either through three histidine and one tyrosine residue or through a bridge histidine for aggregation Aβ. They used electron paramagnetic resonance and nuclear magnetic resonance (NMR). Dong *et al.*, 2003 showed that Zn and Cu ions were coordinated through a histidine at the end of the Aβ sequence in the N-terminal. They used Raman spectroscopic analysis of senile plaque cores for this demonstration.

1.5.1 Mechanism of copper binding to β-amyloid

Cu homeostasis can be compromised under disease conditions, resulting in Cu being more loosely bound Cu, which is vulnerable to ROS production (Simon *et al.*, 2012). This is thought to be the case in AD (Hung *et al.*, 2010), where there is high concentration of Cu found in amyloid plaques (Sayre *et al.*, 2000). Cu-Aβ has been shown to be redox competent and capable of producing ROS catalytically in the presence of physiological concentrations of reductant such as ascorbate (Hureau and Peter 2009). The binding of either Cu ion to the Aβ peptide is highly dynamic and different binding conditions are in rapid exchange (Hureau, 2012). The main binding model for Cu(I) for instance is a diagonal coordination to the Nδ of the two His 13 and His 14 (Jesse *et al*., 2004). In physiological pH, Cu(II) is bound to Aβ in two different coordination sites (Furlan *et al*., 2015). In the major form, Cu(II) is bound to four equatorial ligands. In the minor form, the Cu(II) equatorial ligands are NH_2 (Asp 1), the deprotonated amide N of Asp 1-Ala 2 bond, the adjacent C=O from the Ala 2-Glu 3 bond, and one of the His side chains (Hureau, 2012). This is shown in Fig.6.

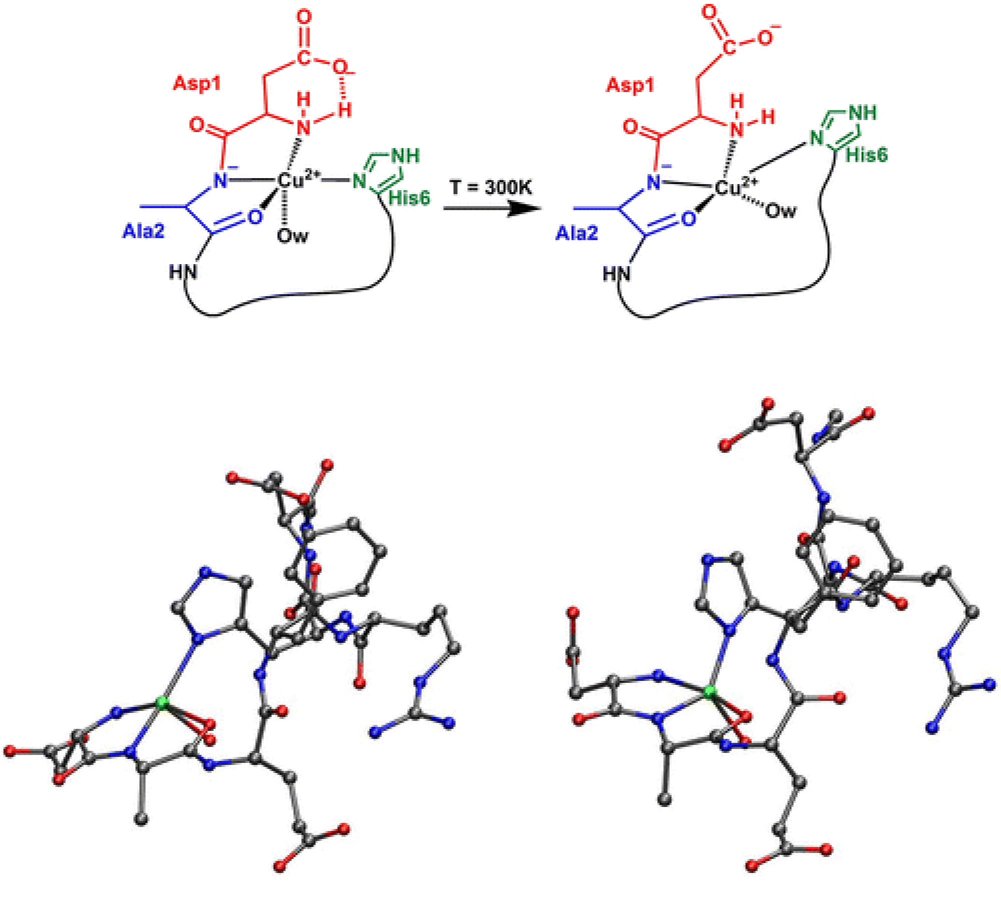

Figure 6: Schematic representation of high pH model of Cu^{2+}- Aβ (Furlan *et al*., 2012).

1.5.2 Mechanism of zinc binding to β-amyloid

The first Zn binding site of Aβ is located in the N-terminal part (Talmard *et al*., 2007). Alies *et al*., 2016 proposed the model shown in Fig.7 regarding Zn(II) binding to Aβ. The main coordinating sphere of Zn(II) near pH 7 is [$2N_2O$], consisting of two His residues and two carboxylate groups. The carboxylate groups are predominantly binding by Glu 11, while the other three carboxylate side chains share the fourth position of coordination, with Asp 1 preference (Alies *et al*., 2016).

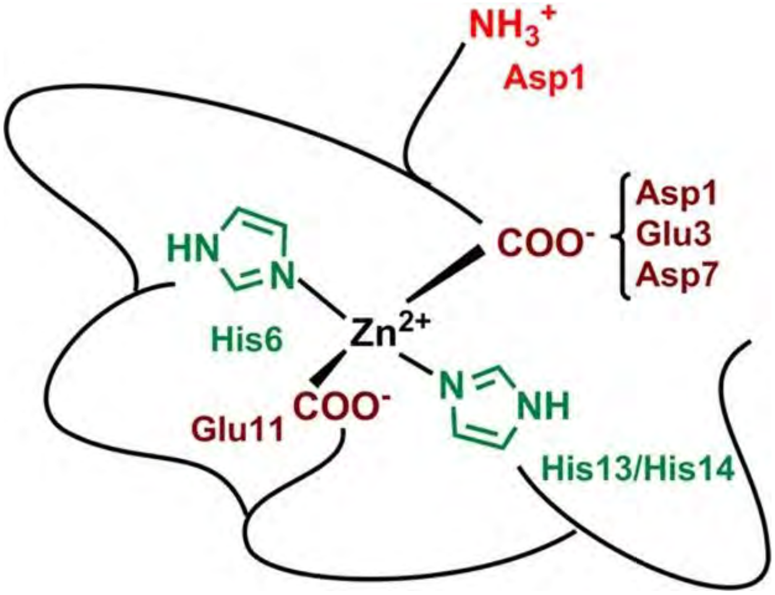

Figure 7: Proposed Zn(II) binding site in Aβ, Alies *et al*., 2016.

1.6 SANCDB compounds in drug discovery

The South African natural compounds database (SANCDB), is a free, online database containing compounds isolated from the plant and marine life in and around South Africa. The database is curated and fully-referenced containing compound information of more than 700 natural products (NPs). SANCDB has been developed to assist with *in silico* drug discovery (Hatherley *et al*., 2015). NPs and their derivatives have been recognized for many years as a single most productive source of leads for the development of drugs, since they have a wide range of diversity of chemical structures and moeities (Harvey, 2008). Thus, it is believed that a large number of new potential drugs are within the space held by all NPs. However, isolating all the NPs and screening them is extremely unpractical, due to the expense and time required to do so (Strohl, 2000).

Problem statement

The *World Alzheimer report 2015*, reported that over 46.8 million people live with dementia. Alzheimer's diseases (AD) is reported as the most frequent form of dementia in adults with at least 65 years of age. Currently there is no cure for AD or a way to stop or slow its progression. The only available forms of treatment are for patients with mild to moderate AD. Patients in the final stages of AD require constant care and are bed-bound till ultimate fatality. AD is a global health priority, which does not only affect patients diagnosed with the disease, but also their families on a personal, social, psychological and financial level. AD has the propensity to drive millions of households below the poverty line.

Drug discovery in AD has attempted in the last decade to develop disease modifying drugs with the help of preclinical models, but none of these drugs has succeeded. This failure is attributed to lack of clarity in terms of the cause of AD.

Recent studies have showed that simulation of copper binding to the Aβ oligomer, showed the residue that copper interacts most with (this interaction in the simulation is only from the set van der Waal's and electrostatic terms) is Met 35. Other studies have also described a relationship between Met 35 and Cu ions, and their influence on neurotoxic activity of Aβ. Thus, investigating different Cu binding sites could offer more insight into the interaction between Aβ and Cu and the effect this relationship has on aggregation and fibril formation.

Hypothesis

High throughput screening of compounds against Aβ_{42} targets will result in hits able to destabilize the Aβ aggregate formation. Understanding the thermodynamics of destabilizing of these aggregates and features contributing to their stability will allow the fine-tuning of therapeutic agents. Understanding of the competitive Cu and Zn binding to Aβ and the potential energy surface associated with ROS will enable us to target these sites in docking. Small molecules that interact with fibrils yet do not disrupt the aggregate, may still be useful in preventing access of O_2 to these metal-binding sites

Aims

The aim of this research is to use *in silico* methods such as, molecular docking to screen for compounds that display destabilizing activity against Aβ aggregates. Additionally, use molecular dynamics, as well as center-of-mass pulling and umbrella sampling to study factors that influence destabilizing effects of these compounds. A secondary aim is to characterize metal binding to the Aβ aggregate, and to perform QM/MM molecular studies for quantification of the interaction between copper and Aβ aggregates.

Goals/objectives

To successfully execute the proposed research, the following objectives will be carried out:

1. High throughput virtual screening of SANCDB compounds against the Aβ oligomer (PDB ID: 2MXU, 2BEG and 2NAO) using Autodock Vina
2. Dock the potential drug candidate Wgx-50 to 2MXU, 2BEG, and 2NAO using Autodock Vina

3. Study the thermodynamics of peptide dissociation from core of 2BEG protofibril at physiological temperature in the presence of SANCDB top hits and Wgx-50.
4. This work seeks to explore Cu (based only on van der Waal's parameters (Carlisle MSc, 2018) methionine binding sites, and other experimentally reported binding sites
5. Investigate and determine how binding affects the Aβ structure
6. Determine the mechanism of formation of H_2O_2 by Cu-Aβ (Mayes *et al*., 2013)
7. Since existing literature depends on a model subset of the full system for 4-6, in this study a full system will be used

Chapter 2: Molecular docking

2.1 Introduction

Molecular docking is a computational procedure that is utilized to predict non-covalent binding of a small molecule (ligand) into a binding site of a macromolecule (receptor). This provides us with the ability to characterize the behavior of small molecules in the binding site of target proteins as well as to elucidate fundamental biochemical processes (McConkey *et al*., 2002). The aim of molecular docking is to predict both the bound conformation (the docking pose) and the binding affinity using computational methods (Trott *et al*., 2010). The prediction of binding of small molecules to proteins is an important part of rational drug design and drug development. Docking programs usually use a scoring function to approximate the standard chemical potentials of the system (Gilson *et al*., 1997). The purpose of the scoring function is to delineate the correct pose from incorrect pose, thereby identifying active and inactive compounds in a reasonable computational time (Cheng *et al*., 2012). Scoring functions involve estimating, the binding affinity and they can be divided into empirical, force-field-based and knowledge-based scoring functions (Kitchen *et al*., 2004). The scoring functions takes a pose as input and returns a number indicating the likelihood that the pose represents a favorable binding interaction. Most scoring functions are physics-based relying on molecular mechanics force fields that estimate the energy of the pose in which a low energy indicates a stable system and thus a likely binding interaction. An alternative approach is to derive a statistical potential for interactions from a large database of protein-ligand complexes such as Protein Data Bank (Halperin *et al*., 2002).

Successful docking methods are able to effectively search the high dimensional search spaces and apply scoring functions that correctly rank docking candidates. However, there are limitations to molecular docking. The major limitation is due to the lack of confidence on the ability of scoring functions to give accurate binding energies (Sethi *et al*., 2019). This stems from the fact that intermolecular interactions terms, such as solvation effect and entropy change are hardly predicted accurately (Yuriev *et al*., 2009). Halogen bonding and guanidine-arginine interactions are some intermolecular interactions which are rarely considered in scoring functions despite being proven to be of significance (Ren *et al*., 2014, Yang *et al*., 2015). Water molecules in the binding pocket during docking process, are still yet to be dealt with accurately (Sethi *et al*., 2019). This inaccuracy is attributed to two challenges. Firstly, the x-ray crystal structures lack the coordinate information of hydrogen as a consequence of inefficient scattering by smaller atoms (Spyrakis and Cavasotto, 2015). Secondly, there is no reliable theoretical approach available to accurately determine how water molecules are affected by ligands and how strong this effect is (Spyrakis and Cavasotto, 2015).

There are also limitations tailored to a specific scoring function, for instance in knowledge-based scoring functions is their reliance on the inverse Boltzmann relationship (Prieto-Martínez, *et al*., 2018). Whereby a reference state needs to be defined in which pairwise potentials are zero. Defining such state is not trivial and it can impact the results significantly (Muegge, 2000). There have been attempts to improve the predictive power which led to hybrid approaches (Debroise *et al*., 2017). In force-field-based scoring functions is the entropic contributions of solvation which cannot be accounted for (Kitchen *et al*., 2004). Additionally, these approaches usually involve long computing times and need distance cut-offs which decreasing the accuracy of long-range effects (Meng *et al*., 2011). While for empirical scoring functions is the fact that they are derived from individual protein-ligand complexes and heterogeneous data in training sets (Pason and Sotriffer, 2016). Although, empirical scoring functions are computed much faster than the force-field-based scoring functions and yield reasonable binding energy predictions (Murray *et al*., 1998).

Docking is useful in performing virtual screening of large libraries of compounds. Since it can rank the results and propose structural hypotheses on how the ligands inhibit the target which is invaluable in lead optimization during computer-assisted drug design (Morris *et al*., 2008).

Over the last two decades, more than 60 different docking tools and programs have been developed for both academic and commercial use such as DOCK (Venkatachalam *et al*., 2003), AutoDock (Österberg *et al*., 2002), FlexX (Rarey *et al*., 1996), Surflex (Jain, 2003), Genetic Optimization for Ligand Docking (GOLD) (Jones *et al*., 1997), AutoDock Vina (Trott and Olson 2010), MOE-Dock (Corbeil *et al*., 2012), UCSF Dock (Allen *et al*., 2015), and many others. The most used docking programs are GOLD (Jones *et al*., 1997) and AutoDock (Goodsell *et al*., 1996).

In this chapter AutoDock Vina was used, it is an open source and is currently used by many groups worldwide for docking and virtual screening molecular (Quiroga and Villarreal, 2016). It is the successor of Autodock 4, a highly successful docking program (Trott and Olson 2010, Morris *et al*., 2009). However, AutoDock Vina is a different program and uses a different scoring function and a global optimization algorithm. It is two orders of magnitude faster and has shown similar or improved accuracy (Trott and Olson, 2010, Chang *et al*., 1955). For the estimation of ligand-receptor affinity, AutoDock Vina uses an empirical scoring function which is inspired by the X-score function (Wang and Lin, 2013). According to the authors, Trott and Olson the nature of the scoring function is used in AutoDock Vina is “more of a machine learning than a physics-based function”.

AutoDock Vina is employed in this study to estimate the binding affinity and generate starting conformations of Aβ-ligand complexes for use in pulling and umbrella simulations. As such it is the first stage of virtual screening for potential drug candidates from the SANCDB.

2.2 Drug-likeness based on molecular properties

During the drug discovery process, medicinal chemists investigate what the biological impact will be of the physicochemical parameters of potential drugs; these physicochemical parameters in turn are dependent on structural features related to drug-likeness properties (Mignani *et al*., 2018). The objective is to differentiate between the medicinal potential of-high-quality drugs and non-drugs, both of which may in theory be active against a particular target. The main developmental properties analyzed are, molecular mass, number of rotatable bonds, number of aromatic rings, number of heavy atoms, number of chiral centers, lipophilicity partition coefficient (logP), polarity, number of hydrogen bond donors (HBD) and hydrogen bond acceptors (HBA) (Segall, 2012).

Lipinski *et al*., 2001 pointed out that leads obtained through high-throughput screening tend to have higher molecular weights and greater lipophilicity. Lipinski's Rule of 5 was developed to set drug-ability guidelines for new molecular entries. The Rule of 5 predicts that poor absorption or permeation is more likely when there are more than 5 HBDs and 10 HBAs, molecular weight greater than 500 g/mol, and the calculated logP is greater than 5 (Benet *et al*., 2016). This Rule of 5 is only valid for compounds that are not substrates for active transporters (Lipinski *et al*., 1997).

2.3 Molecular Docking to Aβ

β-amyloid and amyloid fibril are peptides that do not have any active site or specific activity region. Thus, the blind docking approach is applied to identify possible binding regions (Balaji *et al*., 2013). Theoretical methods have been used for several years to expand the experimental work and increase the rate of Alzheimer's drug design process. However, Aβ aggregation is a challenging area and the related information is difficult to gather using traditional experimental techniques. Hence, molecular docking and virtual screening are very helpful (Teplow *et al*., 2006).

Teper *et al*., 2006, used docking studies of hydroxycholesterol derivatives to find the different compounds that can bind large regions of the Aβ surface, encompassing nearly half of the Aβ sequence. On the other hand, Braymer *et al*., 2011 investigated the binding of stilbene derivatives to Aβ monomers. They reported that these compounds could bind to polar N-terminal residues that are believed to bind to metal ions and contribute to neurotoxicity. Liu *et al*., 2006 performed MD simulations prior to molecular docking to generate Aβ conformations that represent the solution conditions better. The compound that Liu *et al*., 2006 examined was bound to a large portion of the Aβ surface. However, this compound did not inhibit β-strand formation. They concluded that the compound's inhibitory mechanism is involved in interfering with interpeptide hydrogen bonding. Thus, in the context of Aβ, it may be seen that docking is an extremely useful tool.

In this study, structural based virtual docking approach was employed to screen a library of natural products from South Africa (the SANCDB) against 3 $A\beta_{42}$ protofibril structures.

2.4 MUSCLE

Multiple alignments of proteins sequences are important in many applications. They are used in phylogenetic tree estimations, structure prediction and critical residue identification (Edgar, 2004). In this thesis we employed multiple sequence comparison by log expectation (Edgar, 2004), to differentiate between the three Aβ aggregates.

MUSCLE uses two distance measures for a pair of sequences. The first is a *k*mer distance for an unaligned pair, and the other is the Kimura distance for an aligned pair (Edgar, 2004). The *k*mer distance is derived from the fraction of *k*mers in common in a compressed alphabet. Thus, given a pair of sequences, it computes the pairwise identity and convert it to an additive distance estimate. While applying the Kimura correction for multiple substitutions at a single site (Kimura, 1983). MUSCLE can achieve both better average accuracy and better speed than CLUSTALW or T-Coffee, however this depends on the chosen options. (Edgar, 2004).

2.5 Methods

2.5.1 Receptor preparation

The three 3D structural representatives of $A\beta_{42}$ fibrils obtained through solid-state nuclear magnetic resonance (ssNMR) were retrieved from the Protein Data Bank (RCSB.org). PDB ID: 2MXU (Xiao *et al.*, 2015), 2BEG (Lührs, *et al.*, 2005), 2NAO (Wält, *et al.*, 2016). Since the 2NAO structure contains two distinct Aβ filaments, we docked to one filament with chains A-C. The receptors were prepared using a script (*prepare_receptor4.py -r filename*) from the Autodock Tools suite of software. The script prepares the 3D structures of $A\beta_{42}$ fibrils by removing water, adding hydrogens, merging non-polar hydrogen, adding Gasteiger charges, and saving the receptors in pdbqt file format.

2.5.2 Ligand preparation

The potential drug candidate Wgx-50 was sketched and the geometry optimized using Discovery Studio Visualizer version 4.5 based on the structure by (Hou *et al*., 2017). Seven hundred and twenty-eight natural compounds were obtained, already minimized from SANCDB (Hatherlry *et al*., 2015). These compounds together with wgx-50 were then prepared for docking using a script (*prepare_ligand4.py -l filename*) also from Autodock Tools suite. This script sets correct atom types and charges, defines the relevant torsions for conformational searching, and saves the ligands in pdbqt file format.

2.5.3 Docking

The docking simulations were performed with the SANCDB compounds as ligands and the three Aβ_{42} fibrils as targets. Vina input scripts were generated for each SANCDB compound to dock to these targets (the vina input scripts were generated from within a controlling python script) and these vina scripts were used as input to AutoDock Vina (Trott and Olson, 2009). To validate the dockings, the docking simulation was performed in duplicate for each of the three Aβ_{42} fibrils as targets. Dock A (2MXU), and Dock C (2NAO) were targeted docking focusing on the eighth chain (chain H) and final chain (Chain C) of the aggregates respectively. The last chain is the most variable chain of the Aβ_{42} fibrils (Carlisle, 2018). Thus, docking to the last chain could assist in discovering whether the compounds would bind to the variable chain, such that it prevents further aggregation of another monomer to the Aβ_{42} fibrils (Carlisle, 2018). Dock B (2BEG) was also a targeted dock on the fourth chain (chain D) of the aggregate. This is also near the last chain in this structure (Luhrs *et al*., 2005). Blind docking was not performed as it was extensively studied for 2MXU and 2BEG by (Carlisle, 2018). Therefore, targeted docking was performed near (2BEG chain D and 2MXU chain H) the final chain and at the final chain of the 2NAO (chain C) aggregate, because were interested in disruption of these chains in the aggregate. All three dockings were performed with a grid box of 22 Å. Dock A (2MXU) was centred with coordinates x = 7.417, y = 0.177, z = 0.112; Dock B (2BEG) with x = 13.859, y = 0.0965, z = -0.463, while Dock C (2NAO) was coordinated with x = 10.780, y = 17.975, z = -35.945. The grid box was centred visually to cover the $A\beta_{42}$ fibril structures and to accommodate ligands to move freely.

We also performed Dock D (new-2NAO), new-2NAO consist of a single chain of 2NAO repeated four times. The reasons for editing 2NAO, creating a new aggregate new-2NAO are explained in detail in a later chapter in this thesis. A targeted docking approach was followed also on this structure docking at the "C chain" which will be the last chain in Dock C (2NAO). The coordinates were centred with x = 12.057, y = 18.041, z = -35.901.

All four dockings were performed across 4 CPU cores applying an exhaustiveness of 128 (see scripts in appendix 1-4).

2.5.4 RDKit descriptor calculations

We utilized KNIME Analytical Platform version 3.5.1 (Berthold *et al*.,2009), to create a workflow for determining the drug-likeness of the SANCDB compounds and Wgx-50. All these ligands were in pdbqt file format after molecular docking, and required conversion and collation into SDF files. The first node in the workflow reads these SDF files and creates several columns with each molecule in a new row. The second node was the RDKit Fingerprint, which generates hashed bitbased fingerprints for an input RDKit Mol column and appends them to a table. The fingerprint calculation is not necessary for immediate purposes; however, in terms of other aspects of machine learning which are important in the continuation of this project, the fingerprints prove useful. Finally, the last node was the RDKit Descriptor Calculation. It calculates the descriptors (number of HBDs and HBAs, molecular weight and logP) for each molecule in the input table.

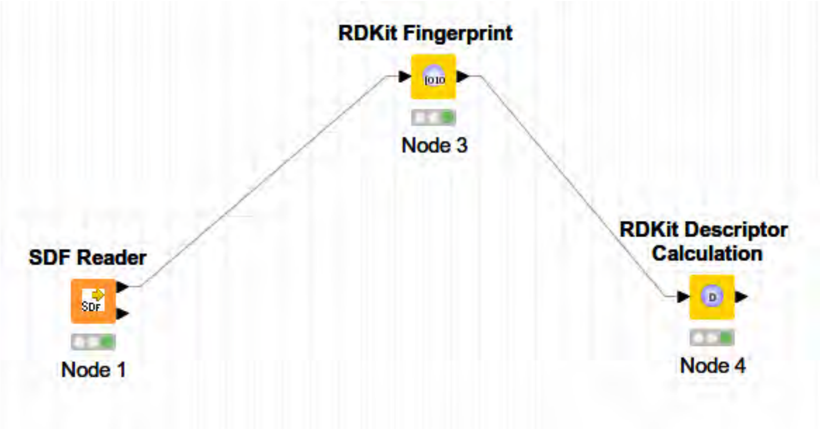

Figure 8: KNIME workflow to determine drug-likeness of the best binding SANCDB ligands and wgx-50.

2.5.5 Wgx-50

Wgx-50 was docked to the four Aβ_{42} aggregate targets following the same approach as the natural products from SANCDB.

2.5.6 Parallel coordinates plot

The SANCDB compounds were fed into the Knime workflow mentioned above with the same parameters as the best binders, then the output table was read in using Excel reader(xls) node. A color manager node was then used to assign colours across the dataset. A parallel coordinates plot

(JavaScript) was finally used to display the multidimensional data set as polylines over five parallel and evenly spaced axes.

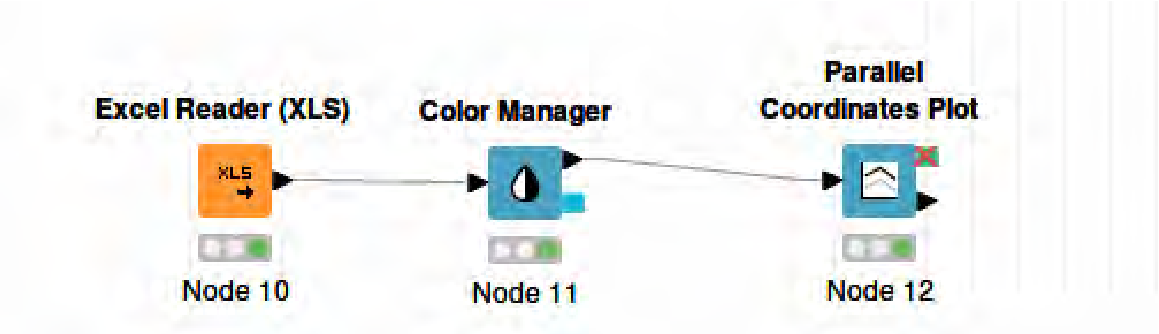

Figure 8.1: KNIME workflow to plot all SANCDB compounds as an overview in terms of Lipinski's rule of five.

2.5.7 Analysis

The top five of the best hits for each docking together with the wgx-50 docking were identified and molecular graphics were created of them together with the receptors using the Discovery Studio visualizer (DSV) version 4.5 program. The ligand interactions were also determined using DSV, while the molecular properties were investigated utilizing the KNIME workflow.

2.6 Results and Discussions

We first performed a structural analysis, to account in detail for using three Aβ$_{42}$ aggregate structures. Figure 9 illustrate the relatively simple residue difference in the docking targets used in this thesis. The sequences of these Aβ aggregates were analyzed using MUSCLE.

```
2NAO:A|PDBID|CHAIN|SEQUENCE/1-42   1 DAEFRHDSGYEVHHQKLVFFAEDVGSNKGAIIGLMVGGVVIA   42
2MXU:A|PDBID|CHAIN|SEQUENCE/1-32   1 ----------EVHHQKLVFFAEDVGSNKGAIIGLMVGGVVIA   32
2BEG:A|PDBID|CHAIN|SEQUENCE/1-26   1 ----------------LVFFAEDVGSNKGAIIGLMVGGVVIA   26
```

Figure 9: Multiple sequence alignment of Aβ_{42} aggregates used, results visualized in Jalview (java version 1.8.0).

The structural analysis results figure 9, 2NAO has no missing residues. While 2MXU and 2BEG are missing 1-10 and 1-16 residues respectively. Residue 1-14 of the 2NAO are partially ordered and in a β-strand conformation, although they do not display unambiguous distance restraints to the remainder of the core structure (Walti *et al*., 2016). It is proposed that the core region of Aβ_{42} comprising residues 17-42 is principally responsible for its stability (Masman *et al,* 2009). It is interesting to note the differences in 3D conformation for each of the three structures given the sequence similarity.

The identification of lead compounds showing pharmacological activity against a biological target and the optimization of the pharmacological properties and potency of these compounds are the important aspects of early-stage drug discovery (Lionta *et al*., 2014). In the human brain, Aβ fibrils are considered the hallmark of AD and are found in the hippocampus and neocortical region (Ramesh *et al*., 2011). Aβ_{42} monomers have a propensity to aggregate into oligomers, protofibrils, and fibrils, with the assistance of exogenous species such as proteins and metal ions, they form dense senile plaques. The formation of dense senile plaques prevents the interaction of neurons in the brain, leading to neuronal atrophy and death (Mash *et al*., 2015). The destabilization of Aβ_{42} and the inhibition of aggregates formation has been argued extensively to combat AD. In this study we worked with three structures of the aggregate; there are only four ssNMR structures of these aggregates available in the PDB (rscb.org). 2MXU, 2BEG and 2NAO were elected for molecular docking study. The fourth structure with PDB ID 5KK3 was omitted due to time constraints, but given the increased number of chains compared to 2NAO (5KK3 has more chains, 18 chains in total) and given it also contains the full sequence as does 2NAO, it is an attractive structure to address in future studies. The dockings were targeted near the last chains for 2MXU (chain H), 2BEG (chain D) new-2NAO (chain C), and on the last chain for 2NAO (chain C). This was thought that it could assist in discovering if the SANCDB natural products could aid destabilizing these chains and prevent aggregation by another monomer to the fibril.

AutoDock Vina (Trott and Olson, 2010) was utilized to perform dockings, after docking top five SANCBD hits for each of the four, docking simulation were identified. DSV was used to identify the protein-ligand interaction for these hits to the Aβ_{42} aggregate structures.

Figure 10 and 10.1 shows an overlay of the docking results that were obtained. Seven hundred and twenty-eight natural products were docked against 2MXU, 2BEG, 2NAO and new-2NAO.

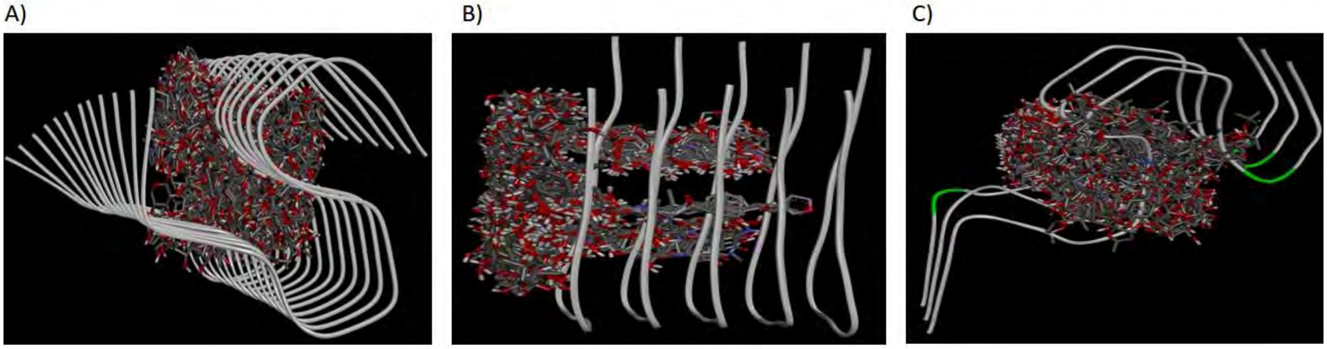

Figure 10: The images of the docking simulations performed using AutoDock Vina visualized in DSV. A) Dock A (2MXU); B) Dock B (2BEG); C) Dock C (2NAO).

Figure 10.1: The screenshots of A) Dock D, also obtained using AutDock Vina

In Table 1, the docking scores are estimated using a scoring function in AutoDock Vina. The docking scores ranged from –10 to –6.5. SANC00585 (D), SANC00407 (D) and SANC00414 (D) have the lowest binding energies. Dock D (new-2NAO) showed the lowest group of docking scores and Dock B (2BEG) showed the highest compared to all four dockings.

Table 1: Docking scores between the receptors A (2MXU), B (2BEG), C (2NAO), D (new-2NAO) and the top hits from all the SANCDB dockings.

SANCDB compound	**Docking score**	**Dock**
SANC00490	-8.9	A
SANC00261	-8.4	A
SANC00585	-8.3	A
SANC00264	-8.2	A
SANC00265	-8.1	A
SANC00248	-7.3	B
SANC00247	-6.9	B
SANC00415	-6.8	B
SANC00348	-6.5	B
SANC00423	-6.4	B
SANC00489	-9.3	C
SANC00491	-8.5	C
SANC00422	-8.1	C
SANC00449	-7.9	C
SANC00488	-7.5	C
SANC00585	-10	D

SANC00490	-9.1	D
SANC00414	-9.2	D
SANC00264	-9.1	D
SANC00407	-9.2	D

Figure 11 shows the docked top five hits from SANCDB against 2BEG. In the images shown 2 compounds dock on the surface of 2BEG. These are compounds SANC00415 and SANC00348 (C and D). The rest of the top five compounds are docking in the interior of the U-shaped 2BEG. The binding energies do not significantly discriminate based on the binding position of the top 5 compounds in Dock B (2BEG). By comparison the docking of wgx-50 to 2BEG is shown later in the chapter, in Figure 19.

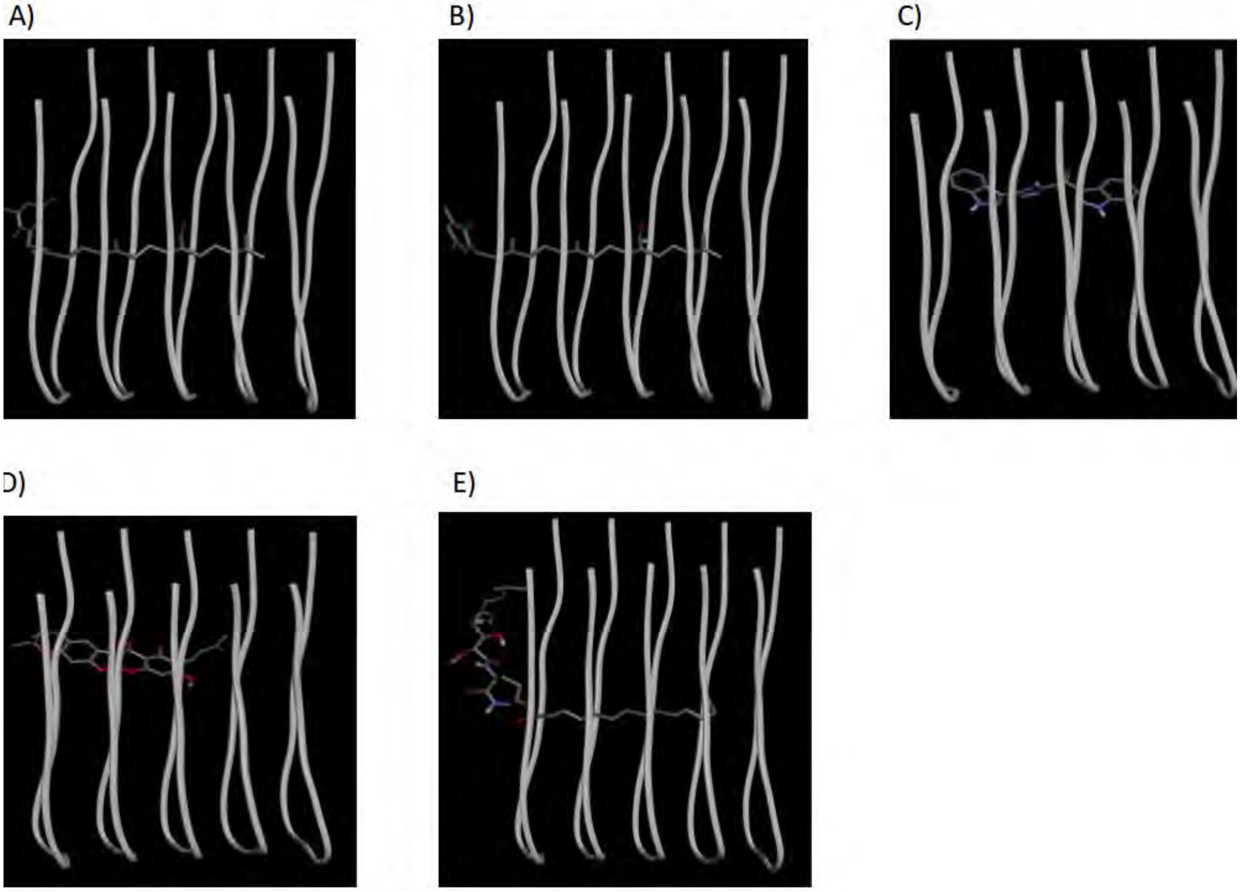

Figure 11: The Dock B (2BEG) and top five SANCDB compounds, images were created in DSV. A) SANC00248, B) SANC00247, C) SANC00415, D) SANC00348, and E) SANC00423.

Table 2 shows all the interactions from Dock B (2BEG) for the top 5 hits. There were no van der Waals clashes present in these hits. The majority of the interactions observed were hydrophobic Alkyl interactions. There were three conventional hydrogen bonds formed between SANC00247, SANC00415, SANC00423 and 2BEG. For each of these three cases, the hydrogen bonds were formed on different residues and chains.

Table 2: The interactions between the receptor and the top hits from Dock B (2BEG), the interactions were visualized in DSV. The letters within brackets indicate the exact chain were the interaction is observed.

SANCDB compound	**Alkyl interactions**	**Amide-π stacked**	**Conventional hydrogen bonds**	**Carbon hydrogen bond**	**π-Sulfur**
SANC00248	Ala21(E, D, B, A) Leu34(B, E, D) Val36(C, B, D, E)				
SANC00247	Ala21(A, B, D, E) Val36(B, C, D, E) Leu34(B, D, E)		Glu22(E)		
SANC00415	Met35(B, C, D, E)	Val36(B, C, D)	Met35(B)		
SANC00348	Val39(B, E) Met35(C)	Val36(C)		Gly37(C)	Met35(E)
SANC00423	Leu17(E) Phe19(D, E) Val36(E, B, C) Ala21(A, B, E) Leu34(B)		Gly37(E)	Met35 (E)	

A pictorial representation of Table 2 is used in Figure 12. The image was obtained using DSV tools for receptor-ligand interactions. Amide-π stacking interactions are between an amide group and an aromatic ring, these interactions are related to canonical aromatic π-stacking, the π-surface of the amide bond stacks against the π-surface of the aromatic ring (Harder *et al*., 2013). In π-Sulphur interactions a π-electron cloud of an aromatic ring interacts with a lone pair of electron cloud of Sulphur atom (Harder *et al*., 2013). Alkyl interactions are non-covalent interactions, between the electrons of the electrons of the compounds and the receptors (Ribas *et al*., 2002). Conventional hydrogen bonding produces a wide variation in the interaction energy, depending on the molecular systems involved. A typical example of this type of non-covalent interaction is the interaction observed in the benzene···NH_3 complex (Kumar *et al*., 2012). The carbon hydrogen bond is an interaction between carbon and hydrogen atoms (Horowitz, 2012).

Figure 12: The image of Dock B (2BEG), obtained from DSV, representing the interactions between SANC00348 and 2BEG.

The Dock B (2BEG) results are of particular interest in this thesis, being used further in chapter 3, to investigate the pulling and umbrella simulation in the presence of the SANCDB top hits. We elected Dock B results, since in literature Lemkul and Bevan, 2009 have also studied 2BEG. In their work they studied several factors that influence the stability of 2BEG following *in silico* mutation. They employed molecular dynamic, center-of-mass (COM) pulling and umbrella sampling to investigate the chain dissociation of Aβ.

The docking results of the top five hits against 2MXU are shown in Figure 13. SANC00490 has the lowest binding energy in this set, docking in between chain I and H (Figure 13 A), while the other docked natural products occupy a similar region (Figure 13 B-E)

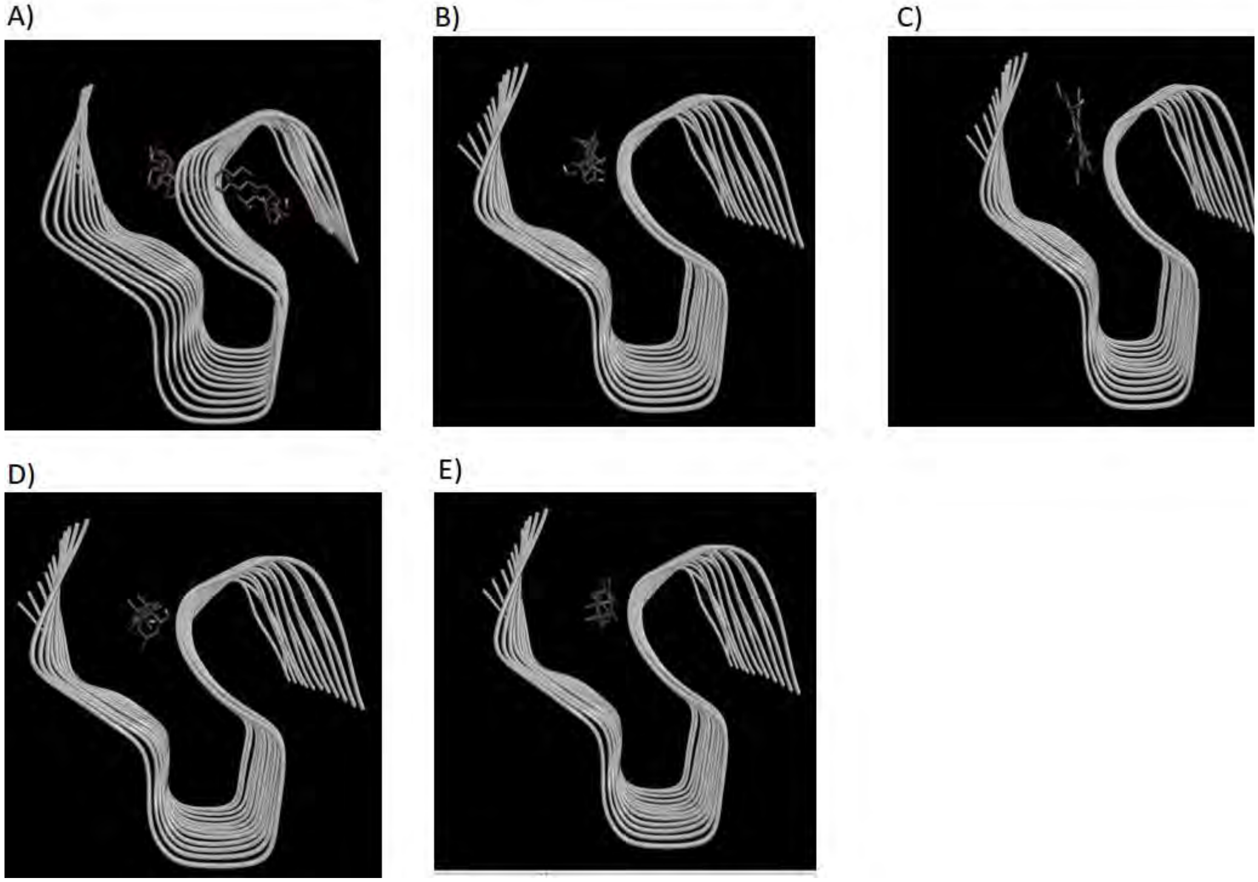

Figure 13: The docking results of the top 5 binding natural products from the South African database against 2MXU aggregate. A) SANC00490, B) SANC00261, C) SANC00585, D) SANC00265 and E) SANC00264.

The summary of the residue interactions of the best 5 binding compounds with receptor 2MXU is presented in Table 3. The ligand with the lowest binding energy in this case is SANC00490. A π-π T-shaped interaction was observed SANC00585. This is an interaction of a π-electron cloud, it occurs between two aromatic groups that are T-shaped (Ribas *et al.*, 2002). SANC00264 and SANC265 showed identical interactions. Across the 5 compounds there was also one common interaction, an alkyl interaction with residue Leu17 in chain F. π-sigma interactions are shown to depend on the bond length and the type of hybridization, this includes the angle between sigma bonds, and on the nature of the bonding atoms (Gleiter, 1987).

Table 3: The interactions between the receptor and the top hits from Dock A (2MXU), the interactions were visualized in DSV. The letters within the brackets indicate chain were the interaction is observed.

SANCDB compound	**Alkyl interactions**	**Conventional hydrogen bond**	***π-π* T-shaped**	***π*-Sigma**
SANC00490	Leu17(F) Leu34(F) Ile32(F, G)	His13(F)		Ile32(F)
SANC00261	His14(F) Leu17(F, G, H) Ile32(F, G, H)			
SANC00585	Leu17(F) Phe20(F) Ala30(F) Ile32(F)		Phe19(F)	
SANC00265	His14(F) Leu17(F, H) Leu34(F) Ile32(H)			
SANC00264	His14(F) Leu17(F, G) Leu34(F) Ile32(H)			

Figure 14 shows the SANC00490 interactions from Table 3. In this figure the interactions between the respective leucine and isoleucine residues and the ligand are clearly observed.

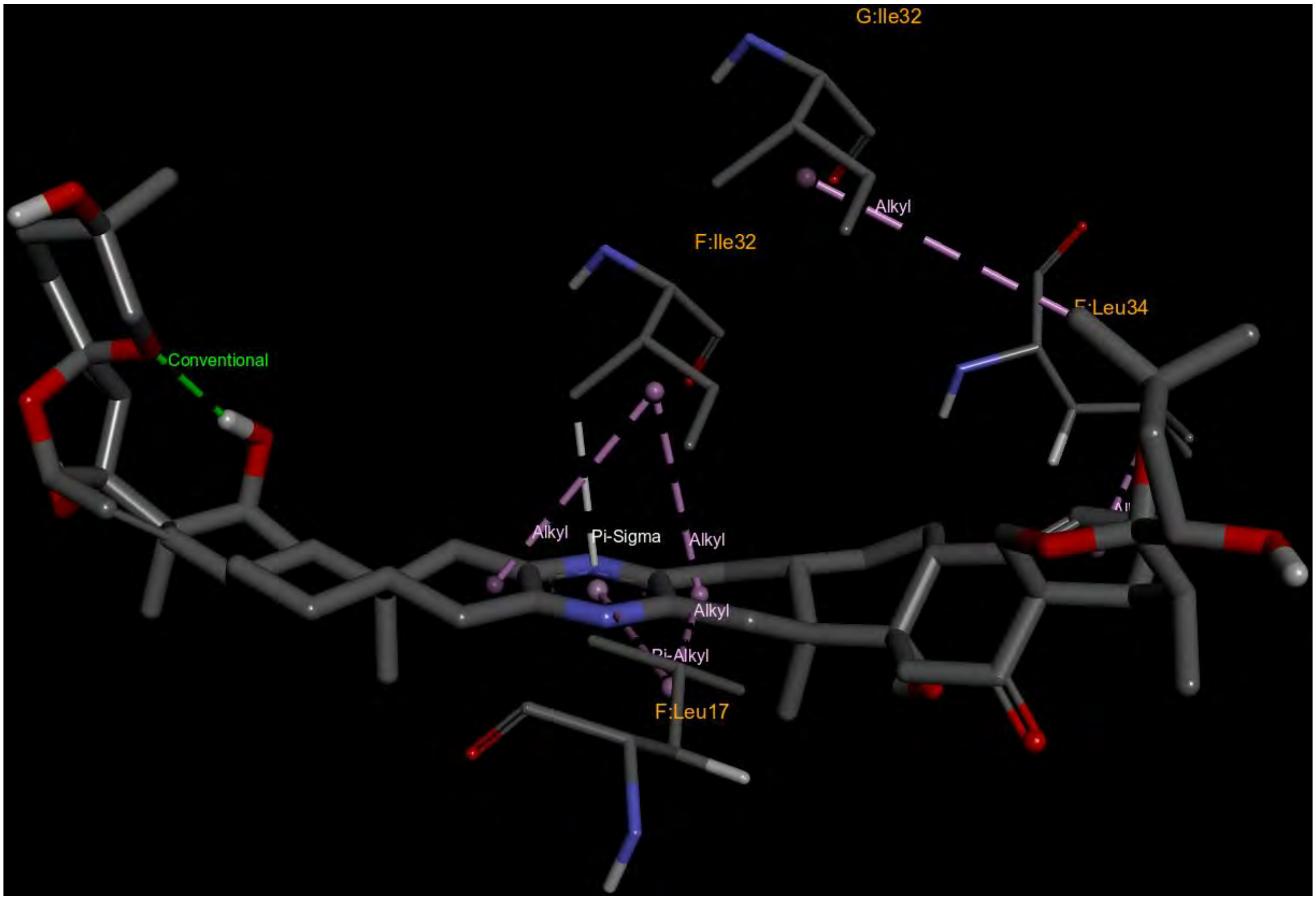

Figure 14: An image showing the interaction of residues with SANC00490 against 2MXU (Dock A). The image was generated using DSV.

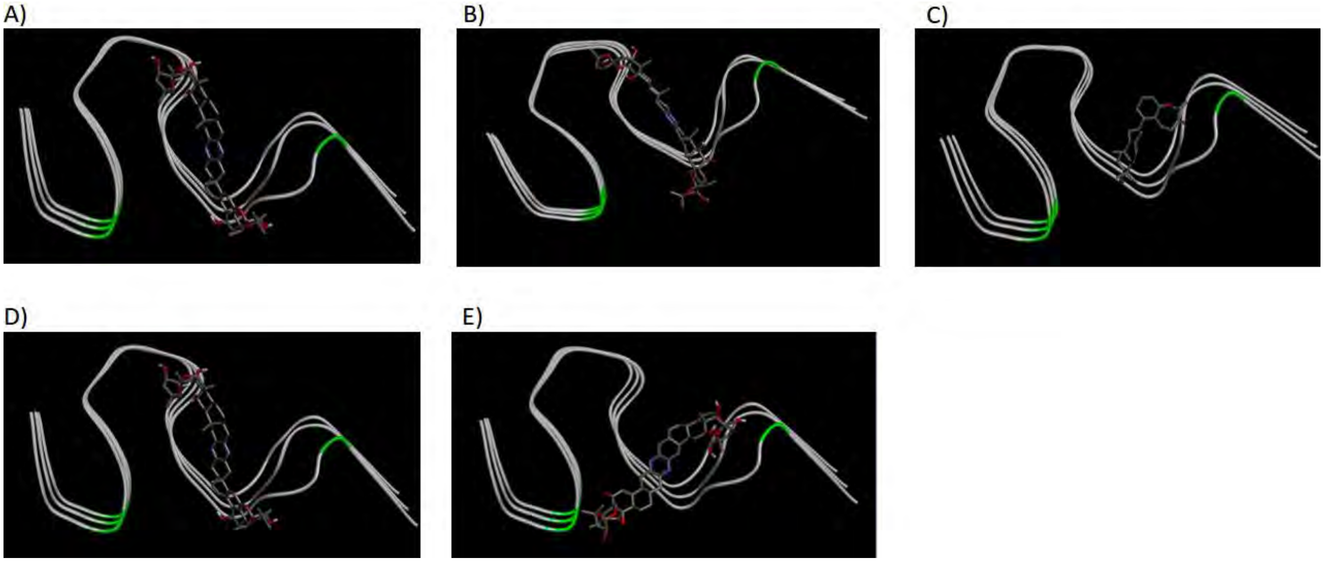

Figure 15: The five lowest energy dockings for Dock C (2NAO), A) SANC00489, B) SANC00491, C) SANC00422, D) SANC00449 and E) SANC00488

In terms of docking to 2NAO in dock C, unfavorable donor-donor and acceptor-acceptor interactions were observed for SANC00489, SANC00422 and SANC00448 (Table 4). These interactions are not satisfactory for a good inhibitor, although at this stage not enough information is available to rule them out as poor inhibitors. More detailed investigation of these compounds will provide firmer conclusions with respect to these ligands.

Table 4: Table showing the docked ligands with lowest energy and their interactions with the receptor from Dock C (2NAO), interactions investigated in DSV. Residue chains are shown in brackets.

SANCDB compound	**Alkyl interactions**	**Conventional hydrogen bond**	**Carbon hydrogen bond**	**Unfavorable Acceptor-Acceptor**	**Unfavorable Donor-donor**	**π-Sigma**
SANC00489	Val12(C) Val18(C) Phe20(C) Phe24(C)	His13(C)	His13(C) Gln15(C)	Gln15(C)		
SANC00491	Val12(C) Val18(C) Phe20(C) Val24(C)					
SANC00422	Tyr10(B) Val12(C) Lys16(C) Val18(C)	Gln15(C)			Leu17(C)	
SANC00449	Val12(C) Lys16(C) Val18(C)		His13(C)			Val12(C)
SANC00488	Val12(C) Leu17(C) Val18(C)	Gly9(B) Glu11(B, C)			Glu15(C)	

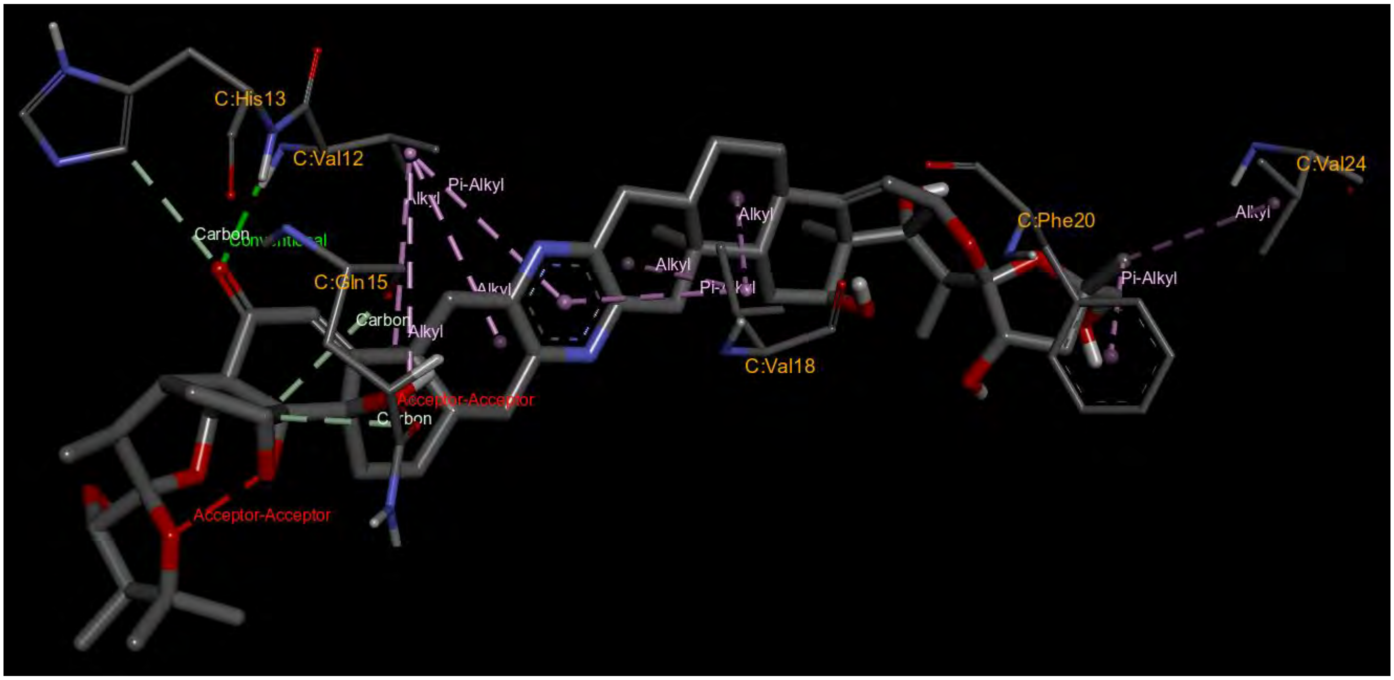

Figure 16: The image of Dock C (2NAO), obtained from DSV, representing the interactions between SANC00489 and 2NAO.

Figure 16 shows the interactions between SANC00489 and 2NAO, in this particular case hydrophobic interactions are abundant valine residues in the C chain of the model and ligand.

A final model receptor, (named the new-2NAO aggregate), was obtained by editing 2NAO. Details of this edit will be provided in a later chapter. Docking to this model was interesting in that complexes obtained exhibited the lowest binding energy compared to the other aggregates used in this thesis. In Figure 17 the top 5 lowest binding poses for this set of docking experiments are represented.

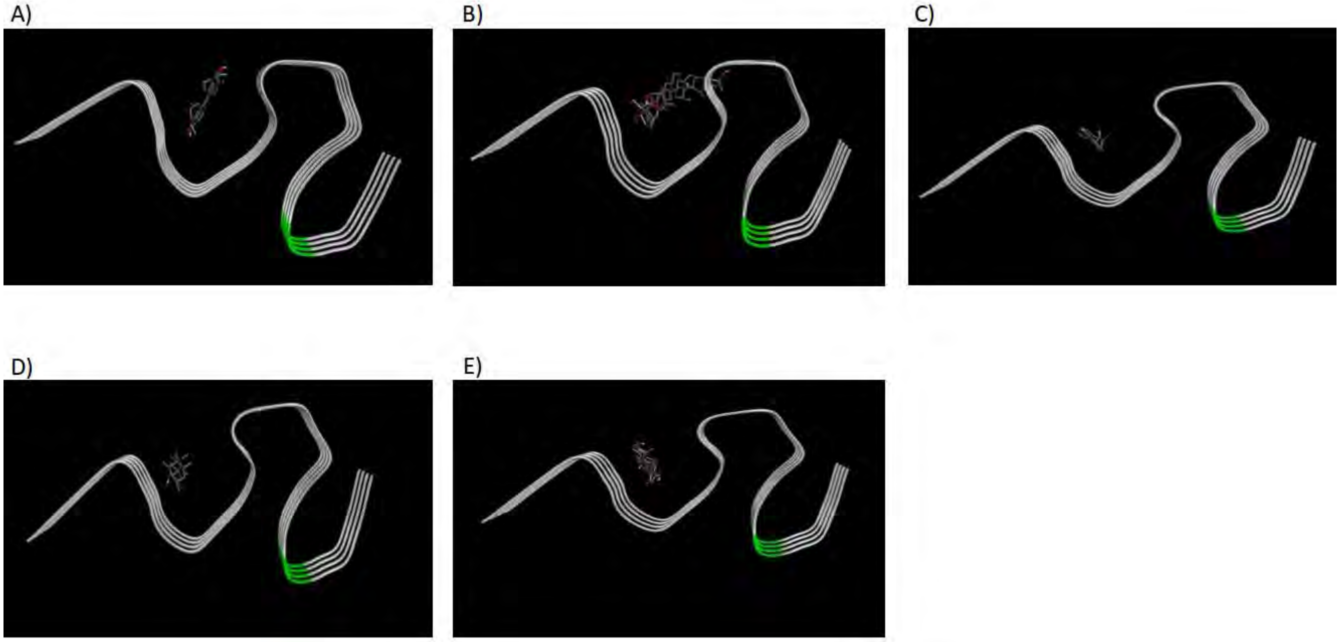

Figure 17: The images show, docking for the top five binding energies for Dock D (new-2NAO). Images were obtained from DSV, A) SANC00585, B) SANC00490, B), SANC00414, D) SANC00261 and E) SANC00407.

As before the, the details of the ligand residue interaction are detailed (Table 5). It is interesting to note though, that residue Tyr10 of chain D, has an unfavourable acceptor-acceptor interaction with SANC00407. This interaction is not shown on the table (see appendix 5, Figure 1 for details). Figure 18 shows the rich range of hydrophobic interactions in the dock between new-2NAO and SANC00585.

Table 5: The interactions between the receptor and the top hits from Dock D (new-2NAO), the interactions were visualized in DSV. The letters within brackets indicate the chain where the interaction is observed.

SANCDB compound	Alkyl interactions	Conventional hydrogen bond	Carbon hydrogen bond	π-cation	π-Donor	π-Sigma	π-anion
SANC00585	Val17(B) Phe20(B)					Phe19(B)	

	Ile32(B) Leu34(B)						
SANC00490	Ala21(B)	Lys16(B) Glu11(C) Lys16(C)					
SANC00414		Tyr10(C, D) Glu11(C) Lys16(C)	Glu11(C)	Glu11(D)	Tyr10(C)	Glu11(D)	
SANC00264	His13(B)		Glu11(D)				Glu11(D)
SANC00407	His13(B)	Tyr10(C) His13(C) Lys16(D) Glu11(D)	Glu11(B) His13(D)				

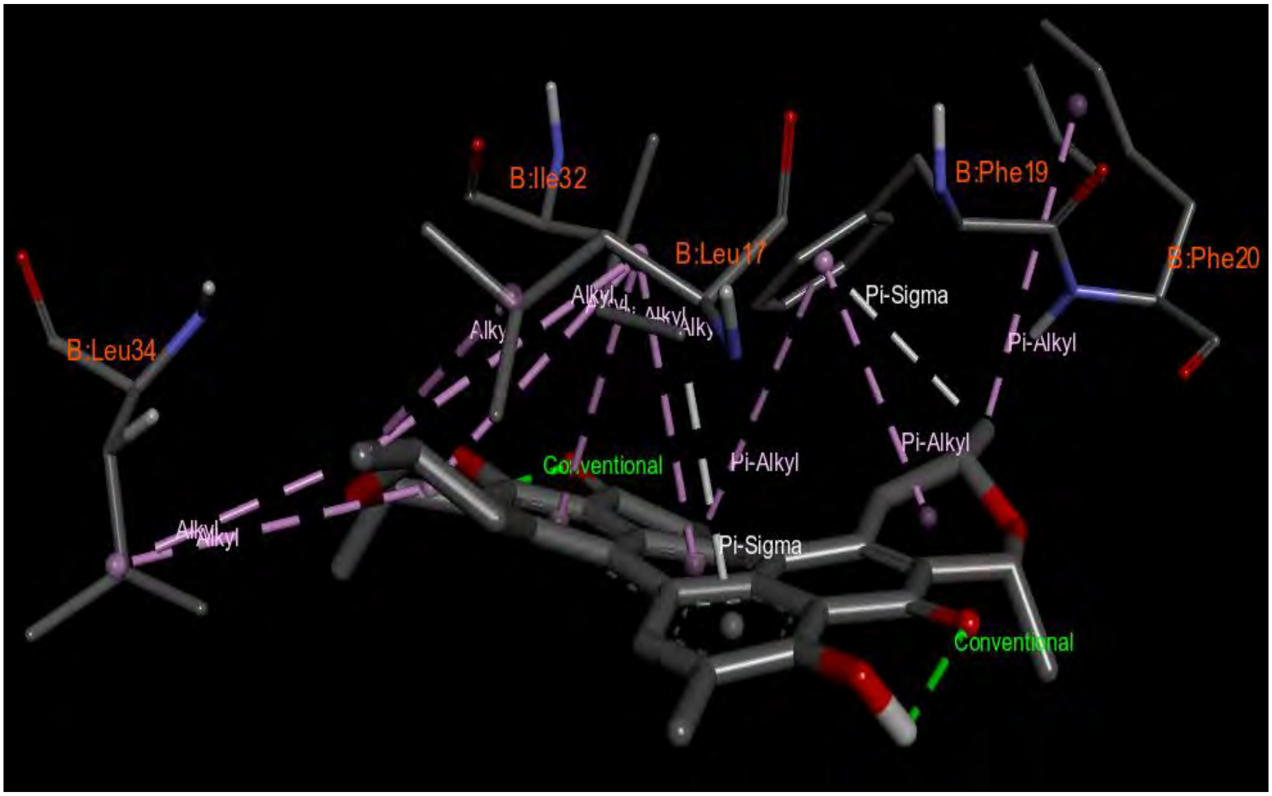

Figure 18: The interaction between SANC00585 and new-2NAO, Dock D.

All docking simulations performed in this thesis were targeted to the more variable chains of the aggregates (near or at the end of the Aβ_{42} fibril). The understanding was that not only would targeting of these chains could prevent further Aβ_{42} monomers from binding to the fibril structure, but this would be the best strategy to explore destabilizing of terminal monomers. Dock C and D were both targeted on the last chains, However Dock D (new-2NAO) was the group with the lowest binding energies. The cause of this is evident from the interactions, Table 5 has more conventional hydrogen bond interactions as compared to other interaction summary tables (Table 2, 3, and 4).

Dock B (2BEG) contained the highest set of docking scores. From Table 2, it is not immediately clear why this is. The table is mostly dominated by alkyl interactions with a few conventional and carbon hydrogen interactions. However, Dock A (2MXU) has almost no hydrogen bond interactions and is dominated by alky interactions (Table 3) but the group shows better binding energy than Dock B (2BEG).

Wgx-50 (the known drug candidate targeting Aβ for AD) was also docked to the four structures. The docking approach used was the same for each specific structure. i.e. wgx-50 against 2BEG followed the Dock B (2BEG) approach. Table 6 illustrates the binding energies of wgx-50. While Figure 19 shows the docking region of wgx-50.

Table 6: Dock score of wgx-50 against Aβ_{42} fibril structures.

Wgx-50	**2MXU**	**2BEG**	**2NAO**	**New-2NAO**
Docking score	-5.4	-6.6	-5.8	-6.6

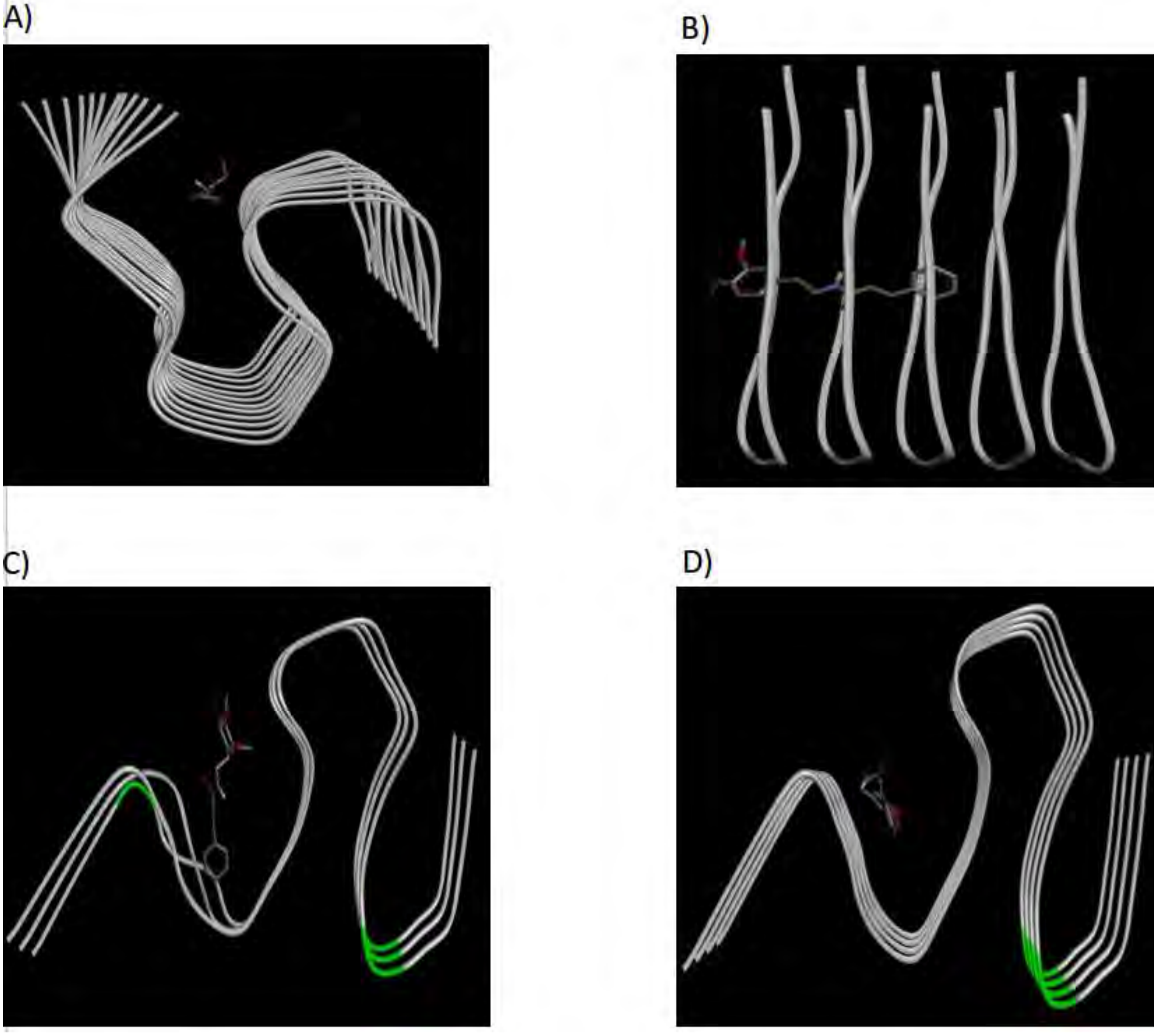

Figure 19: Wgx-50 docked to the four aggregates, A) 2MXU, B) 2BEG, C) 2NAO and D) new-2NAO.

As is presented in Table 6, 2BEG and new-2NAO have the same binding score of 6.6 for wgx-50. More so, the wgx-50 dock score is within the same range of binding energy as the top 5 SANCDB compounds in Dock B (2BEG). These results may offer insight in terms of the interactions, and thermodynamic destabilization of the aggregates. Table 7 illustrates the exact interactions of wgx-50 the $A\beta_{42}$ with aggregates.

In Table 7, a point to note is that the unfavorable donor-donor interaction between residue Lys16 of chain A and wgx-50 in 2NAO aggregate structure is present but not shown (see appendix 5, Figure 2 for details).

Table 7: Interactions between wgx-50 and the aggregates used in this study.

Aβ42 aggregates	**Alkyl interactions**	**Conventional hydrogen bond**	**Carbon hydrogen bond**	**π-cation**	**π-π stacked**	**π-Sigma**
2MXU	Leu17(B) Ile32(B)		Gly33(B)			
2BEG	Leu34(E, D, C) Val36(C, D) Ala21(B, C, E)					
2NAO	Lys16(A, B) Ala21(C)		Phe20(B)		His13(A)	Val12(B) Ala21(B)
New-2NAO		His13(C)	His13(D)	Lys16(B)		

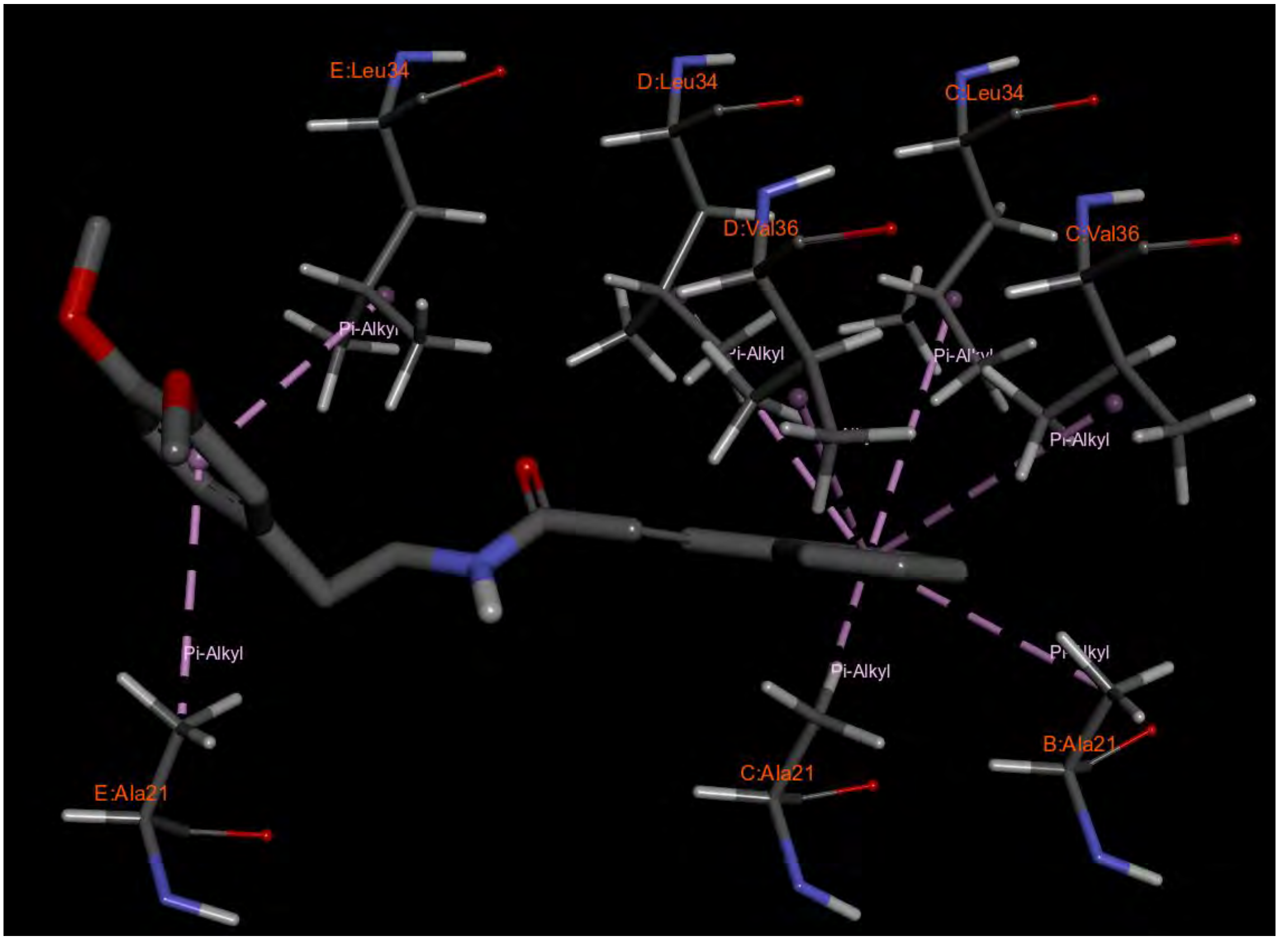

Figure 20: The interactions of wgx-50 in the receptor 2BEG

Wgx-50 docked against 2BEG only showed π-alky interactions with all the residues it interacts with (Figure 20). These interactions are consistent with the Dock B (2BEG) interactions with SANC00248 and SANC00247. However, SANC00247 deviates by having one conventional hydrogen bond. As such SANC00248 and SANC00247 are promising in terms of potential for Aβ disruption.

Lipinski's rule of five is a heuristic approach for predicating drug-likeness. The rule states that molecules having less than 500 amu molecular weight, logP of less than 5, less than 5 hydrogen bond donors and less than 10 hydrogen bond acceptors good oral permeation (Lipinski *et al.*, 1997). Figure 21 shows a parallel coordinates plot of relevant physicochemical properties of compounds in the SANCDB. It is an overview of the seven hundred and twenty-eight SANCDB compounds used in this thesis in relation to Lipinski's rule of 5. High oral bioavailability is an important consideration for the development of bioactive molecules as therapeutic agents (Salah *et al*., 2015). All compounds that meet the Lipinski's rule of five and the Veber rules, suggest that they are theoretically ideal for oral uptake (Zerroug *et al*., 2018).

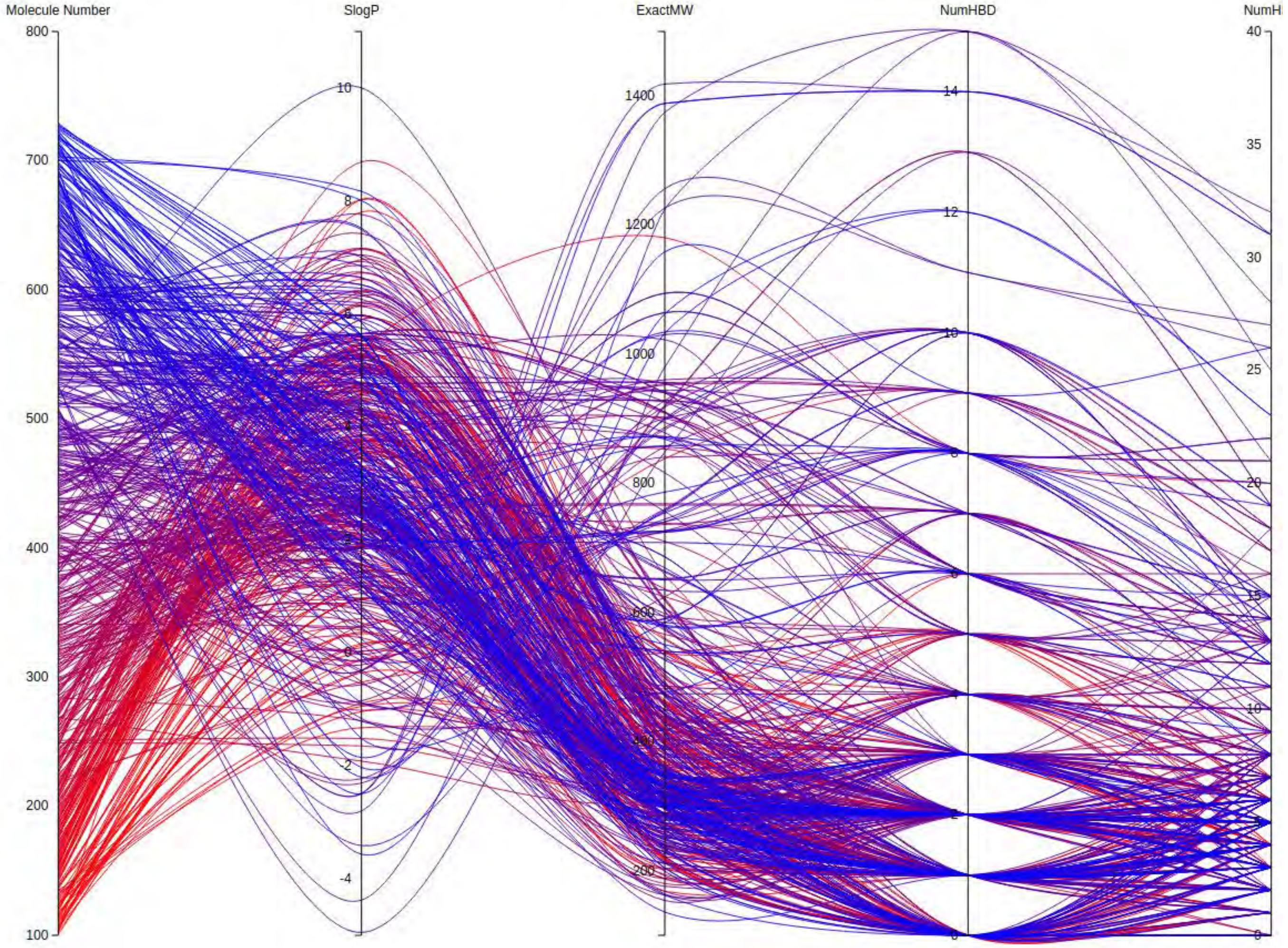

Figure 21: Parallel coordinate plot of all the SANCDB compounds studied.

Table 8 shows the determined Lipinski's rule of five parameters and Veber's rule on the topological polar surface area (TPSA). TPSA is defined as the surface sum over all polar atoms, particularly oxygen and nitrogen. An increase in TPSA is associated with an increase in the percentages of compound that are not permeable (Palma *et al*., 1997). Verber *et al*., 2002 argues that TPSA should be less than 140 Å^2.

Table 8: Predicted Lipinski's rule of five parameters for the top five selected Dock A (2MXU), Dock B (2BEG), Dock C (2NAO), Dock D (new-2NAO) and wgx-50 drug candidate.

Compound ID	**Molecular weight (g/mol)**	**Hydrogen Acceptors**	**Hydrogen Donors**	**LogP**	**TPSA**	**No. Of rules violated**
Rule	<500	<10	<5	≤5	<140	≤1
Wgx-50	311.38	4	1	3.08	47.56	0
SANC00247	424.58	4	1	6.61	71.44	1
SANC00248	408.58	3	0	6.73	51.21	1
SANC00261	442.73	2	2	7.14	40.46	1
SANC00264	420.59	3	1	6.42	54.37	0
SANC00265	436.59	4	2	5.39	74.6	1
SANC00348	594.77	7	3	3.97	105.45	1
SANC00407	328.38	9	5	2.59	138.07	0
SANC00414	326.36	5	3	3.56	73.04	0
SANC00415	456.71	5	3	4.27	77.33	0
SANC00422	584.80	3	1	7.04	46.53	2
SANC00423	895.15	10	5	3.30	154.42	2
SANC00449	895.15	12	6	5.35	184.08	5
SANC00488	941.17	14	6	3.75	213.68	4
SANC00489	955.20	14	6	4.00	213.68	4
SANC00490	911.19	12	5	5.65	180.92	4
SANC00491	911.19	12	5	5.65	180.92	4
SANC00585	510.57	6	2	5.97	93.06	2

From Table 8, it is observed that nine out of the sixteen best docking SANCDB compounds across all dockings obey the Lipinski's rule of five and Verber's rule on TPSA. The drug candidate wgx-50 also abides by these rules. The compounds that obey these rules are SANC00247, SANC00248, SANC00261, SANC00264, SANC00265, SANC00348, SANC00407 and SANC00414.

Although more than half of our compounds obeyed the rules mentioned above, one has to be cognizant of the drawbacks of these rules. Since these rules are based on a distribution of calculated properties, some drugs will lie outside the parameter cutoffs. Equally, there will be leads that meet these rules that will never be effective medicines. For example, Doak *et al*., 2014 identified 226 pre-clinical candidate drugs which have a molecular weight greater than 500 g/mol. This set includes peptides, HIV protease inhibitors, azole antifungal, cyclosporins, cardiac glycosides etc.

Table 9 provides an abbreviated background to the compounds from SANCDB best performing docking against Aβ_{42}, including the compound name, organism, and one or two known tested activities.

Table 9: Summary of the best-performing SANCDB compounds, by categorizing them based on their names to the compound's known activities.

Compound ID	**Name**	**Source organism**	**Compound uses**
SANC00247	Sargaquinoic acid	***Sargassum heterophyllum***	Antimalarial
SANC00248	Sargaquinal	***Sargassum heterophyllum***	Antimalarial
SANC00261	11α-Hydroxy-β-amyrin	***Elaeodendron croceum***	No record
SANC00264	Tingenone	***Elaeodendron croceum***	Anticancer activity activities against Vero cells
SANC00265	Tingenine B	***Elaeodendron croceum***	Anti-HIV activity
SANC00348	Kraussianone 5	***Eriosema kraussianum***	Contraction of corpus cavernosum tissue
SANC00407	(25R)-3β-Hydroxy-5α-spirostan-1β-yl β-D-glucopyranoside	***Ornithogalum thyrsoides***	Cytotoxic activity on HL-60 leukemia cells Cytotoxic activity on HSC-2 cells
SANC00414	Spongotine A	***Topsentia pachastrelloides***	Antibacterial
SANC00415	Bromodeoxytopsentin	***Topsentia pachastrelloides***	Antibacterial
SANC00422	Sodwanone Q	***Axinella weltneri***	diuretic activity
SANC00423	Bengamide A	***Jaspis digonoxea***	Anticancer activity Antimitotic activity

SANC00449	Cephalostatin 6	***Cephalodiscus gilchristi***	Anticancer activity
SANC00488	Cephalostatin 14	***Cephalodiscus gilchristi***	Anticancer activity
SANC00489	Cephalostatin 15	***Cephalodiscus gilchristi***	Anticancer activity
SANC00490	Cephalostatin 16	***Cephalodiscus gilchristi***	Anticancer activity
SANC00491	Cephalostatin 17	***Cephalodiscus gilchristi***	Anticancer activity
SANC00585	Scutiaquinone A	***Scutia myrtina***	Anthelmintic Activity

The structures of these compounds in Table 9 are readily available on the SANCDB database (sancdb.rubi.ru.ac.za).

Since the SANCDB compounds docked against 2BEG showed dock scores within the range of wgx-50 docked across all aggregates (Table 1 and 6), and also since SANC00247 and SANC00248 interactions were similar to wgx-50 docked against 2BEG (Tabled 7 and 2), dock B (2BEG) best-performing ligands are used to study the thermodynamics of destabilizing aggregates in the following chapter. It is also useful to reiterate that 2BEG has been used in previous literature (Lemkul and Bevan, 2010), and this also makes an attractive target for evaluating the disruption ability of these ligands.

Chapter 3: Evaluating the stability of β-amyloid fibrils using molecular dynamics

3.1 Introduction

Molecular dynamics (MD) simulations have been successfully used to study interactions among proteins, lipids, and small molecules to provide atomic-level detail of many phenomena (Lemkul and Bevan, 2010). In a classical MD simulation, the motion of atoms and molecules is described by classical physics. MD simulation was first applied in theoretical physics in the late 1950s (Alder and Wainwright, 1959). It is widely used today in many science and technology domains including computational biophysics and medicine (Hospital *et al*., 2015). There are different force fields that have been worked out to model both biomolecules and ligands at an accurate level such as GROMOS (Haung *et al*., 2010), AMBER (Hornak *et al*., 2006), CHARMM (Vanommeslaeghe *et al*., 2010) and OPSL (Kaminski *et al*., 2010). Even though the force fields are different, the interaction energies have common functional form (Eq.3),

$$E = E_{bonded} + E_{non-bonded} \qquad \text{Eq.3}$$

where E_{bonded} is the interaction energy of atoms which are connected by covalent bonds, and $E_{non-bonded}$ is a term containing the non-bonding interactions such as Van der Waal's (Eq.8) and electrostatic interactions (Eq.7) (Allen, 2004).

3.2 Bonding potential energy

The E_{bonded} consists of four terms to the total energy (E), these are bond stretching (Eq.4), angle bending (Eq.5), and dihedral and improper torsions (Eq.6) (González, 2011).

$$V_b(r_{ij}) = \frac{1}{2}k^b_{ij}(r_{ij} - b_{ij})^2 \quad \text{Eq.4}$$

The bond stretching energy equation is based on Hook's law. The k_{ij} parameter is the bond stretch force constant, r_{ij} is the actual bond length, while b_{ij} defines its equilibrium length (Moses *et al.*, 2017). Both actual bond length and bond stretch force constant are specific for atom pairs. They are either extracted from experimental data or QM calculations. The bond stretching is usually represented with a simple harmonic function, this implies that the bond cannot be broken, thus no chemical processes can be studied. This yields one of the limitations of force field based MD simulations as compared to *ab initio* MD. Although sometimes Morse potential and other functional forms are used to improve the accuracy, they are computationally expensive (González, 2011).

Angle bending is also often represented by a harmonic potential, between a triple of atoms $i - j - k$ is related with the angle θ_{ijk}.

$$V_a(\theta_{ijk}) = \frac{1}{2}k^{\theta}_{ijk}(\theta_{ijk} - \theta^0_{ijk})^2 \quad \text{Eq.5}$$

θ_{ijk} represents the actual bond angle, θ^0_{ijk} represents the equilibrium bond angle, and k_{ijk} denotes the angle bending force constant (Moses *et al.*, 2017). The actual bond angle and equilibrium bond angle are dependent on the chemical type of atoms involved. Angle bending, may sometimes be optimized for fitting to vibrational spectra, by adding the Urey-Bradley potential (Eq.5.1).

$$U_{\mathrm{UB}} = \sum_{\text{angles}} \frac{1}{2}k_{\mathrm{UB}}(s - s_0)^2 \quad \text{Eq.5.1}$$

In the Urey-Bradley term, *s* represents the distance between two external atoms forming the angle (González, 2011).

The dihedral or torsional term is only included in molecules that contain four or more atoms in a row. These terms are as important as angle bending and bond stretching. However, although bond stretching, and angle bending can be replaced by a rigid approximation, torsional terms are vital in obtaining the correct degree of rigidity/flexibility of the molecules allowing for major conformational changes as a result of rotation about bonds (González, 2011).

$$V_d(\phi_{ijkl}) = k_\phi(1 + cos(n\phi - \phi_s)) \qquad \text{Eq.6}$$

The torsional energy is described with terms, k_φ for the dihedral angle force constant, φ_s is the dihedral angle, n =1,2,3 denotes the coefficient symmetry (González, 2011).

3.3 Non-bonding potential energy

Electrostatic interactions play an important role in determining the structure and packing of molecules. The Coulombic energy term is presented in Equation 7,

$$V_c(r_{ij}) = \frac{q_i q_j}{4\pi\epsilon_0 r_{ij}} \qquad \text{Eq.7}$$

where q_i and q_j are the atomic charges, r_{ij} is the distance in Å separating atoms i and j, ε_0 is the dielectric constant. Although there may be, biological systems whereby solvent molecules are not included explicitly in the simulation, most simulations include explicit solvent and so ε_0 usually carries a value of 1(Gao, 1998).

The van der Waals interaction is the long-range attraction which is proportional to R^{-6}. Since at short distances the interaction of all atoms is repulsive. The Lennard-Jones potential (Eq.8) is often used to describe the attractive interactions. The repulsive interaction may be is represented using the exponential function, as is used in the Buckingham potential (González, 2011). However, a power 12 term is often used for the repulsive term within the van der Waal's interaction (Equation 8),

$$V_{LJ}(r_{ij}) = \frac{C_{ij}^{12}}{r_{ij}^{12}} - \frac{C_{ij}^{6}}{r_{ij}^{6}} \quad \text{Eq.8}$$

where C^{12} and C^{6} are specific Lennard-Jones parameters. These parameters are dependent on atom types and force fields. The van der Waals forces between any pair of atoms belonging to different molecules, however, they also occur on atoms of the same molecule (González, 2011).

3.4 Background on umbrella sampling

Umbrella sampling (US) was developed by Torrie and Valleau (Torrie and Valleau, 1974). In US a bias potential, is applied to the system to ensure there is enough sampling along the entire reaction coordinate. The motive of the bias potential is to connect energetically separated regions in phase space, hence the name umbrella sampling (Kästner, 2011). The results obtained from individual simulations must be unbiased and recombined, such that accurate information about the free energy of the system is acquired (Mills and Andricioaei, 2008).

Free energy is an important quantity that describes chemical and biological processes (You *et al.*, 2019). This is because free energy controls to a certain extent, directionality of binding and unbinding kinetics. As such, it is a central task for computational chemists to determine accurate free energy calculations, notably along a chemical or biological process (Miao and McCammon), 2016). US is one of the most used methods to compute the potential mean force (PMF) based on probability calculations along a given coordinate (Torrie and Valleau, 1977).

US is suitable for calculating PMF for non-covalent ligand-receptor association/dissociation interactions. PMF can provide thermodynamic details for molecular recognition (You *et al*., 2019). Limitations of US include the inability to provide the dissociation path by itself. Thus, enhanced sampling methods are employed. Enhanced sampling methods such as, include steered molecular dynamics, adaptive biasing force and metadynamics (You *et al*., 2019).

3.5 Molecular dynamics, umbrella sampling

Since it is challenging to obtain high-resolution structural data of Aβ aggregates, MD simulations are an ideal approach for studying these systems. While US is particularly useful in analyzing macromolecular interactions (Lemkul and Bevan, 2010). In this chapter, a series of configurations are generated along a reaction coordinate, ξ. The Aβ_{42} without a ligand bound is used as a reference. The bound structure contains each of the five different best binding ligands including wgx-50 from chapter 2, Dock B (2BEG). They are used to investigate the dissociation of a single chain from the most interacting (with our ligands) end of the Aβ_{42} protofibril.

Although numerous MD studies have examined the basis for the stability of Aβ_{40} fibril, the neurotoxic form of Aβ in AD is Aβ_{42} (Selkoe, 1999). Therefore, it is vital to understand the structural basis for the stability of the Aβ_{42} (Lemkul and Bevan, 2010).

In this chapter the pulling and umbrella sampling simulations using an atomistic model of a five chain Aβ_{42} protofibril in explicit solvent at physiological temperature are generated.

3.6 Methods

3.6.1 Structural preparation

The model used was the core of the Aβ_{42} fibril, this structure was determined using ssNMR by Lührs *et al*., 2015. For PDB ID 2BEG, in the model the N-terminal 16 amino acids (1-16 residues) are missing. However, it has been proposed that residues 17-42 are responsible for the stability of A$\beta_{1\text{-}42}$ fibril (Masman *et al*., 2009). Thus, the observations made, and the conclusions reached are most likely to extend to the full length of the Aβ_{42} fibril. All chains were used in the simulation, but this structure was prepared by applying a rotation matrix so that the direction of pulling could match one of the Cartesian axes (chapter 3, structural preparation).

3.6.2 Pulling and umbrella sampling simulations

The complexes used included the ligands wgx-50, SANC00247, SANC00248, SANC00348 and SANC00415. These are the best binding compounds from the SANCDB database with the exception of wgx-50 (Dock B). Wgx-50 was considered as it is reported as a potential drug candidate in literature (Tang *et al*., 2013). SANC00415 and SANC00348 bind on the surface 2BEG, while the rest of the compounds bind inside the U-shaped 2BEG.

The parameters from AMBER03 (Duan *et al*., 2003) were applied to all simulated systems. The ligand topologies were generated using acypype script (da Silva and Vranken, 2012) within an ambertools environment (Wang *et al*., 2006). All structures were for pulling simulations, by placing them in a rectangular box of simple point charge (SPC) water, to which a neutral concentration of 0.1 M NaCl, and 5 Na counterions were added. The dimensions of the box were ensured to be sufficient enough to satisfy the minimum image convention and provide enough space for pulling simulations to occur along the x-axis without interacting with the periodic image of the system. The COM of 2BEG was placed at (2.0, 2.9, 3.0) in a box of dimensions 12.0×6.0×6.0 Each of the structures were minimized using a steepest descents minimization, with position restraints applied to peptide heavy atoms throughout for the equilibration step. Followed simulating for 100 ps under constant pressure and temperature (NPT) ensemble, with temperature at 310 K. After equilibration, restraints were removed from all chains with the exception of chain D. Since it was being used as an immobile reference for the pulling simulations.

For each of Aβ-ligand (2BEG bound to our ligands) complexes, chain E was pulled away from the core structure along the x-axis. A spring force constant of 1000 KJ mol^{-1} nm^{-2} was used for pulling over 500 ps with a pull rate of 0.1 Å ps^{-1}. From the pulling simulation trajectories, snapshots were taken to generate the starting configurations for the umbrella sampling windows. The window spacing used was 0.2 nm and resulted in 25 windows. In each window, 10 ns of MD was performed for a total of 250 ns for each Aβ-ligand umbrella sampling and Aβ-apo aggregate. Therefore ultimately 1500 ns simulation time was utilized.

Analysis of the results were performed using the weighted histogram analysis method (WHAM).

3.7 Results and Discussion

Figure 22 shows the images of initial structures used in the pulling simulation. The structures were generated after a 100 ps equilibration as mentioned in section 3.6.2. Movie 1 (see supplementary information) illustrates the pulling simulation of $A\beta_{42}$ docked with wgx-50.

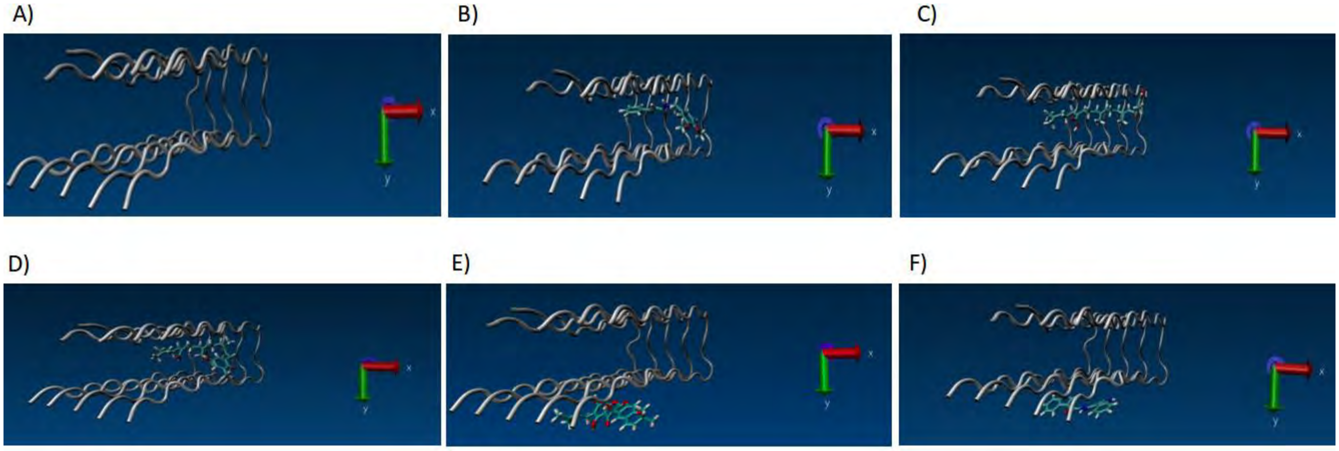

Figure 22: Aβ_{42} aggregate structures after 100 ps NPT equilibration, used as starting structures for pulling simulations, ligands are represented as licorice. A) 2BEG-apo, B) 2BEG-wgx-50, C) 2BEG-SANC00247, D) 2BEG-SANC00248, E) 2BEG-SANC00348, and F) 2BEG-SANC00415. VMD was used to obtain images.

COM pulling simulations are mostly used to bias the functioning of a system to favor a particular phenomenon that might be out of reach on the time scale of traditional MD (Lemkul and Bevan, 2010). COM pulling simulations have been studied on various biological processes, such as protein-protein interactions, protein-ligand, and on extraction of lipids from membranes (Izrailev *et al*., 1998). The applied external force accounts for the ability to determine the work done on the system or by the system. This thermodynamic work is a path-dependent quantity. WHAM is one of the proposed methods used to extract the equilibrium data of the system also known as free energy (Lemkul and Bevan, 2010). The WHAM method determines ΔG from multiple simulations performed on configurations rendered from a single COM pulling simulation (Kumar et *at*., 1992).

The dissociation of chain E in the 2BEG aggregate structure, occurs due to pulling of its COM. A constant pull force is applied at a constant rate, this leads to force building up until a breaking point is reach (Lemkul and Bevan, 2010). The breaking point would not be possible had chain D not been restrained. In each of the pull simulations performed in this thesis, the point of maximum force corresponds to the exact moment when chain D dissociates from the aggregate structure. In Figure 22 the maximum force was reached at 230 ps.

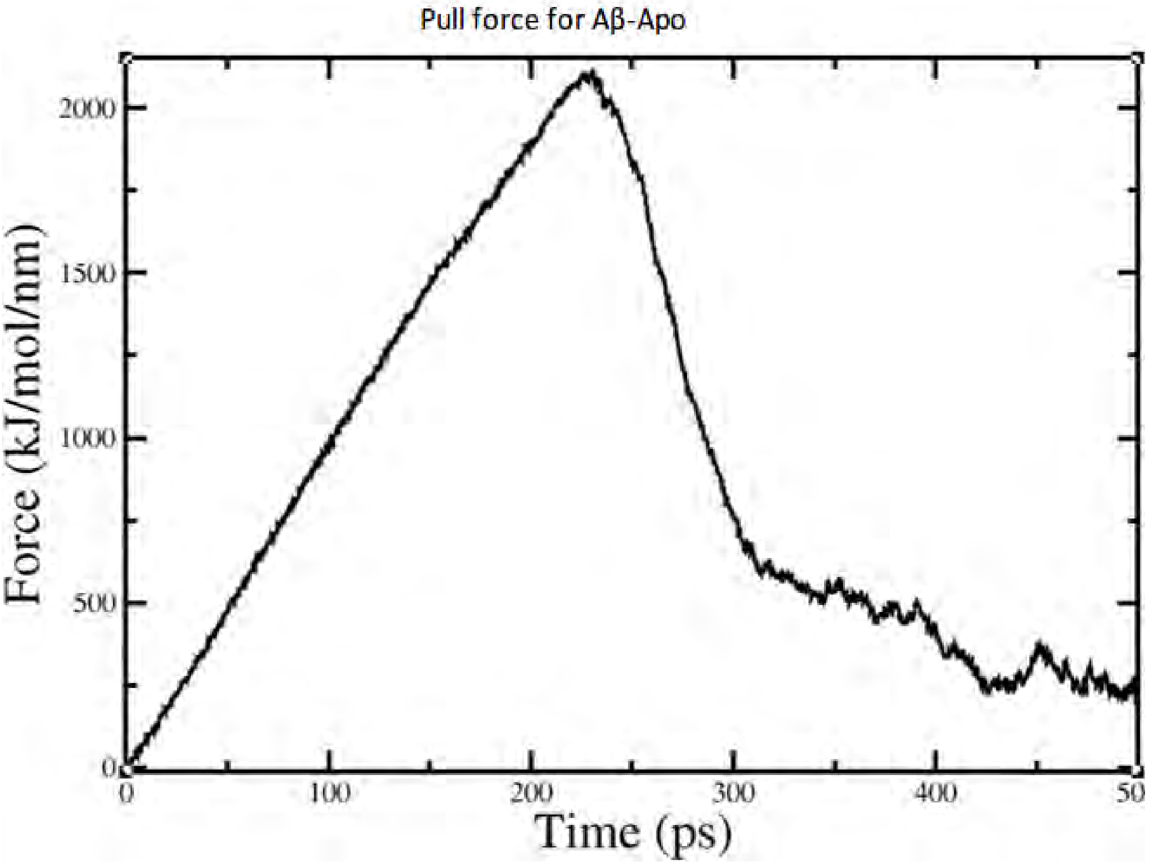

Figure 23: The plot of force vs time graph of the dissociation of $A\beta_{42}$ aggregate. Aβ-apo corresponds to 2BEG without a ligand bound. The plot was generated using Grace.

Since the dissociation is path dependent, the force vs time curves provide insufficient evidence to furnish conclusions on the destabilizing effect of each ligand used, unless the incidents leading up to the dissociation of each system are identical. The major role of the pulling simulation in this thesis is to provide a series of configurations that will be used later for umbrella sampling. Figure 24 shows the dissociation pathway of $A\beta_{42}$ in the presence of the SANCDB compounds.

a) Aβ-SANC00247 b) Aβ-SANC00248

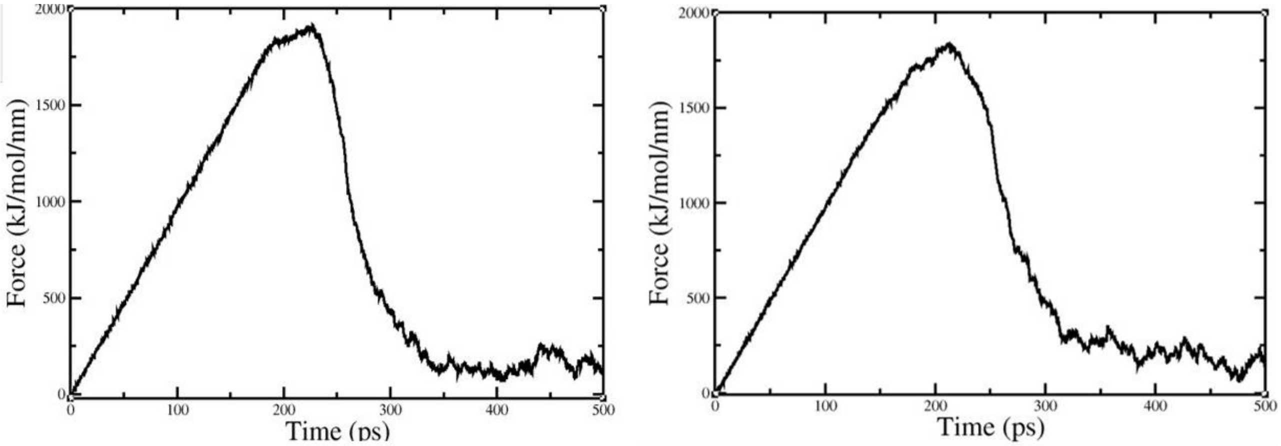

c) Aβ-SANC00348 d) Aβ-SANC00415

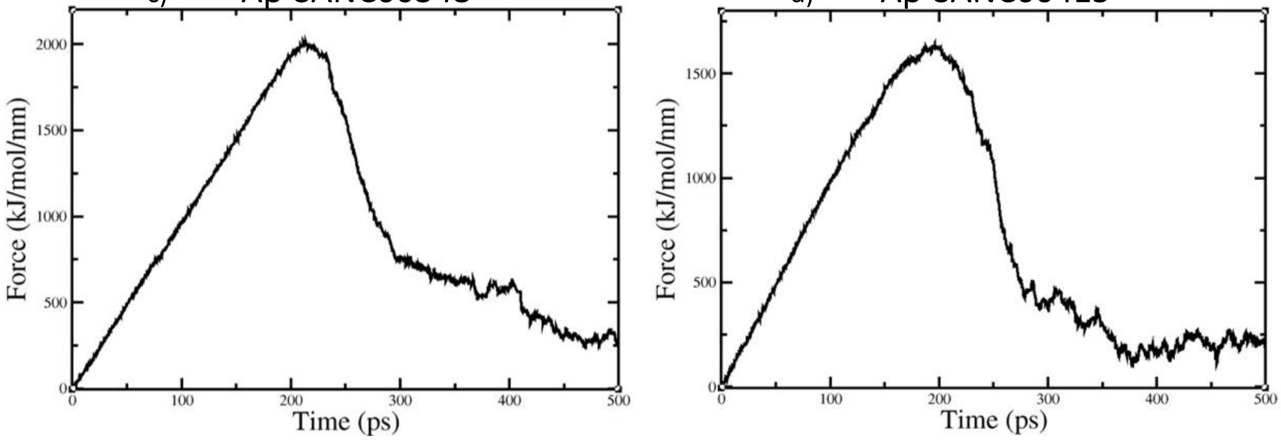

Figure 24: The force vs time graphs showing the dissociation pathway of Aβ42 a) Aβ-SANC00248, b) Aβ-SANC00247, c) Aβ-SANC00348 and d) Aβ-SANC00415

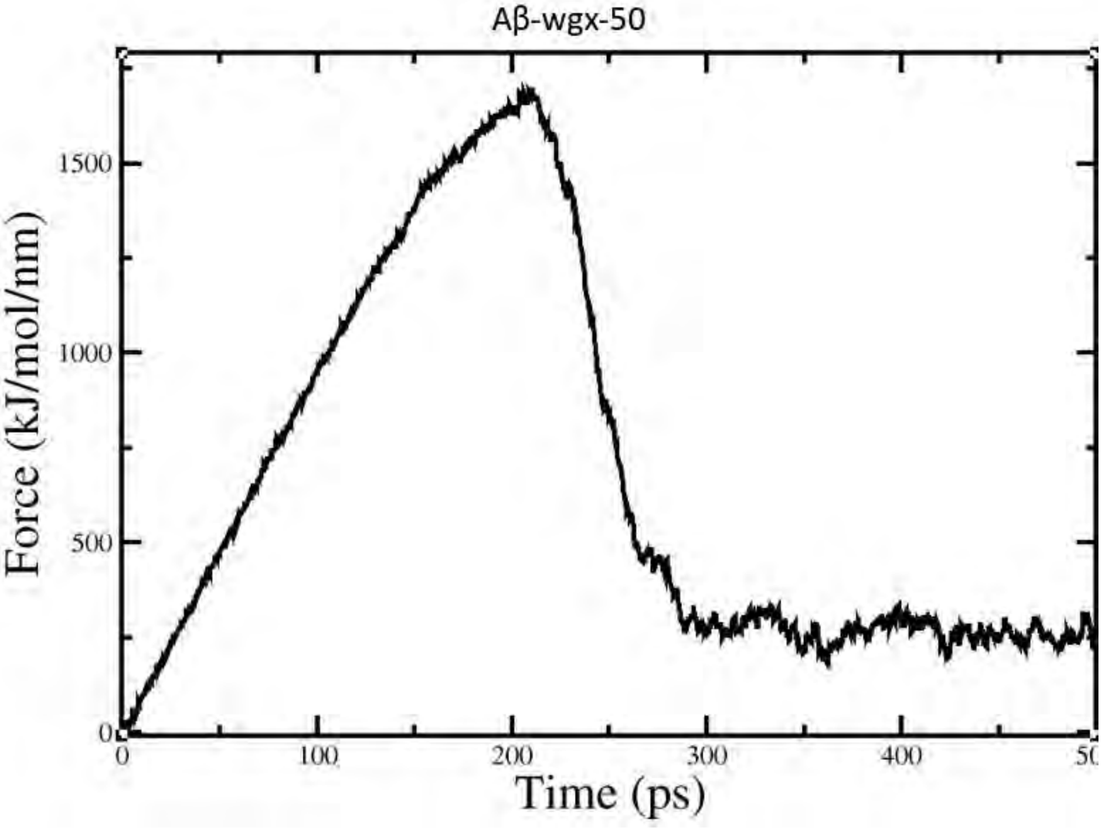

Figure 25: The dissociation of chain E in Aβ_{42} in the presence of wgx-50.

The events leading to the breaking point are different across each force vs time graph in this thesis. The graphs in Figure 24 and 25 as compared to the Aβ-apo dissociation graph (Figure 23), show all require a lower force to dissociate chain E from the aggregate structure. This is also evident in terms of time, the Aβ_{42} aggregate with no ligand present took longer to reach the breaking point than the aggregate with ligands. These results are summarized in table 10 below.

Table 10: Summary of the dissociation point of chain E from Aβ_{42} aggregate structure.

Complex system	**Force (KJ/mol/nm)**	**Time (ps)**
Aβ-apo	2101	230
Aβ-wgx-50	1685	211
Aβ-SANC00247	1909	227
Aβ-SANC00248	1832	213
Aβ-SANC00348	1997	211
Aβ-SANC00415	1625	201

To evaluate the contribution of each ligand effect on destabilizing chain E in the aggregate, we performed umbrella sampling simulations. US are used to determine ΔG of a binding or unbinding process along a specific reaction coordinate. The reaction coordinate in this study is the pulling direction, the x-axis. The PMF curves for each complex system were obtained by using 25 sampling windows along the x-axis (Figure 26). From the PMF curve results, the ΔG of binding for chain E was extracted (Table 11).

The Aβ-apo PMF curve yielded the highest ΔG of binding for chain E, while the Aβ-wgx-50 system produced the lowest ΔG in this study. Interestingly SANC00247 and SANC00248 identified to have similar interactions to wgx-50 in chapter 2, were both compatible with the wgx-50 the drug candidate in terms of ΔG (Table 11 and Figure 26). Exploration of the residues that these three compounds interact with, namely Leu34, Val36, Ala21, and Glu22 may account for the destabilization of Aβ_{42} stabilizing residues.

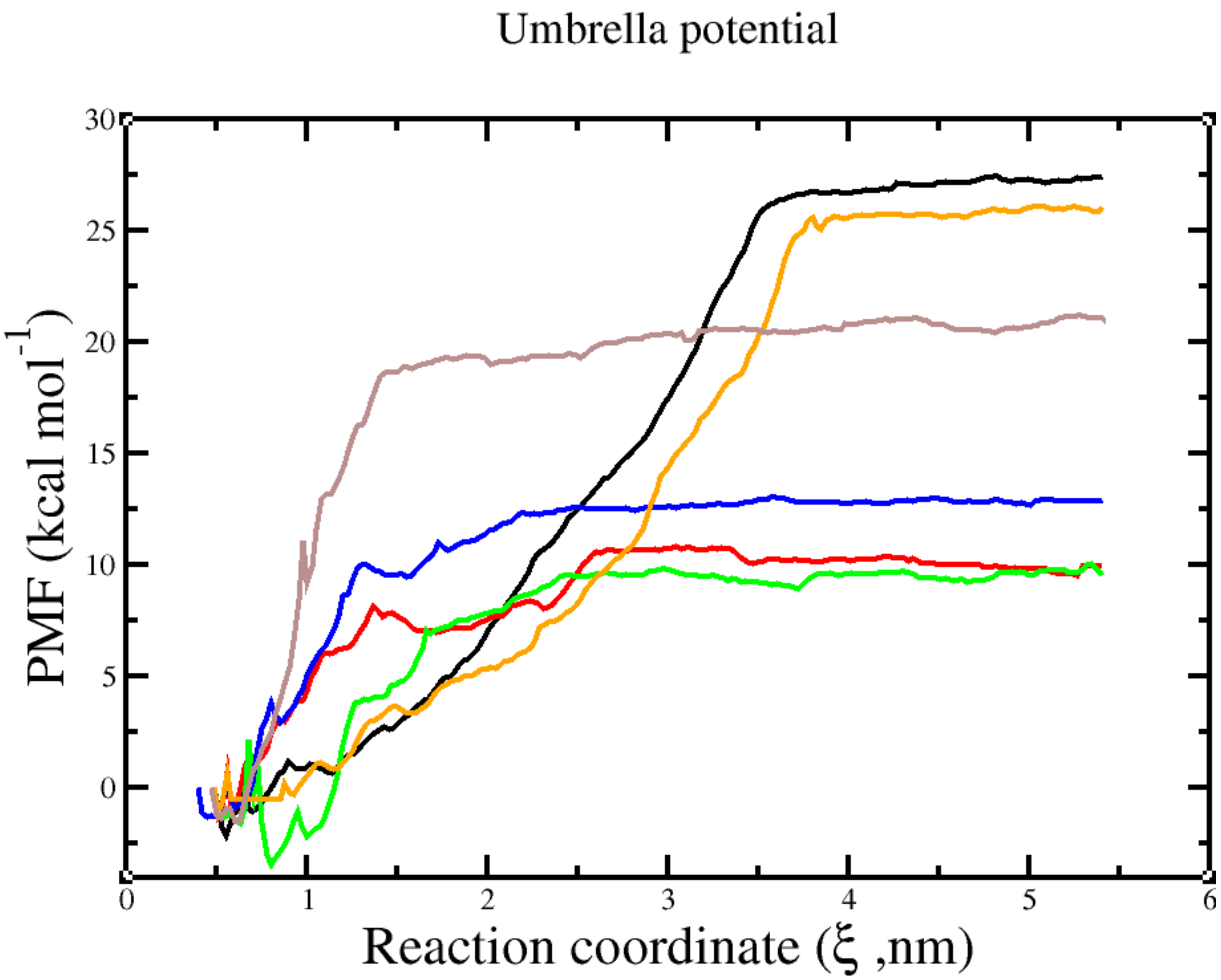

Figure 26: Potential of mean force (PMF) curves, black (Aβ-apo), red (Aβ-wgx-50), green (Aβ-SANC00247), blue (Aβ-SANC00248), orange (Aβ-SANC00348) and brown (Aβ-SANC00415).

An effective US simulation consists of several sampling windows with as much overlap between neighboring windows as possible (Mills and Andricioaei, 2008). Figure 26.1 shows the Aβ-apo 25 window umbrella sampling after 10 ns simulation per window.

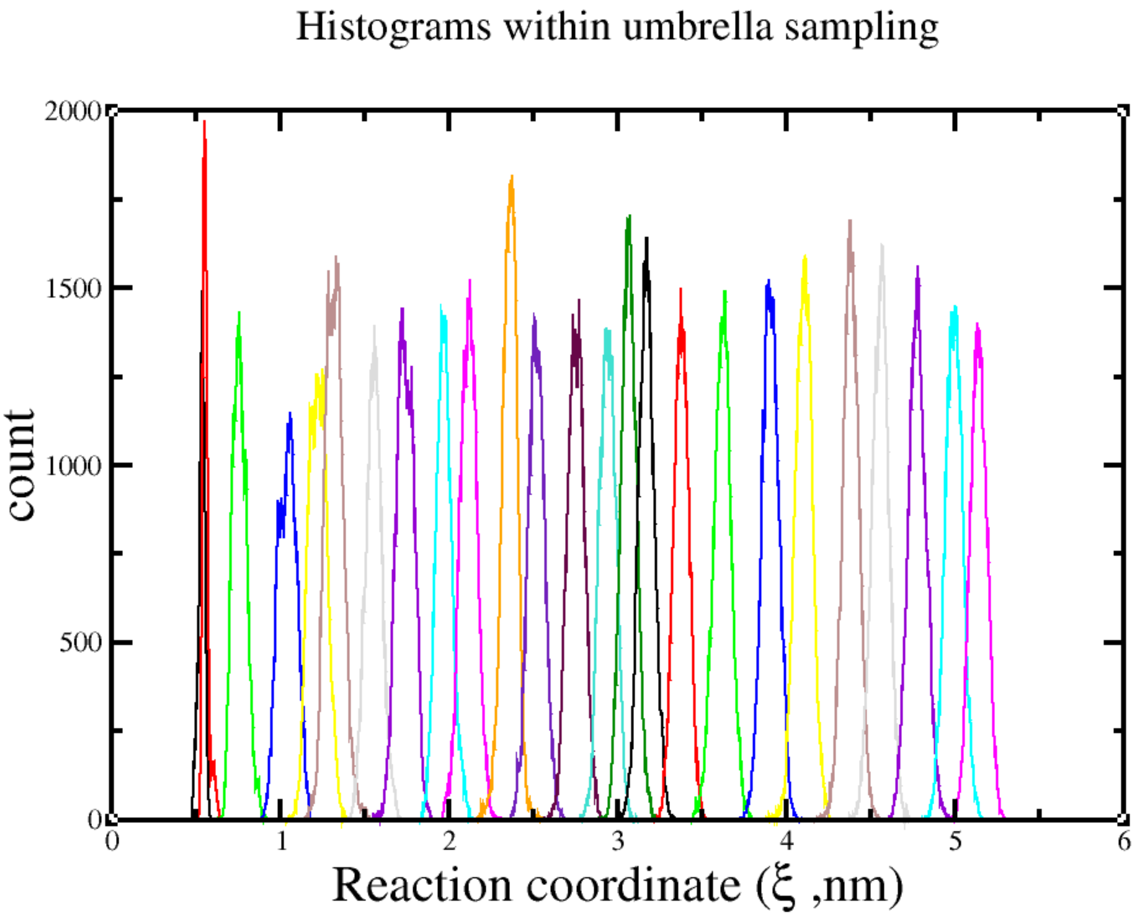

Figure 26.1: The 25 window umbrella sampling histograms for Aβ-apo.

In Figure 26.1 there is sufficient overlap between neighboring windows from 0.8 to 5.1 nm of COM spacing. However, the overlap around 0.5 nm suggest that one or two further sampling windows may increase the accuracy of ΔG further.

Table 11: The binding free energies (ΔG) for each of the aggregates in this thesis.

Complex system	**ΔG (Kcal/mol)**	**PMF colour**
Aβ-apo	30.11	Black
Aβ-wgx-50	11.95	Red
Aβ-SANC00247	13.5	Green
Aβ-SANC00248	14.3	Blue
Aβ-SANC00348	27.18	Orange
Aβ-SANC00415	22.74	Brown

These are promising results in terms of SANCDB compounds. Two compounds (SANC00247 and SANC00248) lower the binding free energy of the final chain to close to that of the wgx-50-based destabilization. This is in the light that both of these compounds only fail one of the Lipinsky rules (the logP is close to 6 in both cases). As such these two compounds may form the basis as potential lead compounds in the search for Aβ destabilizers.

Chapter 4: Charmm simulation with copper and zinc

4.1 Introduction

Bio-metals copper (Cu) and zinc (Zn) are extremely important for brain function (Choo and Grubman 2017). The aggregation of Aβ is mediated by the interaction of metals, notably Cu, Zn and iron (Fe) (Maynard *et al.*, 2005). Zn and Cu have low oxophilicity while Fe is moderately oxophilic. These metals often bind to nitrogen and sulfur-donor ligands, however they can also bind oxygen (Kepp, 2016). Zn exerts a direct control over the Aβ balance in terms of production and degradation via zinc peptidases (Kepp, 2012). Its concentration in the brain is estimated at 150 µM, which is 10 times higher than the concentration in serum (Andreini, 2006). Almost all of the brain Zn is tightly bound in metal-protein complexes to achieve enzymatic activity or structural stability, while the loosely bound Zn is present mainly in areas associated with memory and learning (Huang, 1997). Cu ions bind to Aβ peptides with high affinity and increase the proportions of β-sheet and α-helix structures in amyloid peptides. These structures may be responsible for Aβ aggregation (Atwood *et al.*, 2000, Dai *et al.*, 2010), while binding of Cu to Aβ increases Cu's toxicity to cells (Sarell *et al.*, 2010).

In this chapter molecular dynamics (MD) simulations were performed on three $A\beta_{42}$ structures, carried out in the presence of Cu(II) and Zn(II). It has been reported by numerous scholars that Aβ contains a high-affinity metal-binding region at residues 1-16, which includes histidine residues as well as other groups such as aspartic acid and glutamic acid that can coordinate metal ions (Kepp, 2012, 2017; Hureau and La Penna, 2014; Faller and Hureau, 2009; Kozin *et al.*, 2001; Curtain *et al.*, 2001). However, almost all the postulated Cu and Zn binding residues have been reported for a single chain of $A\beta_{42}$; to the best of our knowledge, only one report of MD simulations on Cu(II)-Aβ fibrillated multiple chain system has been reported in the literature (Carlisle, MSc thesis 2018). Our initial focus is was study the dynamic nature of the of Cu(II) and Zn(II) on the Aβ fibrillated chain system. These results along with the QM/MM studies to be performed aim to provide insight on revealing the formation mechanism of pathogenic Aβ aggregates.

CHARMM stands for Chemistry at HARvard Molecular Mechanics. it is a general and flexible molecular simulation and modeling program. It is widely used and uses both classical and quantum mechanical energy functions (Brooks *et al.*, 2009). The name CHARMM also refers to a set of force fields for molecular dynamics simulation and analysis. Over the years, CHARMM software has been modified to run on many different machines and platforms. This modification includes both serial and parallel implementations of the code. In the present age CHARMM can run on single-processor PCs, Mac and Linux workstations, to machines based on vectorial or multi-core processors. It is also compatible to distributed-memory clusters of Linux machines and large shared-memory super-computer installations (Brooks *et al.*, 2009). The CHARMM simulation program is used for studying the structure, energetics, and properties of molecular systems (Becker and Karplus, 2006).

4.2 FindGeo

FindGeo is a tool for determining coordination geometry of metals in biological macromolecules with known structures. It is available freely as a web server and as a stand-alone program. FindGeo is written in both Fortran and Python, and it uses PDB files as input. The coordinating atoms to the metal are identified using a threshold distance of 2.8 Å (default parameter). Metal coordination is determined by comparing a library of structural templates with ideal geometries. Various probable geometries are tagged as regular, distorted or irregular, based on the root-mean-square deviation (RSMD) values obtained after superposition. The best estimate of the metal coordination has the lowest RMSD, a geometry is not assigned when all possible geometries are tagged as irregular. The template structures in FindGeo's library has geometries for coordination numbers 2-9, including geometries derived from 2-9 coordination numbers because of an empty position (Andreini *et al*., 2012).

The RMSD criteria for tagging geometries is based on using RMSD as a metric for estimating similarities between the overall arrangement of metal coordinating atoms and other potential geometries. The alternative geometries are ranked based on RMSD value, Andreini *et al*., 2012 reported that this ranking allows quantitative comparison of potential geometry assignments. Thus, the RMSD value produced by FindGeo may be understood as the distance between the actual geometry of the query PDB and an idealized geometry (Andreini *et al*., 2012).

4.3 Methods

4.3.1 Molecular models

In order to reduce simulation time, and further to simulate an infinite fibril of Aβ, the number of stacked chains in the NMR-derived fibril was reduced, and periodic boundary conditions were introduced. The twelve chains of the 2MXU PDB structure, each lacking the first 10 amino acids of $A\beta_{42}$, was reduced to four chains. Given that spatially it is impossible for metals to bind to residues on more than two chains simultaneously, this number of chains was deemed to be more adequate for this type of simulation. The chains chosen were F-I, as they were more uniformly orientated, and given the that molecular dynamics equilibration was to be used to remove any artefacts from the construction of this model. Similarly, the five peptide chains of the 2BEG PDB structure were also reduced to four chains, chain A-D. However, for the 2NAO PDB structure which consists of a double filament of 3 chains each (explicitly discussed in the results section), chain A from the first filament was chosen and repeated four times to match 2MXU and 2BEG. Disorder in the chains of 2NAO made this approach necessary; in this approach no overlap of atoms is introduced when periodic boundary conditions are set. Four chains of each PDB structure were also used to keep them consistent with each other and, as previously mentioned, to reduce computational cost. Inspection and initial processing of chains was done using Discovery studio visualizer (DSV) program version 4.5. Of the various multi-models of these structures, the first model was chosen for use, also given that the intention was to use molecular dynamics equilibration to remove artefacts of construction.

4.3.2 Structural preparation

All three structures were submitted to H++ (Virginia Tech), to add missing hydrogen atoms, and obtain protonation states of each amino acid in the chain at pH 7.4. The periodic boundary conditions (PBC) for these structures were computed using a python script, which aligned the fibrils so that the average C_α-C_α vector was aligned with a Cartesian axis, and such that the average C_α-C_α interatomic distance was matched within the PBC (see appendix 6). The script was constructed to read in the 3D structure and to perform calculations only using coordinates of the alpha carbons. This script locates the distances between each chain by subtracting the xyz coordinates of corresponding atoms from adjacent chains. The average distance is determined for each chain in the structure, these distances are than used to calculate an average displacement vector **V**. This vector is used to determine an angle θ with respect to the x-axis (the **OX** vector where **O** is the origin). Further a cross product of three normalized unit vector ||V|| with **OX**, provides a vector **U**. Given the rotation of the full system about **U** through the angle θ aligns the fibril to the x-axis, the script then finally produces the rotation matrix from P and θ that will effect this rotation, and details of the periodic box that maintains the correct chain distance across the boundary. For easy access to visualization of the PBC, the rotation matrix was applied to the system in DSV to transform the PDB structures to be perpendicular with respect to (w.r.t) the A length, and parallel w.r.t the B length of crystal cell.

$$R = \begin{bmatrix} \cos\theta + u_x^2(1-\cos\theta) & u_x u_y(1-\cos\theta) - u_z\sin\theta & u_x u_z(1-\cos\theta) + u_y\sin\theta \\ u_y u_x(1-\cos\theta) + u_z\sin\theta & \cos\theta + u_y^2(1-\cos\theta) & u_y u_z(1-\cos\theta) - u_x\sin\theta \\ u_z u_x(1-\cos\theta) - u_y\sin\theta & u_z u_y(1-\cos\theta) + u_x\sin\theta & \cos\theta + u_z^2(1-\cos\theta) \end{bmatrix}$$

R is the rotation matrix applied, where θ is the angle about the perpendicular vector **U** (u_x, u_y, u_z); as a check the determinant of the rotation matrix was determined to be equal to 1.

4.3.3 CHARMM molecular dynamics

Once the script was set up with PBCs, this information was taken through to CHARMM simulations. The first input script required was for setup (Setup.inp), this script requires the input of each of the four chains to be inputted separately. However, since residue numbering across the chains has to be precise as input within CHARMM, a Perl script was used to renumber the residues in the separate PDB chains from residue 1 on the first chain with no repeating residue number (see appendix 7), vacuum minimization was effected, initiated by a 100-step energy minimization run using the steepest descent (SD) algorithm and followed by a 1000-step minimization run using the adopted basis Newton-Raphson method (ABNR). The orthorhombic crystal cell parameters (in Å) for 2MXU were (19.45 60.00 60.00), 2BEG (18.46 60.00 60.00) and 2NAO (20.48 70.00 70.00). These crystal cell parameters were used within all subsequent steps. The structures were then solvated in the orthorhombic box of pre-equilibrated waters (TIP3). After successful solvation, the systems were neutralized in KCl, but simulations were also set up using the CuCl and ZnCl. The Lennard-Jones parameters for Cu^{2+} were obtained from Moses *et al*., 2017. All neutralized systems then underwent their final minimizations. After all these steps, the systems underwent molecular dynamics, heating, equilibration and production runs.

4.3.4 FindGeo metal coordination geometry

Five Aβ_{42}-metal coordination complexes were investigated. Informed by molecular dynamics of the CHARMM MD simulations, together with information from literature, Cu^{2+} ions were localized to 2NAO His14 (chain A and B), Asp23 (chain A and B), Glu22 (chain B and C), Met35 (chain B and C) and Ala42 (chain B and C) residues. His14 and Asp23 residue have been reported as metal binding residue (Savelieff, *et al*., 2014, Atrián-Blasco *et al*., 2018, Cassagnes *et al*., 2013), Cu had been shown to localize Met35 during MD simulations (Carlisle, MSc thesis 2018); investigating Aβ_{42} metal binding residues is vital for determining mechanism of ROS formation in AD. In these MD simulations performed, no Cu localization was observed to a specific residue was observed. This was attributed to the difference in total simulation time between these simulations and those performed by T. Carlisle. However, since observation of binding is limited under these conditions by diffusion, the concentration of Cu^{2+} and the random location of ions at the start of simulation, the possible binding residues a more directed approach was followed. To this end simple harmonic patches were setup between Cu atom and pairs of residue atoms (one per chain) and these systems optimized. Water was allowed to move freely, and the resultant water geometry was consistent with expected hydration of the metal center. This was repeated for five pairs of Aβ_{42} residues to achieve five possible Cu-Aβ complexes.

Table 12 also confirmed the choice of residues with which to localize the Cu^{2+} ion; the "patch" command was applied in the CHARMM vacuum minimization script to direct Cu^{2+} ion to a residue. Cu-O and Cu-N force constants were obtained from Moses *et al*., 2017 (see appendix 8).

The five complexes were then submitted to FindGeo using the default distance threshold.

4.4 Analysis

The structures were loaded onto the Visual molecular dynamics (VMD), version 1.9.4a31. The trajectories of both Cu and Zn neutralized systems were analysed. The last frame trajectories after MD simulations for, Cu and Zn within 4 Å distance were reported in table 1 and table 2 respectively.

4.5 Results and Discussion

In CHARMM, there are two methods for enforcing periodic boundary conditions (PBC). The first is the well-known minimum image convention, whereby each atom *i* interacts with the version of atom *j* closest to *i.* The other (used in this study) generates replicas of the main simulation cell and its atoms (Seminario and Balbuena, 1999). Initial work with 2NAO resulted in an overestimation of the x-dimension of the periodic box. This was due to extensive disorder in the chains (A-C) resulting in a much longer average C_α-C_α distance. This structure had further issues; under PBC it was evident that there was overlapping of chains after performing MD simulations (Figure 27C). A new 2NAO structures was constructed, new-2NAO, by editing the original 2NAO to four chain A's. The former under PBC showed an overlapping of chains after performing MD simulations (Fig.27C). Figure 27 shows the final structures after MD simulations of 2MXU, 2BEG, 2NAO and new-2NAO, under PBC the main simulation cell is enclosed by the purple box. The new-2NAO structure was validated by monitoring interchain C_α pairs across the periodic boundary conditions during the course of equilibration. A stable interchain distance was observed, contrary to the case of the original 2NAO structure.

A. 2MXU

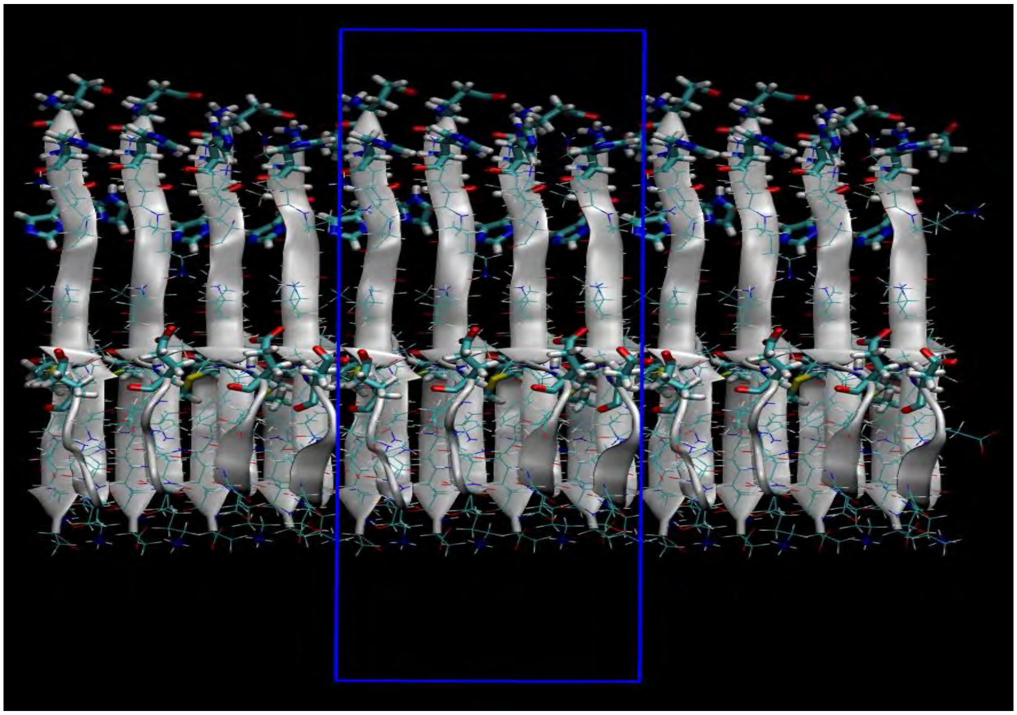

B. 2BEG

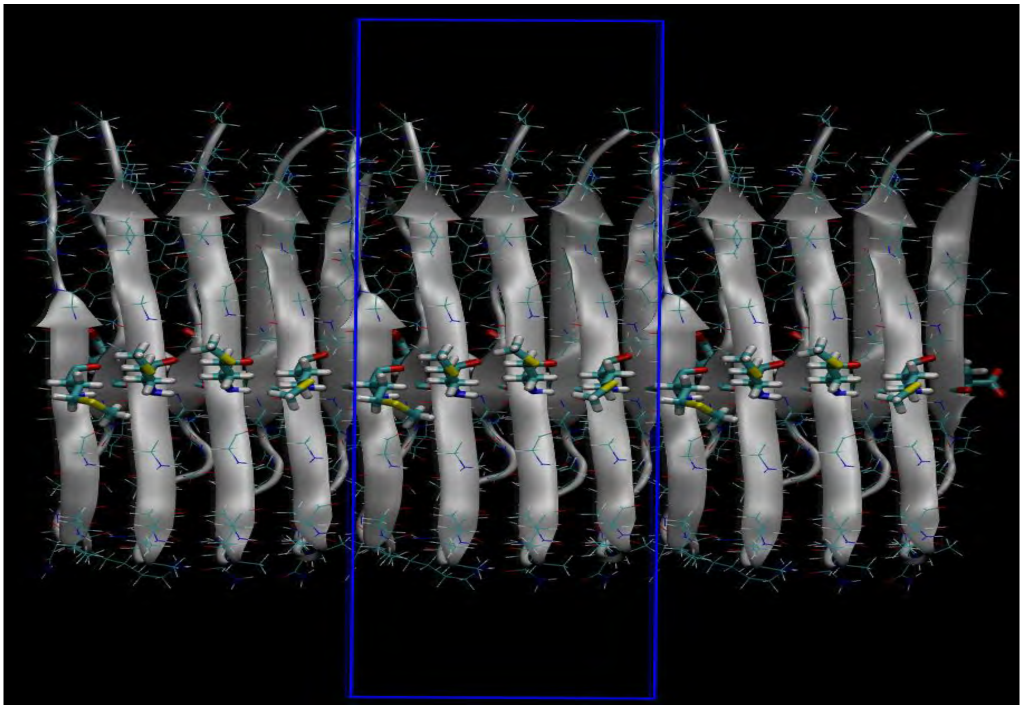

C. 2NAO

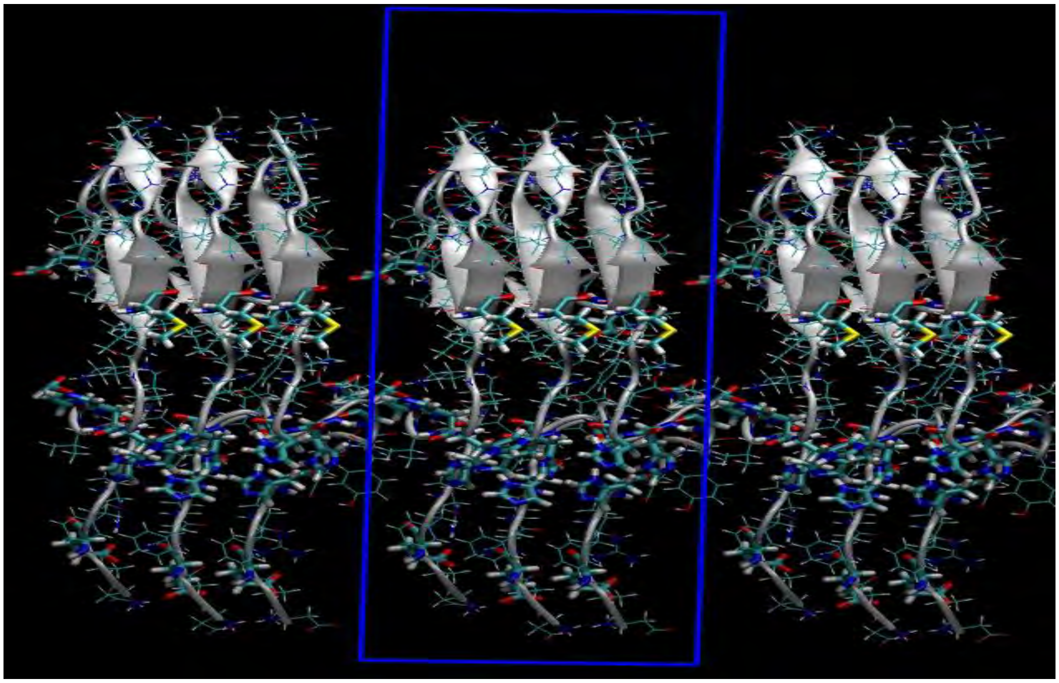

D. new-2NAO

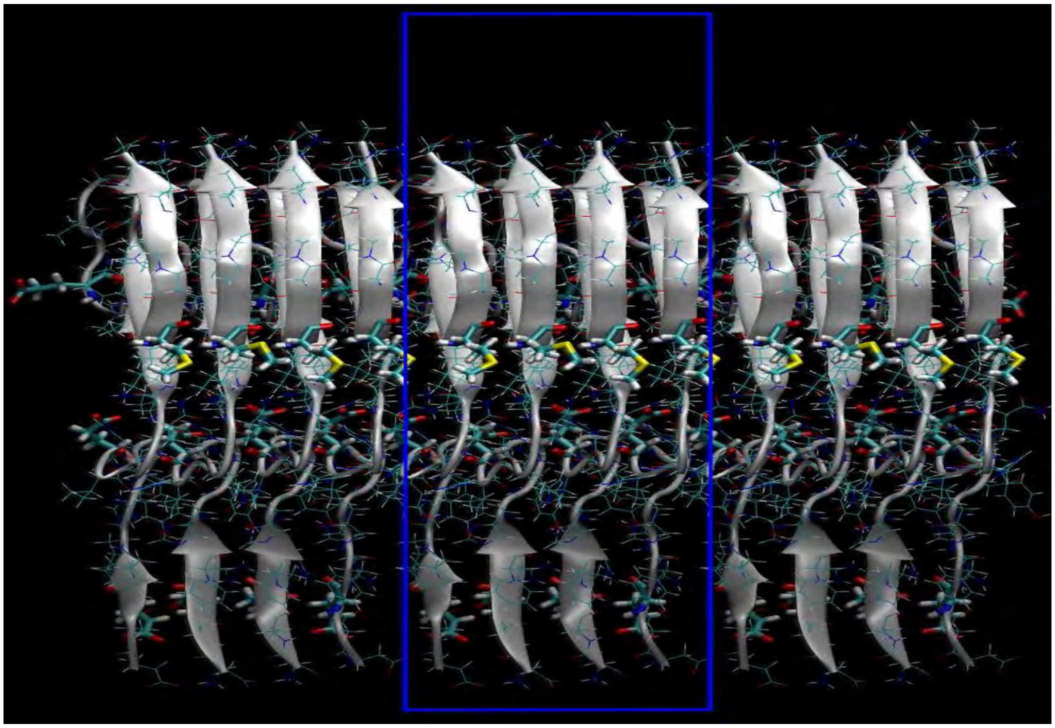

Figure 27: The cartoon structures of A) 2MXU, B) 2BEG, C) 2NAO and D) new-2NAO with their PBC, glutamic acid and methionine residues represented in bond form.

The new-2NAO will be referred to as 2NAO from this point onwards for the sake of clarity. The results obtained from CHARMM simulation with dication neutralized allowed the investigation of the diffusion of the Cu and Zn ions throughout the simulation. Figure 28 shows an overlay of copper atoms in all trajectory frames, illustrating the localization of Cu during MD. This localization is driven by only two force-fields terms – the van der Waal's and electrostatic terms. The residues highlighted are MET, GLU, ASP and HSD as these residues are proposed to bind Cu ions (Carlisle, MSc thesis 2018, Furlan *et al*., 2015, Hureau, 2012).

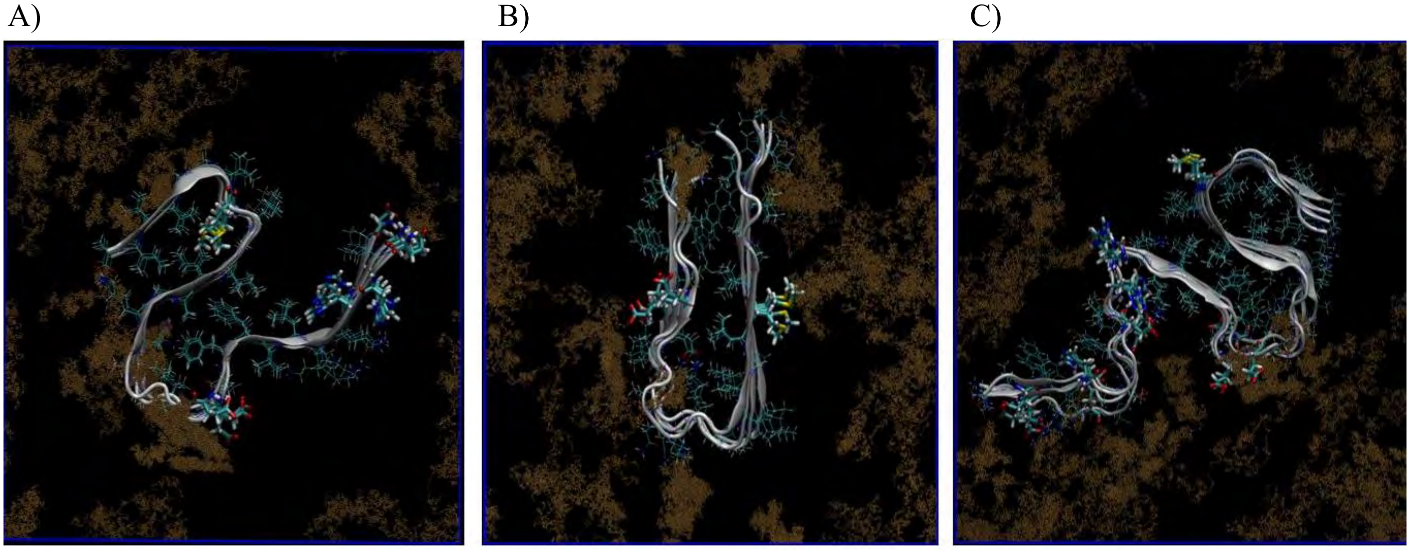

Figure 28: Images of the structures after Charmm MD simulation, showing the diffusion of Cu ions, A) 2MXU-Cu, B) 2BEG-Cu and C) 2NAO-Cu.

Further analysis was done by using the VMD tool to analyze the Aβ-metal distance. We analyzed the distance within 4 Å to confirm the diffusion images (Fig.28 and Fig.29). The results were than presented in table 12 and 13.

Table 12: The residue interaction distance between Aβ and Cu^{2+} ion

3D structure	Residue name	Chain	Distance in Å
2MXU	Glu22	B	4.03
	Asp23	D	3.50
	Ala42	D	3.71
	Glu22	A	4.01
	Asp23	C	4.02
	Glu22	D	4.05
	Ala42	B	4.02
	Gly25	A	3.71
	Asp23	A	3.95
	Val40	D	3.82
2BEG	Glu22	C	3.58
	Glu22	B	3.63
	Ile31	D	3.95
	Met35	C	4.08
	Leu34	D	4.04
	Val40	A	4.09
	Ala42	A	4.02
2NAO	Asp7	A	3.93
	Asp23	C	3.82
	Asp7	B	3.68
	Asp23	A	3.59
	Asp7	B	3.90
	Ser8	B	4.01
	Ser8	C	4.09
	Glu22	A	3.84
	Glu22	B	4.08
	Arg5	C	4.07

Figure 29 shows an overlay of zinc atoms in all trajectory frames, illustrating the diffusion of Zn^{2+} during MD simulations.

A) B) C)

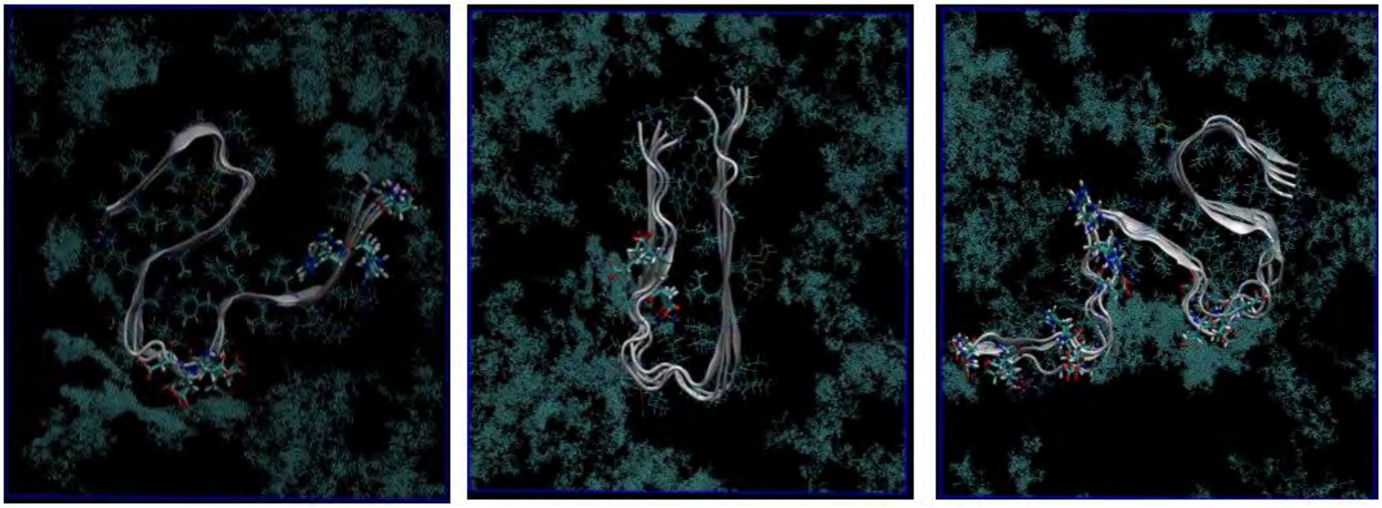

Figure 29: Images of the structures after Charmm simulation, showing the diffusion of Zn ions, A) 2MXU-Zn, B) 2BEG-Zn and C) 2NAO-Zn.

Table 13: The summary of residue interaction distance between Aβ and Zn^{2+} ion

3D structure	**Residue name**	**Chain**	**Distance in Å**
2MXU	Asp23	C	3.92
	Gly25	D	4.04
	Asp23	D	4.08
	Asp23	C	4.01
	Glu11	C	3.84
2BEG	Glu22	C	3.52
	Glu22	B	4.03
	Ala42	C	3.83
	Val24	A	4.01
	Val24	B	4.02
2NAO	Asp7	C	4.07
	Ala21	A	4.07
	Glu22	C	4.03
	Asp23	C	4.04
	Asp23	B	4.01
	Glu22	C	4.06
	Leu34	A	4.09
	Glu3	B	4.03

The results from FindGeo web server comprise of numerous PDB files containing the metal site superimposed to each ideal geometry. Table 14 summaries the best geometry obtained for the five Aβ42-Cu^{2+} used.

Table 14: The results obtained from FindGeo of the Cu^{2+} five explored coordination

Cu bound residue	**Best geometry**	**Tag**	**RMSD**
His14	Octahedron	Distorted	0.759
Glu22	Square antiprism with a vacancy	Distorted	0.591
Met35	Octahedron, face monocapped with a vacancy	Irregular	0.855
Ala42	Square antiprism	Distorted	0.717
Asp23	Pentagonal bipyramid with a vacancy	Distorted	0.584

His 14 the lowest RMSD is an octahedron, face monocapped. However, the best geometry is not the lowest RMSD in this case (see supplementary information). FindGeo was not able to predict the coordination of Cu^{2+} ion Cu-Met35, as a result all possible geometries were tagged as irregular (see supplementary information).

Chapter 5: Optimization of Aβ-copper with ONIOM and QM/MM molecular dynamics

5.1 Introduction

Hybrid techniques that combine two or more computational methods in one calculation allow the accurate exploration of the chemistry of very large systems (Vreven *et al*., 2003). The QM/MM methods combine a quantum mechanical (QM) method with a molecular mechanics (MM) method (Gao, 1996). The development of the hybrid QM/MM approaches is guided by the general idea that large chemical systems may be partitioned into an electronically important region which requires a QM treatment and the rest which only requires a classical description (Bakowies and Thiel, 1996). The QM treatment allows modeling of the electronic rearrangements involved in the breaking and forming of chemical bonds, while the MM treatment allows for the efficient inclusion of the wider environment and its effects on the reaction energetics (Kamp and Mulholland, 2013).

QM/MM approaches can use either subtractive or additive schemes (Senn and Thiel, 2009). The energy in the subtractive QM/MM scheme (Eq.1) is obtained by a MM calculation of the entire system (S) with the inner part (I) cut out and replaced by a QM calculation (Culka *et al*., 2017).

$$E^{Sub} = E_{MM}(S) + E_{QM}(I) - E_{MM}(I) \qquad \text{Eq.1}$$

The QM energy of the quantum mechanically treated inner part ($E_{QM}(I)$) is added to the MM energy of the entire system ($E_{MM}(S)$), however the MM energy of the inner part ($E_{MM}(I)$), has to be subtracted to avoid double counting (Culka *et al*., 2017). The most widely used approach that uses the subtractive scheme is ONIOM (Svensson *et al*., 1996). The ONIOM is able to combine *n* (any counting number) layers of any implemented QM or MM approach. The advantage with this approach is the simplicity, as it automatically ensures that no interactions are double counted and it can be set up for any QM and MM software, without the need of any modification of the code (Cao and Ryde, 2018)

In the additive QM/MM scheme, the MM energy is only calculated on the outer system (O) instead of the entire system (S) (Eq.2). The QM energy ($E_{QM}(I)$) is added and plus an introduction of a coupling term ($E_{QM/MM}(I, O)$) is added. This coupling term treats the interaction of the QM and the MM part (Culka *et al.*, 2017).

$$E^{add} = E_{MM}(O) + E_{QM}(I) - E_{QM/MM}(I, O) \qquad \text{Eq.2}$$

The coupling term is composed of Van der Waals, electrostatic, and bonded contributions. The advantage of the additive QM/MM scheme is that no MM parameters for the QM atoms are needed, because those energy terms are calculated by QM (Cao and Ryde, 2018)

The misfolding of Aβ into toxic conformations is proposed to be at the molecular foundation of AD (Orcellet *et al.*, 2011). Thus, there is a major interest in understanding the structural and toxicity features of Aβ aggregation pathway. This is because if we understand the structural and molecular basis behind the aggregation pathway of $A\beta_{1-42}$, it will advance the design of therapeutic strategies.

5.2 Application of QM/MM

5.2.1 Potential energy surface

A potential energy surface (PES) is a plot of the energy of a collection of nuclei and electrons against the geometric coordinates of the nuclei (molecular energy versus molecular geometry). In Mathematical terms the PES may be regarded as the equation that gives the energy as a function of nuclear coordinates. PESs are important as they assist in visualizing and understanding the relationship between potential energy and molecular geometry. They are also vital in understanding how computational chemistry programs locate and characterize structures of interest (Berger, 2004). Stationary points are the most important features of PESs for discussing chemical reactions. These features on PESs are identified as points at which surfaces are flat. Mathematically, a stationary point is described as a point in which the first derivative of the potential energy with respect to each geometric parameter is zero (Eq.3).

$$\frac{\partial V}{\partial q_1} = \frac{\partial V}{\partial q_2} = \ldots = 0 \qquad \text{Eq.3}$$

The stationary points can be further distinguished by the second derivatives of the potential energy in terms of the internal coordinate. Depending on the number of positive, negative and zero eigenvalues of the Hessian matrix. The stationary points can be characterized as minima, transition states or hilltops (Li, 2014).

An important aspect of Cu-Aβ interactions related to AD, is the catalytic role of Cu in the production of ROS (La Penna *et al.*, 2013). In the presence of a physiological reductant like ascorbate and under aerobic conditions, Cu-Aβ catalyzes the production of H_2O_2 and HO• (Guilloreau *et al.*, 2007).

Aβ + $M^{(n+1)+} \rightarrow$ Aβ + M^{n+} (reduction of the metal ion)
$M^{n+} + O_2 \rightarrow M^{n+1} + O^{-}_2$
$O^{-}_2 + O^{-}_2 + 2H \rightarrow H_2O_2 + O_2$ (production of H_2O_2)
$M^{n+} + H_2O_2 \rightarrow M^{(n+1)} + O^{-}_2 + HO\bullet + HO^{-}$ (Fenton chemistry)
$O^{-}_2 + H_2O_2 \rightarrow, HO\bullet + HO^{-} + O_2$ (Haber-Weiss reaction)

5.2.2 Born-Oppenheimer molecular dynamics

Born-Oppenheimer molecular dynamics (BOMD) is a MD simulation carried out on *ab initio* PES, characterized by determining the electronic ground state and energy at every time step (Payne *et al.*, 1992). The first BOMD simulation using *ab initio* PES was reported in 1978 by Leforestier, and they used the Hartree-Fock approximation and the STO-3G basis to describe the gas phase reaction $H^- + CH_4 \rightarrow CH_4 + H^-$ (Wang and Song, 2019). In BOMDs, it is assumed that the adiabatic and the Born-Oppenheimer approximations are valid and that the nuclei follow a semiclassical Newton equation whose potential is determined by the Ehrenfest theorem (Paquet and Viktor, 2018). The adiabatic approximation assumes that the electronic wave functions adapt quasi-instantaneously to a variation of the nuclear configuration. This assumption is justified by the fact that the nucleus is much heavier than electrons (Broeckhove and Lathouwers, 1992). The Born-Oppenheimer approximation further assumes that the electronic and nuclear motions are separable as a result of the difference between nuclear and electronic masses (Paquet and Viktor, 2018).

BOMD can provide insights into chemical reaction mechanisms independently of mechanistic hypotheses, since individual reaction events can occur naturally by integrating the equations of motion (Wang and Song, 2019). BOMD is computationally expensive, due to the evaluation of *ab initio* PES at each time step. Another BOMD limitation is the self-consistent field equations that are needed to solve *ab initio* PES, these equations may fail to converge (Payne *et al.*, 1992).

Meliá *et al.*, 2013, conducted a computational investigation of the Peptidylglyine a-Hydroxylating Monooxygenase (PHM) mechanism by employing hybrid density function theory and molecular mechanics (DFT/MM) calculations coupled to BOMD simulations. Their main objective was to determine the evolution of cupric-hydroperoxide intermediate which is formed upon the transfer of a hydrogen atom by the cupric-superoxide intermediate. Their BOMD allowed them to understand how fast reactive steps occur at the enzyme active site, which is not possible with current experimental approaches.

5.3 Methods

GaussView version 5.0.9 was used for creation of Gaussian input files and interpretation of output files. Optimization and bond scans were determined by employing the ONIOM model as implemented in Gaussian 09, Revision E01, with the high layer calculated using a Semiemperical (PM6) approach and the low layer using MM with the universal force field (UFF). The high layer consisted of the Cu and the side chains of the two residues to which copper was bound, together with the proximal water molecules (as mentioned in section 4.3.3). The remaining bulk system was set to calculation at the low layer in the two layer ONIOM setup.

In a single calculation BOMD Cu simulations were performed where Cu was bound to two Glu22 residues. The high layer for this particular calculation was at the DFT (B3LYP) level with basis set 6-31G(d), while the low layer was at the MM level (using UFF). This sytem was a good choice for BOMD since firstly, the Glu22 residue was a residue observed to interact with destabilizing SANCDB compounds. Secondly, since these metals have also been implicated in the aggregation process for Aβ, exploration of bonding and exchange processes are interesting within this context. Finally, no studies have explored this bonding, to confirm or refute the possibility of binding to this position.

5.3.1 PES scan setup

Another aspect to be explored was the formation of reactive oxygen species (ROS). In the literature although studies have involved Cu-HIS complexes, to our knowledge no study of the complete Cu-HIS mediated formation of ROS is available.

Dioxygen was added to a Cu bound to two His14 residues and 4 proximal water (bound to two His on separate chains). Bond scans were performed to allow the oxygen to become bound to the copper, as the first step in the formation of ROS. However, the multiplicity of the QM system was deemed important, since this affects or is affected by bond formation.

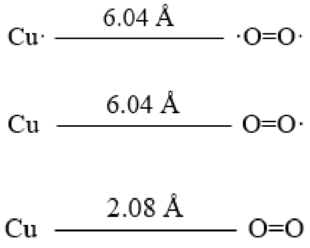

i) Multiplicity 4, O=O bond scan

ii) Multiplicity 2, O=O bond scan

iii) Cleavage of O=O bond (dependent on protonation), and

iv) Reverse scan of O=O bond

Scans i), ii), and iii) are bond scans towards the Cu(II)/C(I), while iv) is a scan away from the Cu(II). The scan coordinate parameter (i), decremented from 6.04 to 1.64 Å in steps of -0.1, (ii) the same approach but with multiplicity 2, and the final bond distance was 1.74 Å, (iii) decremented 2.08 to 0.88 Å in step of 0.05 and finally (iv) incremented 2.08 to 3.13 Å in steps of 0.05.

5.4 Results and Discussions

The ONIOM method combines different levels of theory into one calculation, this method has achieved success in describing large systems. The geometry optimization approach takes advantage of the partitioning of these calculations by treating one region at QM level of theory and the bulk remaining system is treated at MM (Vreven *et al*., 2003).

Table 15: ONIOM energy and RMS optimization results for the five Cu localized residues

Cu bound residue	**ONIOM total energy (Kcal/mol)**	**RMS gradient norm (Kcal/mol)**
His 14	1161.75	0.007
Glu 22	-765.68	0.014
Met 35	1127.34	0.021
Ala 42	-617.15	0.015
Asp 23	624.27	0.116

Table 15 provides the ONIOM total energies for all systems in kcal/mol. Note that the ONIOM values are not comparable to each other although there are systems with exactly the same stoichiometry. This is due to different atoms being at different levels (between systems) within the ONIOM calculation.

In Figure 30, the exploration is of an oxygen coming slowly closer into contact with the Cu, displacing a water molecule in the process. The multiplicity for this system is 4. The scan starts at 1.830 Ha the energy very quickly decreases after only three steps as Cu(II)-O_2 distance decreases reaching 1.825 Ha at scan step 3 at a distance of 5.84 Å. As the distance between Cu(II) and O_2 decreases below 3.4 Å the energy increases to a total of 1.87 Ha. After this point the energy decreases dramatically to 1.807 Ha, the lowest energy obtained for an optimal Cu(II)-O_2 distance.

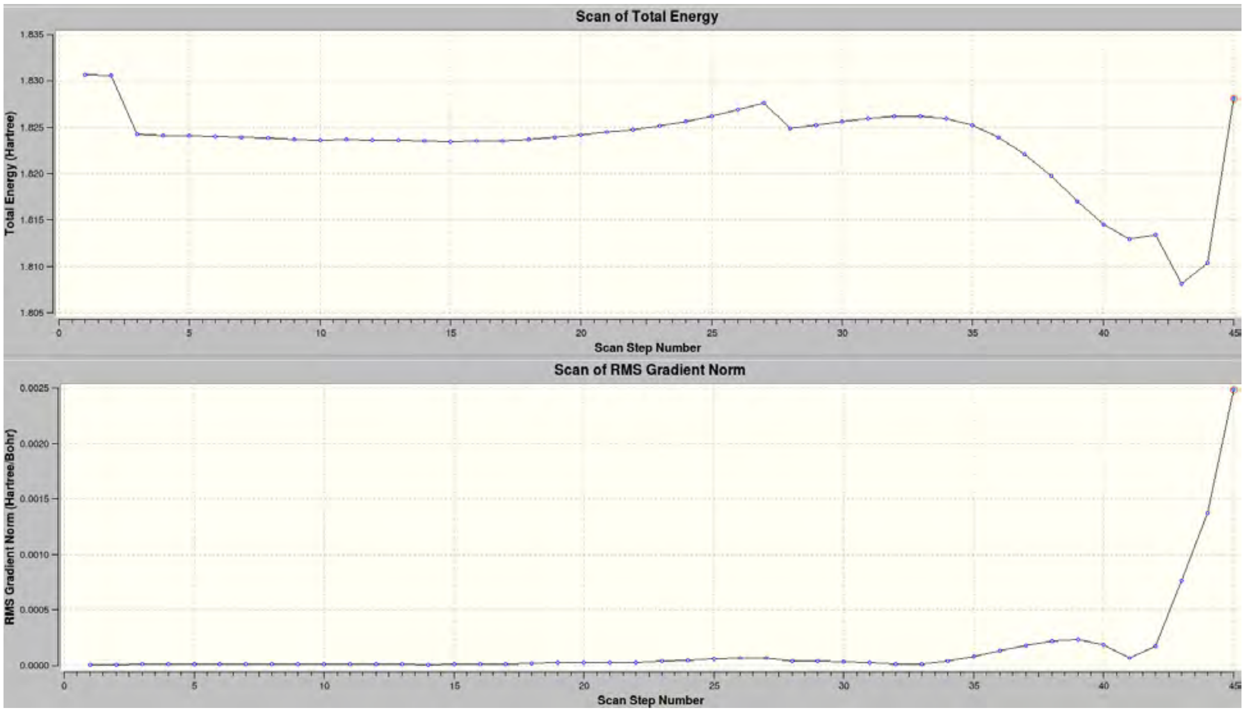

Figure 30: PES scan of O_2 towards Cu(II) coordinated to 2 His14 from adjacent chains and four water molecules.

It is interesting to note that when this scan is repeated at different multiplicity, the interplay between multiplicities becomes apparent. In this scan with multiplicity 2 (Figure 31) the energy starts at 1.830 Ha as before, but remains higher compared to Figure 30 suggesting that when the oxygen is far from the copper, having three unpaired electrons is more favorable energetically. However, the energy drops significantly at scan step 26 when the distance between Cu(II) and O_2 drops below 3.54 Å. This suggests that from this point, it is more favorable to pair two of the electrons in bond formation, leaving a single unpaired electron. The increase in energy after scan step 28 is due to O_2 displacing a H_2O molecule. The Cu(II)-O_2 dative bond reaches its most favorable value at scan step 43 corresponding to 1.770 Ha. The Cu(II)-O_2 dative bond is much more favorable when the electrons are permitted to pair.

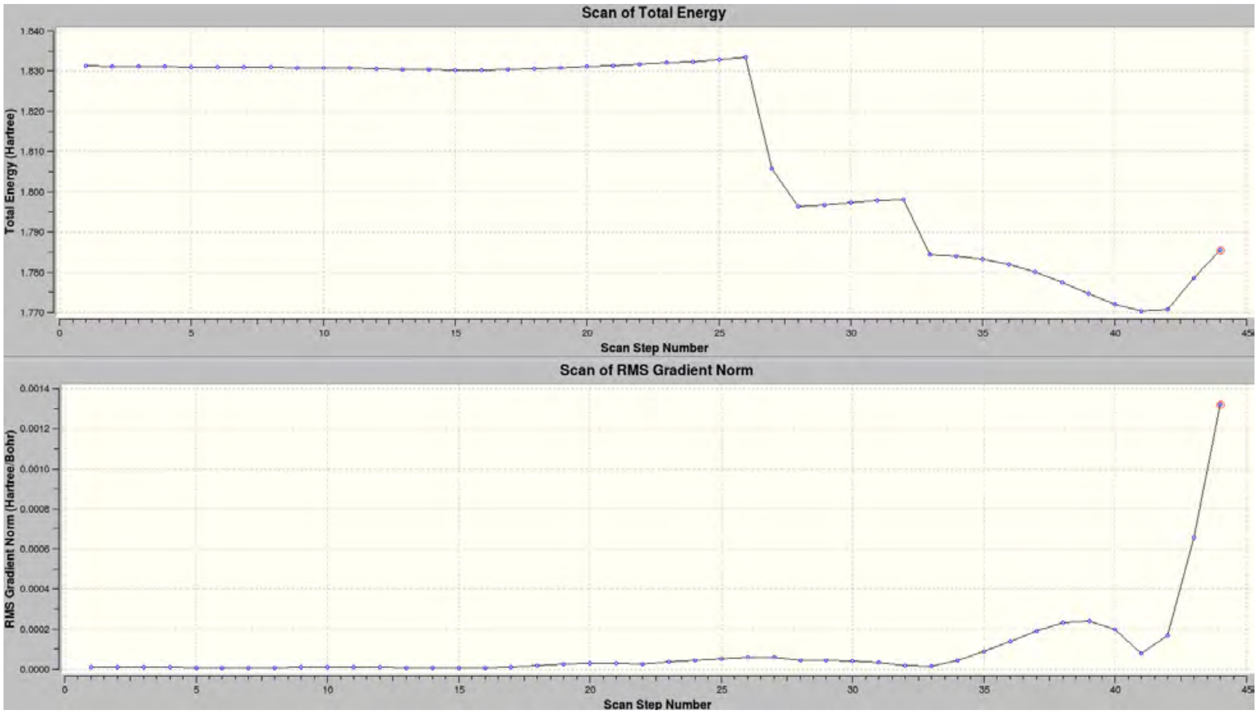

Figure 31: PES scan of O_2 towards Cu(II) coordinated to 2 His14 from adjacent chains and four water molecules.

The scan for O=O bond cleavage, the cleavage of O_2 is an energy expensive process (Figure 32). We do not expect this bond to break directly without protonation, but this provides a basic potential energy surface with which to explore this cleavage where protonation of the O=O is present, and where the oxidation state of the Cu is different.

In terms of the Born-Oppenheimer molecular dynamics, at the B3LYP level, although the calculations are successful, only 11fs of dynamics was possible due to the high level of calculation. Future work will reduce the computational load on the QM portion of the calculation, so that extended dynamics may be performed on the system. Figure 33 shows the interchange betwee kinetic and potential energy during the course of dynamics.

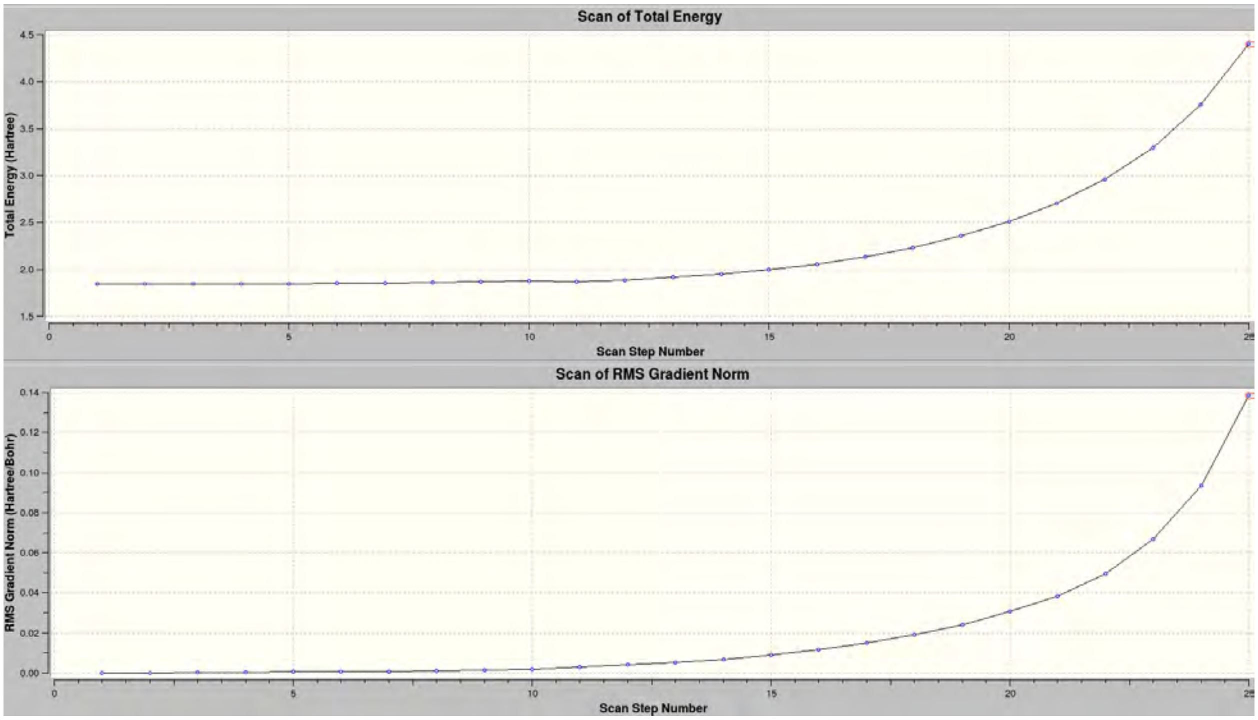

Figure 32: PES scan of O_2 bond breaking towards Cu(II) coordinated to 2 His14 from adjacent chains and four water molecules.

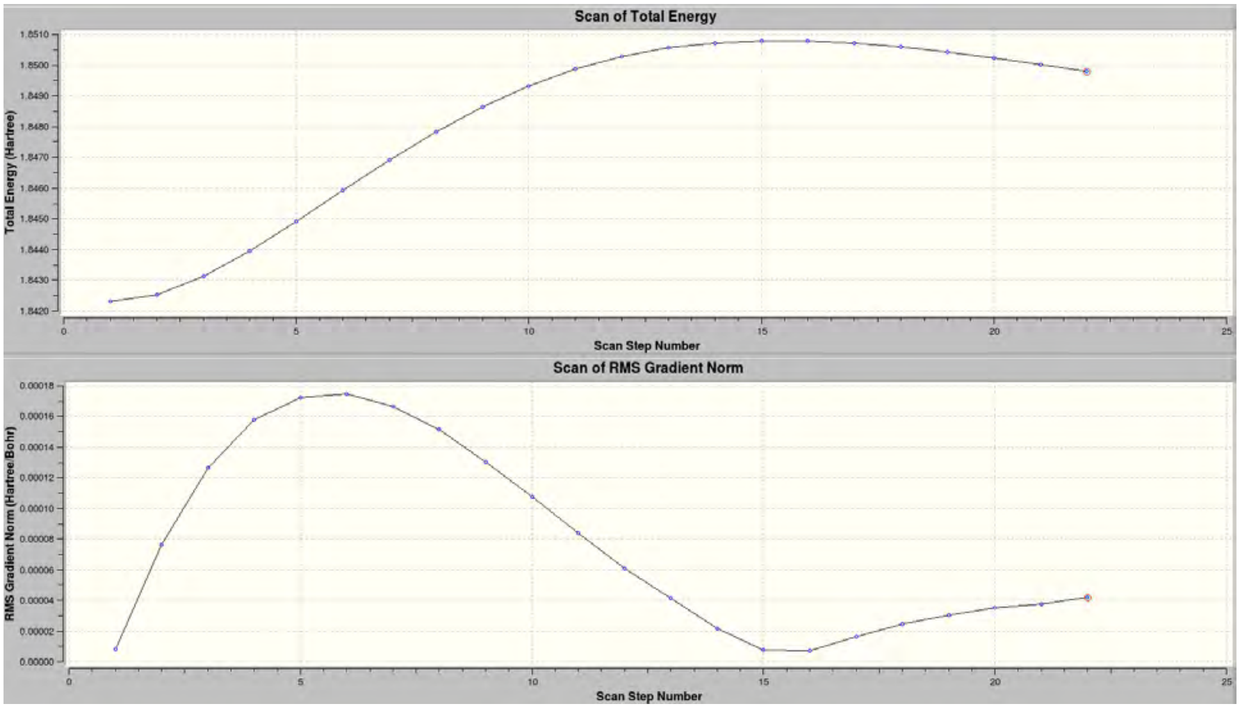

Figure 33: PES scan of O_2 away from Cu(II) coordinated to 2 His14 from adjacent chains and four water molecules.

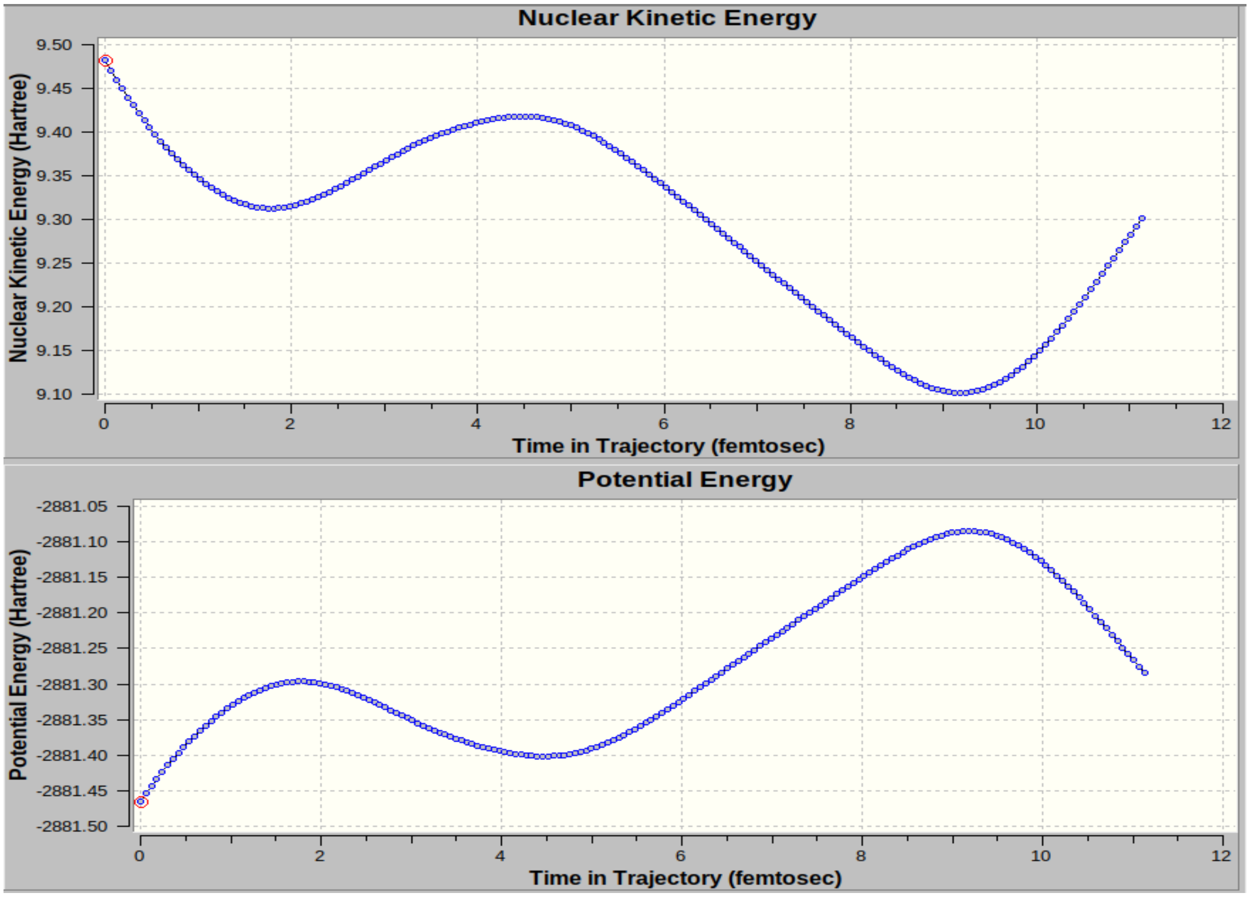

Figure 34: BOMD Cu simulations were performed to 2 Glu22 residues.

In this section the results are preliminary due to time constraints; and future work will explore the generation of all reactive oxygen species and the identification of transition states and reaction pathways detailing their mechanisms of formation. Where this is done for copper at different binding sites, the relative danger of formation of ROS can then be evaluated.

Further, the intention with molecular dynamics is to take the system into the CP2K software to perform adaptive partitioning molecular dynamics to explore exchange processes at the copper center in the Aβ-Cu complex.

Between these to foci, we hope to gain a more complete understanding of metal binding to the fibril, and the consequences of this binding in terms of the reactivity of the complex.

Conclusion

Three $A\beta_{42}$ aggregate structures were used as targets for a targeted docking approach with wgx-50 and seven hundred and twenty-eight SANCDB compounds, leading to fifteen top hits, five from each aggregate structure. The top hits were analyzed in comparison to the known Aβ destabilizer wgx-50, and also based on their structural and physicochemical properties. Destabilizing properties of the top hits to the 2BEG were investigated further through molecular dynamics techniques. The evaluation of the binding of the terminal chain to the fibril in terms of binding energy quantification and destabilization of the ligands involved a combination of pulling and umbrella simulations. The pulling simulations confirmed that the presence of wgx-50 and some of the SANCDB compounds destabilized the terminal chain such that a lower force was required for its removal. Free energy calculations showed SANC00247 and SANC00248 lowered the energy requirements to tear the terminal chain off the fibril, almost to the same extent as wgx-50 and are therefore potential drug candidates for AD.

Three models of an infinite Aβ fibril have been set up using periodic boundary conditions, and are equilibrated in aqueous solutions of ions. These models have been used in molecular dynamics simulations in the presence of metal ions of interest, and this has revealed localization of the metal to residues in some cases, although longer simulations may allow for closer approaches of the metal. Several models of the Aβ-Cu complex have been set up, and potential energy surface scans at the ONIOM (mixed QM and MM level have revealed the energy barrier required for the displacement of water by O_2. Calculations at different multiplicities have quantified the point at which electrons are expected to pair during the approach of O_2 to the copper center of Aβ-Cu.

In a single case BOMD has been performed on an Aβ-Cu complex, but this is a prelude to intended future study of adaptive partitioning molecular dynamics of this system, to explore exchange at the metal center.

Supplementary information

The link below contains supplementary data:

http://tiny.cc/2019_onke_supp

References

1. Alder BJ, Wainwright TE. Studies in molecular dynamics. I. General method. The Journal of Chemical Physics. 1959 Aug;31(2):459-66.
2. Alies, B., Conte-Daban, A., Sayen, S., Collin, F., Kieffer, I., Guillon, E., Faller, P. and Hureau, C., 2016. Zinc (II) binding site to the amyloid-β peptide: insights from spectroscopic studies with a wide series of modified peptides. *Inorganic chemistry*, *55*(20), pp.10499-10509.
3. Allen, M.P., 2004. Introduction to molecular dynamics simulation. Computational soft matter: from synthetic polymers to proteins, 23, pp.1-28.
4. Allen, W.J., Balius, T.E., Mukherjee, S., Brozell, S.R., Moustakas, D.T., Lang, P.T., Case, D.A., Kuntz, I.D. and Rizzo, R.C., 2015. DOCK 6: Impact of new features and current docking performance. Journal of computational chemistry, 36(15), pp.1132-1156.
5. Allgaier, M. and Allgaier, C., 2014. An update on drug treatment options of Alzheimer's disease. *Front Biosci (Landmark Ed)*, *19*, pp.1345-1354.
6. Allsop, D. and Mayes, J., 2014. Amyloid β-peptide and Alzheimer's disease. *Essays in biochemistry*, *56*, pp.99-110.
7. American Psychiatric Association (APA) (1994). Diagnostic and statistical manual of mental disorders (4th Ed.) (DSM-IV), Washington DC: American Psychiatric Association.
8. Andreini, C., Banci, L., Bertini, I. and Rosato, A., 2006. Counting the zinc-proteins encoded in the human genome. Journal of proteome research, 5(1), pp.196-201.
9. Andreini, C., Cavallaro, G. and Lorenzini, S., 2012. FindGeo: a tool for determining metal coordination geometry. Bioinformatics, 28(12), pp.1658-1660.
10. Atri, A., Molinuevo, J.L., Lemming, O., Wirth, Y., Pulte, I. and Wilkinson, D., 2013. Memantine in patients with Alzheimer's disease receiving donepezil: new analyses of efficacy and safety for combination therapy. *Alzheimer's research & therapy*, *5*(1), p.6.
11. Atrián-Blasco, E., Gonzalez, P., Santoro, A., Alies, B., Faller, P. and Hureau, C., 2018. Cu and Zn coordination to amyloid peptides: From fascinating chemistry to debated pathological relevance. Coordination chemistry reviews, 371, pp.38-55.
12. Atwood, C.S., Scarpa, R.C., Huang, X., Moir, R.D., Jones, W.D., Fairlie, D.P., Tanzi, R.E. and Bush, A.I., 2000. Characterization of Copper Interactions with Alzheimer Amyloid β Peptides: Identification of an Attomolar-Affinity Copper Binding Site on Amyloid β1-42. Journal of neurochemistry, 75(3), pp.1219-1233.
13. Azam, F., Alabdullah, N.H., Ehmedat, H.M., Abulifa, A.R., Taban, I. and Upadhyayula, S., 2018. NSAIDs as potential treatment option for preventing amyloid β toxicity in Alzheimer's disease: an investigation by docking, molecular dynamics, and DFT studies. *Journal of Biomolecular Structure and Dynamics*, *36*(8), pp.2099-2117.
14. Balaji, G.L., Rajesh, K., Priya, R., Iniyavan, P., Siva, R. and Vijayakumar, V., 2013. Ultrasound-promoted synthesis, biological evaluation and molecular docking of novel 7-(2-chloroquinolin-4-yloxy)-4-methyl-2H-chromen-2-one derivatives. Medicinal Chemistry Research, 22(7), pp.3185-3192.
15. Barnard, N.D., Bush, A.I., Ceccarelli, A., Cooper, J., de Jager, C.A., Erickson, K.I., Fraser, G., Kesler, S., Levin, S.M., Lucey, B. and Morris, M.C., 2014. Dietary and lifestyle guidelines for the prevention of Alzheimer's disease. *Neurobiology of aging*, *35*, pp.S74-S78.
16. Bateman, R.J., Xiong, C., Benzinger, T.L., Fagan, A.M., Goate, A., Fox, N.C., Marcus, D.S., Cairns, N.J., Xie, X., Blazey, T.M. and Holtzman, D.M., 2012. Clinical and biomarker changes

in dominantly inherited Alzheimer's disease. *New England Journal of Medicine*, *367*(9), pp.795-804.

17. Baumketner, A., Bernstein, S.L., Wyttenbach, T., Bitan, G., Teplow, D.B., Bowers, M.T. and Shea, J.E., 2006. Amyloid β-protein monomer structure: A computational and experimental study. Protein Science, 15(3), pp.420-428.
18. Becker, O.M. and Karplus, M., 2006. Guide to biomolecular simulations (Vol. 4). Springer Science & Business Media.
19. Ben-Arie, O., Swartz, L., Teggin, A.F. and Elk, R., 1983. The coloured elderly in Cape Town--a psychosocial, psychiatric and medical community survey. Part II. Prevalence of psychiatric disorders. *South African medical journal= Suid-Afrikaanse tydskrif vir geneeskunde*, *64*(27), pp.1056-1061.
20. Benet, L.Z., Hosey, C.M., Ursu, O. and Oprea, T.I., 2016. BDDCS, the rule of 5 and drugability. Advanced drug delivery reviews, 101, pp.89-98.
21. Berger, R., 2004. Computational Chemistry. Introduction to the Theory and Applications of Molecular and Quantum Mechanics. Von Errol G. Lewars. Angewandte Chemie, 116(38), pp.5087-5089.
22. Bero, A.W., Yan, P., Roh, J.H., Cirrito, J.R., Stewart, F.R., Raichle, M.E., Lee, J.M. and Holtzman, D.M., 2011. Neuronal activity regulates the regional vulnerability to amyloid-β deposition. *Nature neuroscience*, *14*(6), p.750.
23. Berthold, M.R., Cebron, N., Dill, F., Di Fatta, G., Gabriel, T.R., Georg, F., Meinl, T., Ohl, P., Sieb, C. and Wiswedel, B., 2009. Technical Report Knime: The Konstanz Information Miner.
24. Bi, M., Ittner, A., Ke, Y.D., Götz, J. and Ittner, L.M., 2011. Tau-targeted immunization impedes progression of neurofibrillary histopathology in aged P301L tau transgenic mice. *PloS one*, *6*(12), p.e26860.
25. Blonz, E.R., 2017. Alzheimer's disease as the product of a progressive energy deficiency syndrome in the central nervous system: The neuroenergetic hypothesis. *Journal of Alzheimer's Disease*, *60*(4), pp.1223-1229.
26. Bollag, D.M., McQueney, P.A., Zhu, J., Hensens, O., Koupal, L., Liesch, J., Goetz, M., Lazarides, E. and Woods, C.M., 1995. Epothilones, a new class of microtubule-stabilizing agents with a taxol-like mechanism of action. *Cancer research*, *55*(11), pp.2325-2333.
27. Braak, H. and Del Tredici, K., 2011. Alzheimer's pathogenesis: is there neuron-to-neuron propagation? *Acta neuropathologica*, *121*(5), pp.589-595.
28. Braymer, J.J., Choi, J.S., DeToma, A.S., Wang, C., Nam, K., Kampf, J.W., Ramamoorthy, A. and Lim, M.H., 2011. Development of bifunctional stilbene derivatives for targeting and modulating metal-amyloid-β species. Inorganic chemistry, 50(21), pp.10724-10734.
29. Briggs, R., Kennelly, S.P. and O'Neill, D., 2016. Drug treatments in Alzheimer's disease. *Clinical medicine*, *16*(3), pp.247-253.
30. Brookmeyer, R., Gray, S. and Kawas, C., 1998. Projections of Alzheimer's disease in the United States and the public health impact of delaying disease onset. *American journal of public health*, *88*(9), pp.1337-1342.
31. Brookmeyer, R., Johnson, E., Ziegler-Graham, K. and Arrighi, H.M., 2007. Forecasting the global burden of Alzheimer's disease. *Alzheimer's & dementia*, *3*(3), pp.186-191.
32. Brooks, B.R., Brooks III, C.L., Mackerell Jr, A.D., Nilsson, L., Petrella, R.J., Roux, B., Won, Y., Archontis, G., Bartels, C., Boresch, S. and Caflisch, A., 2009. CHARMM: the biomolecular simulation program. Journal of computational chemistry, 30(10), pp.1545-1614.
33. Brunden, K.R., Zhang, B., Carroll, J., Yao, Y., Potuzak, J.S., Hogan, A.M.L., Iba, M., James, M.J., Xie, S.X., Ballatore, C. and Smith, A.B., 2010. Epothilone D improves microtubule density,

axonal integrity, and cognition in a transgenic mouse model of tauopathy. *Journal of Neuroscience*, *30*(41), pp.13861-13866.

34. Buisson, B. and Bertrand, D., 1998. Open-channel blockers at the human α4β2 neuronal nicotinic acetylcholine receptor. *Molecular pharmacology*, *53*(3), pp.555-563.
35. Bush, A.I., Pettingell, W.H., Multhaup, G., d Paradis, M., Vonsattel, J.P., Gusella, J.F., Beyreuther, K., Masters, C.L. and Tanzi, R.E., 1994. Rapid induction of Alzheimer A beta amyloid formation by zinc. *Science*, *265*(5177), pp.1464-1467.
36. Cao, L. and Ryde, U., 2018. On the difference between additive and subtractive QM/MM calculations. Frontiers in chemistry, 6, p.89.
37. Carlisle T, 2018, Molecular simulations of potential agents and targets of Alzheimer's disease, MSc, Rhodes university, Grahamstown
38. Cassagnes, L.E., Hervé, V., Nepveu, F., Hureau, C., Faller, P. and Collin, F., 2013. The Catalytically Active Copper-Amyloid-Beta State: Coordination Site Responsible for Reactive Oxygen Species Production. Angewandte Chemie International Edition, 52(42), pp.11110-11113.
39. Castro, D.M., Dillon, C., Machnicki, G. and Allegri, R.F., 2010. The economic cost of Alzheimer's disease: Family or public-health burden?. *Dementia & neuropsychologia*, *4*(4), pp.262-267.
40. Cheng, T., Li, Q., Zhou, Z., Wang, Y. and Bryant, S.H., 2012. Structure-based virtual screening for drug discovery: a problem-centric review. The AAPS journal, 14(1), pp.133-141.
41. Chételat, G., La Joie, R., Villain, N., Perrotin, A., de La Sayette, V., Eustache, F. and Vandenberghe, R., 2013. Amyloid imaging in cognitively normal individuals, at-risk populations and preclinical Alzheimer's disease. *NeuroImage: Clinical*, *2*, pp.356-365.
42. Choi, Y., Lee, K., Ryu, J., Kim, H.G., Jeong, A.Y., Woo, R.S., Lee, J.H., Hyun, J.W., Hahn, S., Kim, J.H. and Kim, H.S., 2014. Neuritin attenuates cognitive function impairments in tg2576 mouse model of Alzheimer's disease. *PloS one*, *9*(8), p.e104121.
43. Choo, X.Y. and Grubman, A., 2017. Treatment and Measurement of Metals in Brain Cell Cultures. In Metals in the Brain (pp. 259-268). Humana Press, New York, NY.
44. Chow, V.W., Mattson, M.P., Wong, P.C. and Gleichmann, M., 2010. An overview of APP processing enzymes and products. *Neuromolecular medicine*, *12*(1), pp.1-12.
45. Congdon, E.E. and Sigurdsson, E.M., 2018. Tau-targeting therapies for Alzheimer disease. *Nature Reviews Neurology*, *14*(7), p.399.
46. Corbeil, C.R., Williams, C.I. and Labute, P., 2012. Variability in docking success rates due to dataset preparation. Journal of computer-aided molecular design, 26(6), pp.775-786.
47. Culka, M., Gisdon, F.J. and Ullmann, G.M., 2017. Computational Biochemistry—Enzyme Mechanisms Explored. In Advances in protein chemistry and structural biology (Vol. 109, pp. 77-112). Academic Press.
48. Cummings, J.L., Morstorf, T. and Zhong, K., 2014. Alzheimer's disease drug-development pipeline: few candidates, frequent failures. *Alzheimer's research & therapy*, *6*(4), p.37.
49. Curtain, C.C., Ali, F., Volitakis, I., Cherny, R.A., Norton, R.S., Beyreuther, K., Barrow, C.J., Masters, C.L., Bush, A.I. and Barnham, K.J., 2001. Alzheimer's disease amyloid-β binds copper and zinc to generate an allosterically ordered membrane-penetrating structure containing superoxide dismutase-like subunits. *Journal of Biological Chemistry*, *276*(23), pp.20466-20473.
50. Curtain, C.C., Ali, F., Volitakis, I., Cherny, R.A., Norton, R.S., Beyreuther, K., Barrow, C.J., Masters, C.L., Bush, A.I. and Barnham, K.J., 2001. Alzheimer's disease amyloid-β binds copper and zinc to generate an allosterically ordered membrane-penetrating structure containing superoxide dismutase-like subunits. Journal of Biological Chemistry, 276(23), pp.20466-20473.

51. da Silva, A.W.S. and Vranken, W.F., 2012. ACPYPE-Antechamber python parser interface. *BMC research notes*, *5*(1), p.367.
52. Dai, X., Sun, Y., Gao, Z. and Jiang, Z., 2010. Copper enhances amyloid-β peptide neurotoxicity and non β-aggregation: a series of experiments conducted upon copper-bound and copper-free amyloid-β peptide. Journal of molecular neuroscience, 41(1), pp.66-73.
53. Das, P., Murphy, M.P., Younkin, L.H., Younkin, S.G. and Golde, T.E., 2001. Reduced effectiveness of Aβ1-42 immunization in APP transgenic mice with significant amyloid deposition. *Neurobiology of aging*, *22*(5), pp.721-727.
54. Dawkins, E. and Small, D.H., 2014. Insights into the physiological function of the β-amyloid precursor protein: beyond Alzheimer's disease. *Journal of neurochemistry*, *129*(5), pp.756-769.
55. de Jager, C.A., Msemburi, W., Pepper, K. and Combrinck, M.I., 2017. Dementia prevalence in a rural region of South Africa: a cross-sectional community study. *Journal of Alzheimer's Disease*, *60*(3), pp.1087-1096.
56. Deane, R., Wu, Z., Sagare, A., Davis, J., Du Yan, S., Hamm, K., Xu, F., Parisi, M., LaRue, B., Hu, H.W. and Spijkers, P., 2004. LRP/amyloid β-peptide interaction mediates differential brain efflux of Aβ isoforms. *Neuron*, *43*(3), pp.333-344.
57. Deardorff, W.J. and Grossberg, G.T., 2016. A fixed-dose combination of memantine extended-release and donepezil in the treatment of moderate-to-severe Alzheimer's disease. *Drug design, development and therapy*, *10*, p.3267.
58. Debroise, T., Shakhnovich, E.I. and Chéron, N., 2017. A hybrid knowledge-based and empirical scoring function for protein–ligand interaction: SMoG2016. *Journal of chemical information and modeling*, *57*(3), pp.584-593
59. Doak, B.C., Over, B., Giordanetto, F. and Kihlberg, J., 2014. Oral druggable space beyond the rule of 5: insights from drugs and clinical candidates. Chemistry & biology, 21(9), pp.1115-1142.
60. Dong, H. and Chen, L., 2003. B7-H1 pathway and its role in the evasion of tumor immunity. *Journal of molecular medicine*, *81*(5), pp.281-287.
61. Duan, Y., Wu, C., Chowdhury, S., Lee, M.C., Xiong, G., Zhang, W., Yang, R., Cieplak, P., Luo, R., Lee, T. and Caldwell, J., 2003. A point-charge force field for molecular mechanics simulations of proteins based on condensed-phase quantum mechanical calculations. Journal of computational chemistry, 24(16), pp.1999-2012.
62. Dumont, M. and Beal, M.F., 2011. Neuroprotective strategies involving ROS in Alzheimer disease. *Free radical biology and medicine*, *51*(5), pp.1014-1026.
63. Edgar, R.C., 2004. MUSCLE: multiple sequence alignment with high accuracy and high throughput. Nucleic acids research, 32(5), pp.1792-1797.
64. Eskildsen, S.F., Coupé, P., García-Lorenzo, D., Fonov, V., Pruessner, J.C., Collins, D.L. and Alzheimer's Disease Neuroimaging Initiative, 2013. Prediction of Alzheimer's disease in subjects with mild cognitive impairment from the ADNI cohort using patterns of cortical thinning. *Neuroimage*, *65*, pp.511-521.
65. Faller, P. and Hureau, C., 2009. Bioinorganic chemistry of copper and zinc ions coordinated to amyloid-β peptide. *Dalton Transactions*, (7), pp.1080-1094.
66. Faller, P. and Hureau, C., 2009. Bioinorganic chemistry of copper and zinc ions coordinated to amyloid-β peptide. Dalton Transactions, (7), pp.1080-1094.
67. Faller, P., Hureau, C. and La Penna, G., 2014. Metal ions and intrinsically disordered proteins and peptides: from Cu/Zn amyloid-β to general principles. Accounts of chemical research, 47(8), pp.2252-2259.

68. Fan, Z., Aman, Y., Ahmed, I., Chetelat, G., Landeau, B., Chaudhuri, K.R., Brooks, D.J. and Edison, P., 2015. Influence of microglial activation on neuronal function in Alzheimer's and Parkinson's disease dementia. *Alzheimer's & Dementia*, *11*(6), pp.608-621.
69. Feng, T., Niu, M., Ji, C., Gao, Y., Wen, J., Bu, G., Xu, H. and Zhang, Y.W., 2016. SNX15 regulates cell surface recycling of APP and Aβ generation. *Molecular neurobiology*, *53*(6), pp.3690-3701.
70. Ferri, C.P., Prince, M., Brayne, C., Brodaty, H., Fratiglioni, L., Ganguli, M., Hall, K., Hasegawa, K., Hendrie, H., Huang, Y. and Jorm, A., 2005. Global prevalence of dementia: a Delphi consensus study. The lancet, 366(9503), pp.2112-2117.
71. Folch, J., Busquets, O., Ettcheto, M., Sanchez-Lopez, E., Castro-Torres, R.D., Verdaguer, E., Garcia, M.L., Olloquequi, J., Casadesus, G., Beas-Zarate, C. and Pelegri, C., 2018. Memantine for the treatment of dementia: a review on its current and future applications. *Journal of Alzheimer's Disease*, *62*(3), pp.1223-1240.
72. Foster, N.L., Chase, T.N., Fedio, P., Patronas, N.J., Brooks, R.A. and Di Chiro, G., 1983. Alzheimer's disease: focal cortical changes shown by positron emission tomography. *Neurology*, *33*(8), pp.961-961.
73. Gabbita, S.P., Aksenov, M.Y., Lovell, M.A. and Markesbery, W.R., 1999. Decrease in peptide methionine sulfoxide reductase in Alzheimer's disease brain. *Journal of neurochemistry*, *73*(4), pp.1660-1666.
74. Gao, G., 1998. Large scale molecular simulations with application to polymers and nano-scale materials. California Institute of Technology.
75. Gasparini L, Ongini E, Wenk G. Non-steroidal anti-inflammatory drugs (NSAIDs) in Alzheimer's disease: old and new mechanisms of action. Journal of neurochemistry. 2004 Nov;91(3):521-36.
76. Gaugler, J., James, B., Johnson, T., Marin, A. and Weuve, J., 2019. 2019 Alzheimer's disease facts and figures. *Alzheimers & Dementia*, *15*(3), pp.321-387.
77. George-Carey, R., Adeloye, D., Chan, K.Y., Paul, A., Kolčić, I., Campbell, H. and Rudan, I., 2012. An estimate of the prevalence of dementia in Africa: a systematic analysis. *Journal of global health*, *2*(2).
78. George-Carey, R., Adeloye, D., Chan, K.Y., Paul, A., Kolčić, I., Campbell, H. and Rudan, I., 2012. An estimate of the prevalence of dementia in Africa: a systematic analysis. *Journal of global health*, *2*(2).
79. Gilgun-Sherki, Y., Melamed, E. and Offen, D., 2006. Anti-inflammatory drugs in the treatment of neurodegenerative diseases: current state. *Current pharmaceutical design*, *12*(27), pp.3509-3519.
80. Gilson MK, Given JA, Head MS. 1997. A new class of models for computing receptor-ligand binding affinities. Chem Biol 4~2!:87–92.
81. Gironi, M., Borgiani, B., Farina, E., Mariani, E., Cursano, C., Alberoni, M., Nemni, R., Comi, G., Buscema, M., Furlan, R. and Grossi, E., 2015. A global immune deficit in Alzheimer's disease and mild cognitive impairment disclosed by a novel data mining process. *Journal of Alzheimer's Disease*, *43*(4), pp.1199-1213.
82. Gleiter, R., 1987. Pi-sigma interactions: Experimental evidence and its consequences for the chemical reactivity of organic compounds. Pure and Applied Chemistry, 59(12), pp.1585-1594.
83. González, M.A., 2011. Force fields and molecular dynamics simulations. École thématique de la Société Française de la Neutronique, 12, pp.169-200.
84. Goodsell, D.S., Morris, G.M. and Olson, A.J., 1996. Automated docking of flexible ligands: applications of AutoDock. Journal of Molecular Recognition, 9(1), pp.1-5.

85. Gu, Z., Liu, W. and Yan, Z., 2009. β-Amyloid impairs AMPA receptor trafficking and function by reducing Ca2+/calmodulin-dependent protein kinase II synaptic distribution. *Journal of Biological Chemistry*, *284*(16), pp.10639-10649.

86. H Ferreira-Vieira, T., M Guimaraes, I., R Silva, F. and M Ribeiro, F., 2016. Alzheimer's disease: targeting the cholinergic system. *Current neuropharmacology*, *14*(1), pp.101-115.

87. Haass, C. and Selkoe, D.J., 2007. Soluble protein oligomers in neurodegeneration: lessons from the Alzheimer's amyloid β-peptide. *Nature reviews Molecular cell biology*, *8*(2), p.101.

88. Halperin, I., Wolfson, H. and Nussinov, R., 2004. Protein-protein interactions: coupling of structurally conserved residues and of hot spots across interfaces. Implications for docking. Structure, 12(6), pp.1027-1038.

89. Hamaguchi, T., Ono, K. and Yamada, M., 2010. Curcumin and Alzheimer's disease. *CNS neuroscience & therapeutics*, *16*(5), pp.285-297.

90. Hamdane, M., Sambo, A.V., Delobel, P., Bégard, S., Violleau, A., Delacourte, A., Bertrand, P., Benavides, J. and Buée, L., 2003. Mitotic-like tau phosphorylation by p25-Cdk5 kinase complex. *Journal of Biological Chemistry*, *278*(36), pp.34026-34034.

91. Hanover, J.L., Huang, Z.J., Tonegawa, S. and Stryker, M.P., 1999. Brain-derived neurotrophic factor overexpression induces precocious critical period in mouse visual cortex. *The Journal of neuroscience: the official journal of the Society for Neuroscience*, *19*(22), p.RC40.

92. Harder, M., Kuhn, B. and Diederich, F., 2013. Cover Picture: Efficient Stacking on Protein Amide Fragments (ChemMedChem 3/2013). *ChemMedChem*, *8*(3), pp.345-345.

93. Hardy, J.A. and Higgins, G.A., 1992. Alzheimer's disease: the amyloid cascade hypothesis. *Science*, *256*(5054), pp.184-186.

94. Harvey, A.L., 2008. Natural products in drug discovery. Drug discovery today, 13(19-20), pp.894-901.

95. Hatherley, R., Brown, D.K., Musyoka, T.M., Penkler, D.L., Faya, N., Lobb, K.A. and Bishop, Ö.T., 2015. SANCDB: a South African natural compound database. Journal of cheminformatics, 7(1), p.29.

96. Hebert, L.E., Weuve, J., Scherr, P.A. and Evans, D.A., 2013. Alzheimer disease in the United States (2010–2050) estimated using the 2010 census. Neurology, 80(19), pp.1778-1783.

97. Holtzman, D.M., Morris, J.C. and Goate, A.M., 2011. Alzheimer's disease: the challenge of the second century. *Science translational medicine*, *3*(77), pp.77sr1-77sr1.

98. Hornak, V., Abel, R., Okur, A., Strockbine, B., Roitberg, A. and Simmerling, C., 2006. Comparison of multiple Amber force fields and development of improved protein backbone parameters. Proteins: Structure, Function, and Bioinformatics, 65(3), pp.712-725.

99. Horowitz, S. and Trievel, R.C., 2012. Carbon-oxygen hydrogen bonding in biological structure and function. Journal of Biological Chemistry, 287(50), pp.41576-41582.

100. Hospital, A., Goñi, J.R., Orozco, M. and Gelpí, J.L., 2015. Molecular dynamics simulations: advances and applications. Advances and applications in bioinformatics and chemistry: AABC, 8, p.37.

101. Hou, S., Gu, R.X. and Wei, D.Q., 2017. Inhibition of β-amyloid channels with a drug candidate wgx-50 revealed by molecular dynamics simulations. *Journal of chemical information and modeling*, *57*(11), pp.2811-2821.

102. Houmani, N., Vialatte, F., Gallego-Jutglà, E., Dreyfus, G., Nguyen-Michel, V.H., Mariani, J. and Kinugawa, K., 2018. Diagnosis of Alzheimer's disease with Electroencephalography in a differential framework. *PloS one*, *13*(3), p.e0193607.

103. Huang, E.P., 1997. Metal ions and synaptic transmission: think zinc. Proceedings of the National Academy of Sciences, 94(25), pp.13386-13387.

104. Huang, S.Y., Grinter, S.Z. and Zou, X., 2010. Scoring functions and their evaluation methods for protein–ligand docking: recent advances and future directions. Physical Chemistry Chemical Physics, 12(40), pp.12899-12908.

105. Huang, X., Atwood, C.S., Hartshorn, M.A., Multhaup, G., Goldstein, L.E., Scarpa, R.C., Cuajungco, M.P., Gray, D.N., Lim, J., Moir, R.D. and Tanzi, R.E., 1999. The Aβ peptide of Alzheimer's disease directly produces hydrogen peroxide through metal ion reduction. *Biochemistry*, *38*(24), pp.7609-7616.

106. Hung, Y.H., Bush, A.I. and La Fontaine, S., 2013. Links between copper and cholesterol in Alzheimer's disease. *Frontiers in physiology*, *4*, p.111.

107. Hureau, C., 2012. Coordination of redox active metal ions to the amyloid precursor protein and to amyloid-β peptides involved in Alzheimer disease. Part 1: An overview. *Coordination Chemistry Reviews*, *256*(19-20), pp.2164-2174.

108. Iqbal, K. and Grundke-Iqbal, I., 2008. Alzheimer neurofibrillary degeneration: significance, etiopathogenesis, therapeutics and prevention. *Journal of cellular and molecular medicine*, *12*(1), pp.38-55.

109. Izrailev, S., Sergey, S., Isralewitz, B., Kosztin, D., Lu, H., Molnar, F., Wriggers, W. and Schulten, K., 1998. Steered Molecular Dynamics; Vol. 4 of Lecture Notes in Computational Science and Engineering.

110. Jain, A.N., 2003. Surflex: fully automatic flexible molecular docking using a molecular similarity-based search engine. Journal of medicinal chemistry, 46(4), pp.499-511.

111. Jeong, H.H., Yalamanchili, H.K., Guo, C., Shulman, J.M. and Liu, Z., 2018. An ultra-fast and scalable quantification pipeline for transposable elements from next generation sequencing data. In *PSB* (pp. 168-179).

112. Ji, Y., Shi, Z., Zhang, Y., Liu, S., Liu, S., Yue, W., Liu, M., Huo, Y.R., Wang, J. and Wisniewski, T., 2015. Prevalence of dementia and main subtypes in rural northern China. *Dementia and geriatric cognitive disorders*, *39*(5-6), pp.294-302.

113. Jia, J., Wang, F., Wei, C., Zhou, A., Jia, X., Li, F., Tang, M., Chu, L., Zhou, Y., Zhou, C. and Cui, Y., 2014. The prevalence of dementia in urban and rural areas of China. *Alzheimer's & Dementia*, *10*(1), pp.1-9.

114. Jia, J., Wei, C., Liang, J., Zhou, A., Zuo, X., Song, H., Wu, L., Chen, X., Chen, S., Zhang, J. and Wu, J., 2016. The effects of DL-3-n-butylphthalide in patients with vascular cognitive impairment without dementia caused by subcortical ischemic small vessel disease: A multicentre, randomized, double-blind, placebo-controlled trial. *Alzheimer's & dementia*, *12*(2), pp.89-99.

115. Jones, G., Willett, P., Glen, R.C., Leach, A.R. and Taylor, R., 1997. Development and validation of a genetic algorithm for flexible docking. Journal of molecular biology, 267(3), pp.727-748.

116. Kaminski, G.A., Friesner, R.A., Tirado-Rives, J. and Jorgensen, W.L., 2001. Evaluation and reparametrization of the OPLS-AA force field for proteins via comparison with accurate quantum chemical calculations on peptides. The Journal of Physical Chemistry B, 105(28), pp.6474-6487.

117. Karr, J.W. and Szalai, V.A., 2007. Role of aspartate-1 in Cu (II) binding to the amyloid-β peptide of Alzheimer's disease. Journal of the American Chemical Society, 129(13), pp.3796-3797.

118. Karr, J.W., Kaupp, L.J. and Szalai, V.A., 2004. Amyloid-β binds Cu2+ in a mononuclear metal ion binding site. Journal of the American Chemical Society, 126(41), pp.13534-13538.

119. Kästner, J., 2011. Umbrella sampling. Wiley Interdisciplinary Reviews: Computational Molecular Science, 1(6), pp.932-942.

120. Kepp KP. Alzheimer's disease due to loss of function: A new synthesis of the available data. Progress in neurobiology. 2016 Aug 1;143:36-60.

121. Kepp, K.P., 2012. Bioinorganic chemistry of Alzheimer's disease. Chemical reviews, 112(10), pp.5193-5239.
122. Kepp, K.P., 2017. Alzheimer's disease: How metal ions define β-amyloid function. Coordination Chemistry Reviews, 351, pp.127-159.
123. Kimura, M., 1983. The neutral theory of molecular evolution. Cambridge University Press.
124. Kitchen, D.B., Decornez, H., Furr, J.R. and Bajorath, J., 2004. Docking and scoring in virtual screening for drug discovery: methods and applications. Nature reviews Drug discovery, 3(11), p.935.
125. Kitchen, D.B., Decornez, H., Furr, J.R. and Bajorath, J., 2004. Structure-based virtual screening and lead optimization: methods and applications. *Nature Rev Drug Discov*, *3*, pp.935-949.
126. Kozin, S.A., Zirah, S., Rebuffat, S., Hoa, G.H.B. and Debey, P., 2001. Zinc binding to Alzheimer's Aβ (1–16) peptide results in stable soluble complex. Biochemical and biophysical research communications, 285(4), pp.959-964.
127. Kumar, S., Rosenberg, J.M., Bouzida, D., Swendsen, R.H. and Kollman, P.A., 1992. The weighted histogram analysis method for free‐energy calculations on biomolecules. I. The method. Journal of computational chemistry, 13(8), pp.1011-1021.
128. L Orcellet, M. and O Fernandez, C., 2011. Structures behind the amyloid aggregation of α-synuclein: An NMR based approach. Current Protein and Peptide Science, 12(3), pp.188-205.
129. La Penna, G., Hureau, C., Andreussi, O. and Faller, P., 2013. Identifying, by first-principles simulations, Cu [amyloid-β] species making fenton-type reactions in Alzheimer's disease. The journal of physical chemistry B, 117(51), pp.16455-16467.
130. Lathouwers, L. and Broeckhove, J., 1992. Time-dependent quantum molecular dynamics. Plenum Press.
131. Lemkul, J.A. and Bevan, D.R., 2010. Assessing the stability of Alzheimer's amyloid protofibrils using molecular dynamics. *The Journal of Physical Chemistry B*, *114*(4), pp.1652-1660.
132. Lemkul, J.A. and Bevan, D.R., 2010. Assessing the stability of Alzheimer's amyloid protofibrils using molecular dynamics. The Journal of Physical Chemistry B, 114(4), pp.1652-1660.
133. Li, J., 2014. Theoretical studies on the low-lying electronic states of N2O: From structural aspects to reaction dynamics (Doctoral dissertation).
134. Lindwall, G. and Cole, R.D., 1984. Phosphorylation affects the ability of tau protein to promote microtubule assembly. *Journal of Biological Chemistry*, *259*(8), pp.5301-5305.
135. Lionta, E., Spyrou, G., K Vassilatis, D. and Cournia, Z., 2014. Structure-based virtual screening for drug discovery: principles, applications and recent advances. Current topics in medicinal chemistry, 14(16), pp.1923-1938.
136. Lipinski, C.A., Lombardo, F., Dominy, B.W. and Feeney, P.J., 1997. Experimental and computational approaches to estimate solubility and permeability in drug discovery and development settings. Advanced drug delivery reviews, 23(1-3), pp.3-25.
137. Loewi, O., 1921. Über humorale übertragbarkeit der Herznervenwirkung. *Pflügers Archiv European Journal of Physiology*, *189*(1), pp.239-242.
138. Lührs, T., Ritter, C., Adrian, M., Riek-Loher, D., Bohrmann, B., Döbeli, H., Schubert, D. and Riek, R., 2005. 3D structure of Alzheimer's amyloid-β (1–42) fibrils. Proceedings of the National Academy of Sciences, 102(48), pp.17342-17347.
139. Manning, F.C., 1994. Tacrine therapy for the dementia of Alzheimer's disease. *American family physician*, *50*(4), pp.819-826.
140. Martorana, A. and Koch, G., 2014. Is dopamine involved in Alzheimer's disease? *Frontiers in aging neuroscience*, *6*, p.252.

141. Masman, M.F., Eisel, U.L., Csizmadia, I.G., Penke, B., Enriz, R.D., Marrink, S.J. and Luiten, P.G., 2009. In silico study of full-length amyloid β 1− 42 tri-and penta-oligomers in solution. The Journal of Physical Chemistry B, 113(34), pp.11710-11719.
142. Mayeux, R. and Stern, Y., 2012. Epidemiology of Alzheimer disease. Cold Spring Harbor perspectives in medicine, 2(8), p.a006239.
143. Mayeux, R. and Stern, Y., 2012. Epidemiology of Alzheimer disease. Cold Spring Harbor perspectives in medicine, 2(8), p.a006239.
144. Maynard, C.J., Bush, A.I., Masters, C.L., Cappai, R. and Li, Q.X., 2005. Metals and amyloid-β in Alzheimer's disease. International journal of experimental pathology, 86(3), pp.147-159.
145. McConkey, B.J., Sobolev, V. and Edelman, M., 2002. The performance of current methods in ligand–protein docking. Current Science, pp.845-856.
146. Meek, P.D., McKeithan, E.K. and Schumock, G.T., 1998. Economic considerations in Alzheimer's disease. *Pharmacotherapy: The Journal of Human Pharmacology and Drug Therapy*, *18*(2P2), pp.68-73.
147. Meliá, C., Ferrer, S., Řezáč, J., Parisel, O., Reinaud, O., Moliner, V. and De la Lande, A., 2013. Investigation of the hydroxylation mechanism of noncoupled copper oxygenases by ab initio molecular dynamics simulations. Chemistry–A European Journal, 19(51), pp.17328-17337.
148. Memczak, S., Jens, M., Elefsinioti, A., Torti, F., Krueger, J., Rybak, A., Maier, L., Mackowiak, S.D., Gregersen, L.H., Munschauer, M. and Loewer, A., 2013. Circular RNAs are a large class of animal RNAs with regulatory potency. *Nature*, *495*(7441), p.333.
149. Meng, X.Y., Zhang, H.X., Mezei, M. and Cui, M., 2011. Molecular docking: a powerful approach for structure-based drug discovery. *Current computer-aided drug design*, *7*(2), pp.146-157.
150. Miao, Y. and McCammon, J.A., 2016. Unconstrained enhanced sampling for free energy calculations of biomolecules: a review. Molecular simulation, 42(13), pp.1046-1055.
151. Mignani, S., Rodrigues, J., Tomas, H., Jalal, R., Singh, P.P., Majoral, J.P. and Vishwakarma, R.A., 2018. Present drug-likeness filters in medicinal chemistry during the hit and lead optimization process: how far can they be simplified?. Drug discovery today, 23(3), pp.605-615.
152. Mills, M. and Andricioaei, I., 2008. An experimentally guided umbrella sampling protocol for biomolecules. The Journal of chemical physics, 129(11), p.114101.
153. Mohandas, E., Rajmohan, V. and Raghunath, B., 2009. Neurobiology of Alzheimer's disease. *Indian journal of psychiatry*, *51*(1), p.55.
154. Monsonego, A., Zota, V., Karni, A., Krieger, J.I., Bar-Or, A., Bitan, G., Budson, A.E., Sperling, R., Selkoe, D.J. and Weiner, H.L., 2003. Increased T cell reactivity to amyloid β protein in older humans and patients with Alzheimer disease. *The Journal of clinical investigation*, *112*(3), pp.415-422.
155. Morris, G.M., Huey, R. and Olson, A.J., 2008. Using autodock for ligand-receptor docking. Current protocols in bioinformatics, 24(1), pp.8-14.
156. Mosconi, L., Brys, M., Glodzik-Sobanska, L., De Santi, S., Rusinek, H. and De Leon, M.J., 2007. Early detection of Alzheimer's disease using neuroimaging. *Experimental gerontology*, *42*(1-2), pp.129-138.
157. Moses, V., Bishop, Ö.T. and Lobb, K.A., 2017. The evaluation and validation of copper (II) force field parameters of the Auxiliary Activity family 9 enzymes. Chemical Physics Letters, 678, pp.91-97.
158. Moses, V., Bishop, Ö.T. and Lobb, K.A., 2017. The evaluation and validation of copper (II) force field parameters of the Auxiliary Activity family 9 enzymes. *Chemical Physics Letters*, *678*, pp.91-97.

159. Mudher, A. and Lovestone, S., 2002. Alzheimer's disease–do tauists and baptists finally shake hands?. *Trends in neurosciences*, *25*(1), pp.22-26.
160. Muegge, I., 2000. A knowledge-based scoring function for protein-ligand interactions: Probing the reference state. *Perspectives in Drug Discovery and Design*, *20*(1), pp.99-114.
161. Muir, J.L., 1997. Acetylcholine, aging, and Alzheimer's disease. *Pharmacology Biochemistry and Behavior*, *56*(4), pp.687-696.
162. Murakami, K., Horikoshi-Sakuraba, Y., Murata, N., Noda, Y., Masuda, Y., Kinoshita, N., Hatsuta, H., Murayama, S., Shirasawa, T., Shimizu, T. and Irie, K., 2010. Monoclonal antibody against the turn of the 42-residue amyloid β-protein at positions 22 and 23. ACS chemical neuroscience, 1(11), pp.747-756.
163. Murray, C.W., Auton, T.R. and Eldridge, M.D., 1998. Empirical scoring functions. II. The testing of an empirical scoring function for the prediction of ligand-receptor binding affinities and the use of Bayesian regression to improve the quality of the model. *Journal of computer-aided molecular design*, *12*(5), pp.503-519.
164. Nagahara, A.H., Merrill, D.A., Coppola, G., Tsukada, S., Schroeder, B.E., Shaked, G.M., Wang, L., Blesch, A., Kim, A., Conner, J.M. and Rockenstein, E., 2009. Neuroprotective effects of brain-derived neurotrophic factor in rodent and primate models of Alzheimer's disease. *Nature medicine*, *15*(3), p.331.
165. National Institute for Health and Clinical Excellence (Great Britain), 2011. *Donepezil, Galantamine, Rivastigmine and Memantne for the Treatment of Alzheimer's Disease: Review of NICE Technology Appraisal Guidance 111*. National Institute for Health and Clinical Excellence.
166. Nativio, R., Donahue, G., Berson, A., Lan, Y., Amlie-Wolf, A., Tuzer, F., Toledo, J.B., Gosai, S.J., Gregory, B.D., Torres, C. and Trojanowski, J.Q., 2018. Dysregulation of the epigenetic landscape of normal aging in Alzheimer’s disease. *Nature neuroscience*, *21*(4), p.497.
167. Navarro, A. and Boveris, A., 2009. Brain mitochondrial dysfunction and oxidative damage in Parkinson’s disease. *Journal of Bioenergetics and Biomembranes*, *41*(6), pp.517-521.
168. Okumura, H. and Itoh, S.G., 2016. Structural and fluctuational difference between two ends of Aβ amyloid fibril: MD simulations predict only one end has open conformations. Scientific reports, 6, p.38422.
169. Ono, K., Yoshiike, Y., Takashima, A., Hasegawa, K., Naiki, H. and Yamada, M., 2003. Potent anti-amyloidogenic and fibril-destabilizing effects of polyphenols in vitro: implications for the prevention and therapeutics of Alzheimer's disease. *Journal of neurochemistry*, *87*(1), pp.172-181.
170. Österberg, F., Morris, G.M., Sanner, M.F., Olson, A.J. and Goodsell, D.S., 2002. Automated docking to multiple target structures: incorporation of protein mobility and structural water heterogeneity in AutoDock. Proteins: Structure, Function, and Bioinformatics, 46(1), pp.34-40.
171. Palm, K., Stenberg, P., Luthman, K. and Artursson, P., 1997. Polar molecular surface properties predict the intestinal absorption of drugs in humans. Pharmaceutical research, 14(5), pp.568-571.
172. Panza, F., Solfrizzi, V., Seripa, D., Imbimbo, B.P., Lozupone, M., Santamato, A., Zecca, C., Barulli, M.R., Bellomo, A., Pilotto, A. and Daniele, A., 2016. Tau-centric targets and drugs in clinical development for the treatment of Alzheimer’s disease. *BioMed research international*, *2016*.
173. Paquet, E. and Viktor, H.L., 2018. Computational Methods for Ab Initio Molecular Dynamics. Advances in Chemistry, 2018.
174. Parhizkar, S., Arzberger, T., Brendel, M., Kleinberger, G., Deussing, M., Focke, C., Nuscher, B., Xiong, M., Ghasemigharagoz, A., Katzmarski, N. and Krasemann, S., 2019. Loss of TREM2 function increases amyloid seeding but reduces plaque-associated ApoE. *Nature neuroscience*, *22*(2), p.191.

175. Pason, L.P. and Sotriffer, C.A., 2016. Empirical Scoring Functions for Affinity Prediction of Protein-ligand Complexes. *Molecular informatics*, *35*(11-12), pp.541-548.
176. Payne, M.C., Teter, M.P., Allan, D.C., Arias, T.A. and Joannopoulos, A.J., 1992. Iterative minimization techniques for ab initio total-energy calculations: molecular dynamics and conjugate gradients. Reviews of modern physics, 64(4), p.1045.
177. Perez Ortiz, J.M. and Swerdlow, R.H., 2019. Mitochondrial dysfunction in Alzheimer's disease: Role in pathogenesis and novel therapeutic opportunities. *British journal of pharmacology*.
178. Prieto-Martínez, F.D., Arciniega, M. and Medina-Franco, J.L., 2019. Molecular docking: current advances and challenges. *TIP Revista Especializada en Ciencias Químico-Biológicas*, *21*(S1), pp.65-87.
179. Priller, C., Bauer, T., Mitteregger, G., Krebs, B., Kretzschmar, H.A. and Herms, J., 2006. Synapse formation and function is modulated by the amyloid precursor protein. Journal of Neuroscience, 26(27), pp.7212-7221.
180. Prince, M., Comas-Herrera, A., Knapp, M., Guerchet, M. and Karagiannidou, M., 2016. World Alzheimer report 2016: improving healthcare for people living with dementia: coverage, quality and costs now and in the future.
181. Prince, M.J., 2015. World Alzheimer Report 2015: the global impact of dementia: an analysis of prevalence, incidence, cost and trends. Alzheimer's Disease International.
182. Querfurth, H.W. and LaFerla, F.M., 2010. Mechanisms of disease. N Engl J Med, 362(4), pp.329-344.
183. Quiroga, R. and Villarreal, M.A., 2016. Vinardo: A scoring function based on autodock vina improves scoring, docking, and virtual screening. PloS one, 11(5), p.e0155183.
184. Quistorff, B., Secher, N.H. and Van Lieshout, J.J., 2008. Lactate fuels the human brain during exercise. *The FASEB Journal*, *22*(10), pp.3443-3449.
185. Ramesh, B.N., Raichurkar, K.P., Shamasundar, N.M., Rao, T.S.S. and Rao, K.S.J., 2011. Aβ (42) induced MRI changes in aged rabbit brain resembles AD brain. Neurochemistry international, 59(5), pp.637-642.
186. Rarey, M., Kramer, B., Lengauer, T. and Klebe, G., 1996. A fast flexible docking method using an incremental construction algorithm. Journal of molecular biology, 261(3), pp.470-489.
187. Ren, J., He, Y., Chen, W., Chen, T., Wang, G., Wang, Z., Xu, Z., Luo, X., Zhu, W., Jiang, H. and Shen, J., 2014. Thermodynamic and structural characterization of halogen bonding in protein–ligand interactions: a case study of PDE5 and its inhibitors. Journal of medicinal chemistry, 57(8), pp.3588-3593.
188. Riverol, M. and López, O., 2011. Biomarkers in Alzheimer's disease. *Frontiers in neurology*, *2*, p.46.
189. Riviere, G.R., Riviere, K.H. and Smith, K.S., 2002. Molecular and immunological evidence of oral Treponema in the human brain and their association with Alzheimer's disease. *Oral microbiology and immunology*, *17*(2), pp.113-118.
190. Rudnitskaya, E.A., Kozlova, T.A., Burnyasheva, A.O., Kolosova, N.G. and Stefanova, N.A., 2019. Alterations of hippocampal neurogenesis during development of Alzheimer's disease-like pathology in OXYS rats. *Experimental gerontology*, *115*, pp.32-45.
191. Salah, T., Belaidi, S., Melkemi, N. and Tchouar, N., 2015. Molecular Geometry, Electronic Properties, MPO Methods and Structure Activity/Property Relationship Studies of 1, 3, 4-Thiadiazole Derivatives by Theoretical Calculations. Reviews in Theoretical Science, 3(4), pp.355-364.

192. Salomone, S., Caraci, F., Leggio, G.M., Fedotova, J. and Drago, F., 2012. New pharmacological strategies for treatment of Alzheimer's disease: focus on disease modifying drugs. *British journal of clinical pharmacology*, *73*(4), pp.504-517.
193. Sarell, C.J., Wilkinson, S.R. and Viles, J.H., 2010. Substoichiometric levels of Cu2+ ions accelerate the kinetics of fiber formation and promote cell toxicity of amyloid-β from Alzheimer disease. Journal of biological chemistry, 285(53), pp.41533-41540.
194. Sarter, M., Givens, B. and Bruno, J.P., 2001. The cognitive neuroscience of sustained attention: where top-down meets bottom-up. *Brain research reviews*, *35*(2), pp.146-160.
195. Schneider, L.S., Mangialasche, F., Andreasen, N., Feldman, H., Giacobini, E., Jones, R., Mantua, V., Mecocci, P., Pani, L., Winblad, B. and Kivipelto, M., 2014. Clinical trials and late-stage drug development for A lzheimer's disease: an appraisal from 1984 to 2014. *Journal of internal medicine*, *275*(3), pp.251-283.
196. Segall, M., 2012. Drug-Like or Likely to be a Drug?. Innov. Pharm. Technol., 43, pp.20-23.
197. Selkoe, D.J., 1991. The molecular pathology of Alzheimer's disease. *Neuron*, *6*(4), pp.487-498.
198. Selkoe, D.J., 1999. Translating cell biology into therapeutic advances in Alzheimer's disease. Nature, 399(6738), p.A23.
199. Seminario, J.M. and Balbuena, P.B. eds., 1999. Molecular dynamics: from classical to quantum methods. Elsevier.
200. Senn, H.M. and Thiel, W., 2009. QM/MM methods for biomolecular systems. Angewandte Chemie International Edition, 48(7), pp.1198-1229.
201. Sethi, A., Joshi, K., Sasikala, K. and Alvala, M., 2019. Molecular Docking in Modern Drug Discovery: Principles and Recent Applications. In *Drug Discovery and Development-New Advances*. IntechOpen.
202. Shankar, G.M., Li, S., Mehta, T.H., Garcia-Munoz, A., Shepardson, N.E., Smith, I., Brett, F.M., Farrell, M.A., Rowan, M.J., Lemere, C.A. and Regan, C.M., 2008. Amyloid-β protein dimers isolated directly from Alzheimer's brains impair synaptic plasticity and memory. *Nature medicine*, *14*(8), p.837.
203. Shibata, M., Yamada, S., Kumar, S.R., Calero, M., Bading, J., Frangione, B., Holtzman, D.M., Miller, C.A., Strickland, D.K., Ghiso, J. and Zlokovic, B.V., 2000. Clearance of Alzheimer's amyloid-β 1-40 peptide from brain by LDL receptor–related protein-1 at the blood-brain barrier. *The Journal of clinical investigation*, *106*(12), pp.1489-1499.
204. Shukla, V., Zheng, Y.L., Mishra, S.K., Amin, N.D., Steiner, J., Grant, P., Kesavapany, S. and Pant, H.C., 2013. A truncated peptide from p35, a Cdk5 activator, prevents Alzheimer's disease phenotypes in model mice. *The FASEB Journal*, *27*(1), pp.174-186.
205. Silva, K.I., Michael, B.C., Geib, S.J. and Saxena, S., 2014. ESEEM analysis of multi-histidine Cu (II)-coordination in model complexes, peptides, and amyloid-β. The Journal of Physical Chemistry B, 118(30), pp.8935-8944.
206. Smith, D.G., Cappai, R. and Barnham, K.J., 2007. The redox chemistry of the Alzheimer's disease amyloid β peptide. Biochimica et Biophysica Acta (BBA)-Biomembranes, 1768(8), pp.1976-1990.
207. Smith, M.A., Drew, K.L., Nunomura, A., Takeda, A., Hirai, K., Zhu, X., Atwood, C.S., Raina, A.K., Rottkamp, C.A., Sayre, L.M. and Friedland, R.P., 2002. Amyloid-β, tau alterations and mitochondrial dysfunction in Alzheimer disease: the chickens or the eggs?. *Neurochemistry international*, *40*(6), pp.527-531.
208. Spyrakis, F. and Cavasotto, C.N., 2015. Open challenges in structure-based virtual screening: Receptor modeling, target flexibility consideration and active site water molecules description. *Archives of biochemistry and biophysics*, *583*, pp.105-119.

209. Svensson, M., Humbel, S., Froese, R.D., Matsubara, T., Sieber, S. and Morokuma, K., 1996. ONIOM: a multilayered integrated MO+ MM method for geometry optimizations and single point energy predictions. A test for Diels− Alder reactions and Pt (P (t-Bu) 3) 2+ H2 oxidative addition. The Journal of Physical Chemistry, 100(50), pp.19357-19363.
210. Talmard, C., Bouzan, A. and Faller, P., 2007. Zinc binding to amyloid-β: isothermal titration calorimetry and Zn competition experiments with Zn sensors. *Biochemistry*, *46*(47), pp.13658-13666.
211. Tarasoff-Conway, J.M., Carare, R.O., Osorio, R.S., Glodzik, L., Butler, T., Fieremans, E., Axel, L., Rusinek, H., Nicholson, C., Zlokovic, B.V. and Frangione, B., 2015. Clearance systems in the brain—implications for Alzheimer disease. *Nature reviews neurology*, *11*(8), p.457.
212. Tariot, P.N. and Aisen, P.S., 2009. Can lithium or valproate untie tangles in Alzheimer's disease?. *The Journal of clinical psychiatry*, *70*(6), pp.919-921.
213. Thies, W. and Bleiler, L., 2011. Alzheimer’s disease facts and figures. Alzheimer’s Dement.
214. Torrie, G.M. and Valleau, J.P., 1977. Nonphysical sampling distributions in Monte Carlo free-energy estimation: Umbrella sampling. Journal of Computational Physics, 23(2), pp.187-199.
215. Trott, O. and Olson, A.J., 2010. AutoDock Vina: improving the speed and accuracy of docking with a new scoring function, efficient optimization, and multithreading. Journal of computational chemistry, 31(2), pp.455-461.
216. van der Kamp, M.W. and Mulholland, A.J., 2013. Combined quantum mechanics/molecular mechanics (QM/MM) methods in computational enzymology. Biochemistry, 52(16), pp.2708-2728.
217. Van der Poel R, Heyns P (2012) Algorithmic case prediction inrelation to local clinician diagnosis in an indigenous SouthAfrican population 27th International Conference ofAlzheimer’s Disease International (ADI). London, England
218. Vanommeslaeghe, K., Hatcher, E., Acharya, C., Kundu, S., Zhong, S., Shim, J., Darian, E., Guvench, O., Lopes, P., Vorobyov, I. and MacKerell Jr, A.D., 2010. CHARMM general force field: A force field for drug‐like molecules compatible with the CHARMM all‐atom additive biological force fields. Journal of computational chemistry, 31(4), pp.671-690.
219. Venkatachalam, C.M., Jiang, X., Oldfield, T. and Waldman, M., 2003. LigandFit: a novel method for the shape-directed rapid docking of ligands to protein active sites. Journal of Molecular Graphics and Modelling, 21(4), pp.289-307.
220. Villemagne, V.L., Burnham, S., Bourgeat, P., Brown, B., Ellis, K.A., Salvado, O., Szoeke, C., Macaulay, S.L., Martins, R., Maruff, P. and Ames, D., 2013. Amyloid β deposition, neurodegeneration, and cognitive decline in sporadic Alzheimer's disease: a prospective cohort study. *The Lancet Neurology*, *12*(4), pp.357-367.
221. Wälti, M.A., Ravotti, F., Arai, H., Glabe, C.G., Wall, J.S., Böckmann, A., Güntert, P., Meier, B.H. and Riek, R., 2016. Atomic-resolution structure of a disease-relevant Aβ (1–42) amyloid fibril. Proceedings of the National Academy of Sciences, 113(34), pp.E4976-E4984.
222. Wang, J., Wang, W., Kollman, P.A. and Case, D.A., 2006. Automatic atom type and bond type perception in molecular mechanical calculations. *Journal of molecular graphics and modelling*, *25*(2), pp.247-260.
223. Wang, J.C. and Lin, J.H., 2013. Scoring functions for prediction of protein-ligand interactions. Current pharmaceutical design, 19(12), pp.2174-2182.
224. Wang, X., Wang, W., Li, L., Perry, G., Lee, H.G. and Zhu, X., 2014. Oxidative stress and mitochondrial dysfunction in Alzheimer's disease. *Biochimica et Biophysica Acta (BBA)-Molecular Basis of Disease*, *1842*(8), pp.1240-1247.

225. Wei, D.Q., Ma, Y., Cho, W.C., Xu, Q. and Zhou, F. eds., 2017. *Translational Bioinformatics and Its Application*. Springer.
226. Weingarten, M.D., Lockwood, A.H., Hwo, S.Y. and Kirschner, M.W., 1975. A protein factor essential for microtubule assembly. *Proceedings of the National Academy of Sciences*, *72*(5), pp.1858-1862.
227. West, L.A., Cole, S., Goodkind, D. and He, W., 2014. 65+ in the United States: 2010. *US Census Bureau*, pp.23-212.
228. Wimo, A., Jonsson, L. and Winblad, B., 2006. An estimate of the worldwide prevalence and direct costs of dementia in 2003. *Dementia and geriatric cognitive disorders*, *21*(3), pp.175-181.
229. Wimo, A., Jönsson, L., Bond, J., Prince, M., Winblad, B. and International, A.D., 2013. The worldwide economic impact of dementia 2010. *Alzheimer's & Dementia*, *9*(1), pp.1-11.
230. Wischik, C.M., Edwards, P.C., Lai, R.Y., Roth, M. and Harrington, C.R., 1996. Selective inhibition of Alzheimer disease-like tau aggregation by phenothiazines. *Proceedings of the National Academy of Sciences*, *93*(20), pp.11213-11218.
231. Wischik, C.M., Harrington, C.R. and Storey, J.M., 2014. Tau-aggregation inhibitor therapy for Alzheimer's disease. *Biochemical pharmacology*, *88*(4), pp.529-539.
232. Xiao, Y., Ma, B., McElheny, D., Parthasarathy, S., Long, F., Hoshi, M., Nussinov, R. and Ishii, Y., 2015. Aβ (1–42) fibril structure illuminates self-recognition and replication of amyloid in Alzheimer's disease. Nature structural & molecular biology, 22(6), p.499.
233. Yoon, S.S. and Jo, S.A., 2012. Mechanisms of amyloid-β peptide clearance: potential therapeutic targets for Alzheimer's disease. *Biomolecules & therapeutics*, *20*(3), p.245.
234. You, W., Tang, Z. and Chang, C.E.A., 2019. Potential mean force from umbrella sampling simulations: what can we learn and what is missed?. Journal of chemical theory and computation, 15(4), pp.2433-2443.
235. Yuriev, E., Agostino, M. and Ramsland, P.A., 2011. Challenges and advances in computational docking: 2009 in review. *Journal of Molecular Recognition*, *24*(2), pp.149-164.
236. Zerroug, A., Belaidi, S., BenBrahim, I., Sinha, L. and Chtita, S., 2018. Virtual screening in drug-likeness and structure/activity relationship of pyridazine derivatives as Anti-Alzheimer drugs. Journal of King Saud University-Science.
237. Zhang, B., Carroll, J., Trojanowski, J.Q., Yao, Y., Iba, M., Potuzak, J.S., Hogan, A.M.L., Xie, S.X., Ballatore, C., Smith, A.B. and Lee, V.M.Y., 2012. The microtubule-stabilizing agent, epothilone D, reduces axonal dysfunction, neurotoxicity, cognitive deficits, and Alzheimer-like pathology in an interventional study with aged tau transgenic mice. *Journal of Neuroscience*, *32*(11), pp.3601-3611.
238. Zhu, C.W. and Sano, M., 2006. Economic considerations in the management of Alzheimer's disease. *Clinical interventions in aging*, *1*(2), p.143.
239. Zimbone, S., Monaco, I., Gianì, F., Pandini, G., Copani, A.G., Giuffrida, M.L. and Rizzarelli, E., 2018. Amyloid Beta monomers regulate cyclic adenosine monophosphate response element binding protein functions by activating type-1 insulin-like growth factor receptors in neuronal cells. *Aging cell*, *17*(1), p.e12684.
240. Zvěřová, M., 2019. Clinical aspects of Alzheimer's disease. *Clinical biochemistry*.

Appendices

Appendix 1: Vina script example Dock A (2MXU)

```
receptor = /home/onke/docking/receptors/2mxu_model2.pdbqt

ligand = /home/onke/docking/SANCDB_compounds/findBestLigand_and_all.pdbqtTO.pdbqt

out = 2mxu_model2findBestLigand_and_all.pdbqtTO.all.pdbqt

log = 2mxu_model2findBestLigand_and_all.pdbqtTO.log

center_x = 7.417

center_y = 0.177

center_z = 0.112

size_x = 22

size_y = 22

size_z = 22

energy_range = 4

exhaustiveness = 128

cpu = 4
```

Appendix 2: Vina script example Dock B (2BEG)

```
receptor = /home/onke/docking/receptors/2beg_model1.pdbqt

ligand = /home/onke/docking/SANCDB_compounds/findBestLigand_and_all.pdbqtTO.pdbqt

out = 2beg_model1findBestLigand_and_all.pdbqtTO.all.pdbqt

log = 2beg_model1findBestLigand_and_all.pdbqtTO.log

center_x = 13.859

center_y = 0.0965

center_z = -0.463

size_x = 22

size_y = 22

size_z = 22

energy_range = 4

exhaustiveness = 128

cpu = 4
```

Appendix 3: Vina script example Dock C (2NAO)

```
receptor = /home/onke/docking/receptors/2nao_model1.pdbqt
```

```
ligand = /home/onke/docking/SANCDB_compounds/findBestLigand_and_all.pdbqtTO.pdbqt

out = 2nao_model1findBestLigand_and_all.pdbqtTO.all.pdbqt

log = 2nao_model1findBestLigand_and_all.pdbqtTO.log

center_x = 10.78

center_y = 17.975

center_z = -35.945

size_x = 22

size_y = 22

size_z = 22

energy_range = 4

exhaustiveness = 128

cpu = 4
```

Appendix 4: Vina script example Dock D (new-2NAO)

```
receptor = /home/onke/docking/receptors/new-2nao_model2.pdbqt

ligand = /home/onke/docking/SANCDB_compounds/findBestLigand_and_all.pdbqtTO.pdbqt

out = new-2nao_model2findBestLigand_and_all.pdbqtTO.all.pdbqt

log = new-2nao_model2findBestLigand_and_all.pdbqtTO.log

center_x = 12.057

center_y = 18.041

center_z = -35.901

size_x = 22

size_y = 22

size_z = 22

energy_range = 4

exhaustiveness = 128

cpu = 4
```

Appendix 5: List of colours for docking figures analysis

Interactions	**Colour Name**
Alkyl	Cotton candy
Attractive charge	Orange peel
Carbon hydrogen bond, halogen	Honeydew
Carbon-hydrogen bond	Honeydew
Conventional hydrogen bond	Lime
Halogen	Aqua
Metal-acceptor	Light grey

π-alkyl	Cotton candy
π-anion	Orange peel
π-cation	Orange peel
π-donor hydrogen bond	Honeydew
π-π stacked	Neon pink
π-π T shaped	Neon pink
π-sigma	Heliotrope
π-Sulphur	Tangerine yellow
Salt bridge	Orange peel
Unfavorable acceptor-acceptor	Red
Unfavorable donor-donor	Red
Unfavorable positive-positive	Red

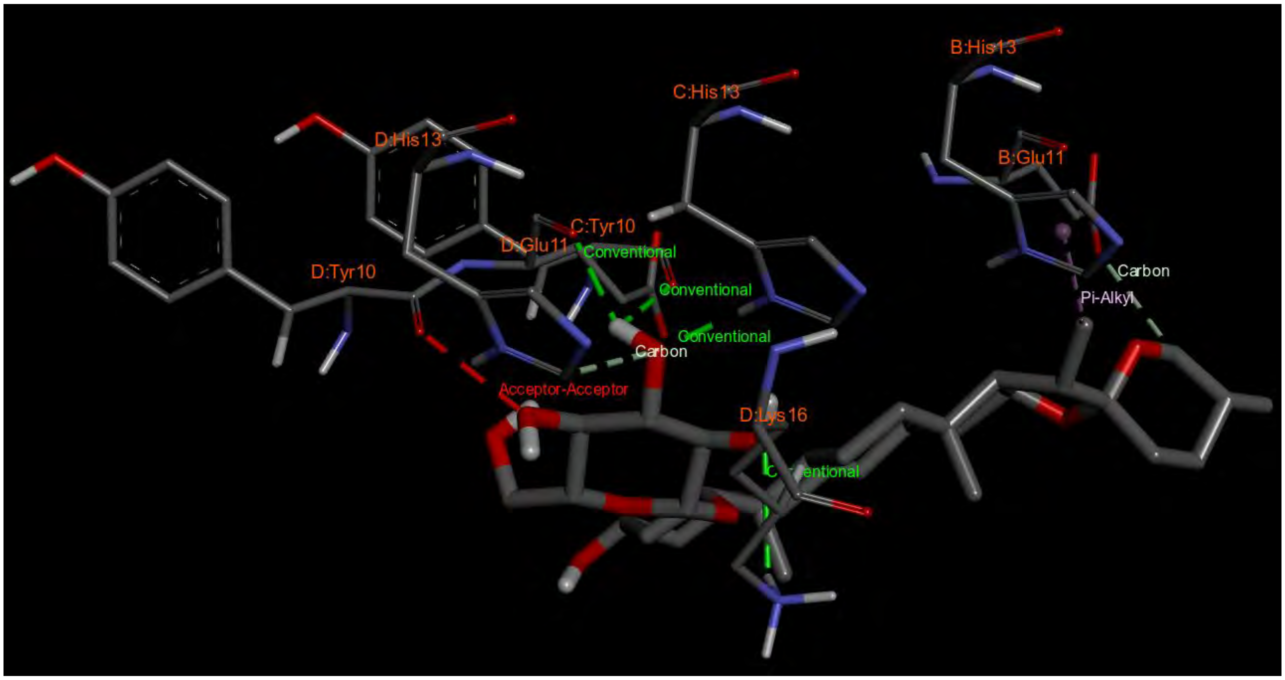

Figure 1: Dock D (new-2NAO), the interactions with SANC00407.

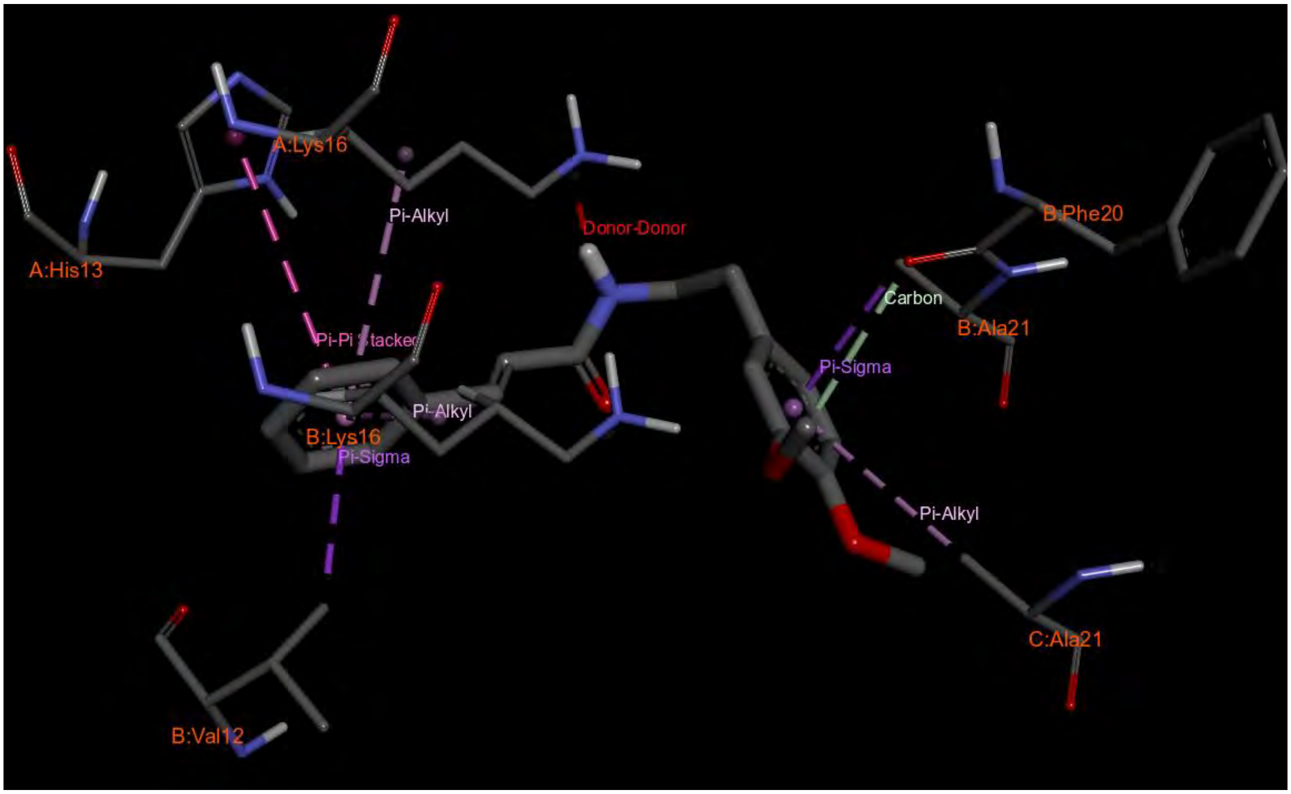

Figure 2: 2NAO and wgx-50 interactions.

Appendix 6: Periodic boundary conditions and rotation matrix script

```python
# Reading in the PDB file
pdbread = open("2beg.pdb")
pdbread_info = pdbread.readlines()
pdbread.close()
#Only read lines that start with ATOM and contain the alpha carbon
all_coord = []
for line in pdbread_info:
    if line.startswith("ATOM"):
        if line.__contains__("CA"):
            new_line = str.split(line)
            all_coord.append(new_line[6:9])
#Convert all coordinates from strings to float values and group the chains A-D with their corresponding coordinates
new_coord_A = []
coord_A = all_coord[0:26]
for a in coord_A:
    coord_A = list(map(float, a))
```

```python
    new_coord_A.append(coord_A)
new_coord_B = []
coord_B = all_coord[26:52]
for b in coord_B:
    coord_B = list(map(float, b))
    new_coord_B.append(coord_B)
new_coord_C = []
coord_C = all_coord[52:78]
for c in coord_C:
    coord_C = list(map(float, c))
    new_coord_C.append(coord_C)
new_coord_D = []
coord_D = all_coord[78:104]
for d in coord_D:
    coord_D = list(map(float, d))
    new_coord_D.append(coord_D)
new_coord_E = []
coord_E = all_coord[104:130]
for e in coord_E:
    coord_E = list(map(float, e))
    new_coord_E.append(coord_E)
# Subtracting atom coordinates in chain A with those in chain B, till F. Such that coordinates of 1st atom in chain A minus 1st atom in chain B
vector1 = []
for j in range(len(new_coord_A)):
    a = new_coord_A[j]
    b = new_coord_B[j]
    b_minus_a = [b[0]-a[0],b[1]-a[1],b[2]-a[2]]
    vector1.append(b_minus_a)
vector2 = []
for n in range(len(new_coord_B)):
    b = new_coord_B[n]
    c = new_coord_C[n]
    c_minus_b = [c[0]-b[0],c[1]-b[1],c[2]-b[2]]
    vector2.append(c_minus_b)
```

```
vector3 = []
for k in range(len(new_coord_C)):
    c = new_coord_C[k]
    d = new_coord_D[k]
    d_minus_c = [d[0]-c[0],d[1]-c[1],d[2]-c[2]]
    vector3.append(d_minus_c)
vector4 = []
for m in range(len(new_coord_D)):
    d = new_coord_D[m]
    e = new_coord_E[m]
    e_minus_d = [e[0]-d[0],e[1]-d[1],e[2]-d[2]]
    vector4.append(e_minus_d)
# Take the average of each vector, such that ave of coordinate x, y, z are produced for the five vectors
x_coor = []
y_coor = []
z_coor = []
for k in vector1:
    x_coor.append(k[0])
    y_coor.append(k[1])
    z_coor.append(k[2])
    sum_x = sum(x_coor)/len(vector1)
    sum_y = sum(y_coor)/len(vector1)
    sum_z = sum(z_coor)/len(vector1)
ave_coor1 = [sum_x,sum_y,sum_z]
x_coor = []
y_coor = []
z_coor = []
for k in vector2:
    x_coor.append(k[0])
    y_coor.append(k[1])
    z_coor.append(k[2])
    sum_x = sum(x_coor)/len(vector2)
    sum_y = sum(y_coor)/len(vector2)
    sum_z = sum(z_coor)/len(vector2)
```

```
ave_coor2 = [sum_x,sum_y,sum_z]

x_coor = []

y_coor = []

z_coor = []

for k in vector3:

    x_coor.append(k[0])

    y_coor.append(k[1])

    z_coor.append(k[2])

sum_x = sum(x_coor)/len(vector3)

sum_y = sum(y_coor)/len(vector3)

sum_z = sum(z_coor)/len(vector3)

ave_coor3 = [sum_x,sum_y,sum_z]

x_coor = []

y_coor = []

z_coor = []

for k in vector4:

    x_coor.append(k[0])

    y_coor.append(k[1])

    z_coor.append(k[2])

    sum_x = sum(x_coor)/len(vector4)

    sum_y = sum(y_coor)/len(vector4)

    sum_z = sum(z_coor)/len(vector4)

ave_coor4 = [sum_x,sum_y,sum_z]

# Calculating the unit vector for each of the average vectors and the angle they produce
with ox vector which is given by the xyz coordinates (1.0, 0.0, 0.0)

import math

import numpy.matlib

import numpy as np

norm1 = math.sqrt((ave_coor1[0]**2 + ave_coor2[1]**2 + ave_coor1[2]**2))

unit_vector1 = [ave_coor1[0]/norm1,ave_coor1[1]/norm1,ave_coor1[2]/norm1]

vector_ox = [1.0, 0.0, 0.0]

ab_ox = np.dot(unit_vector1,vector_ox)

angle_ab_ox = math.degrees(math.acos(ab_ox))

norm2 = math.sqrt((ave_coor2[0]**2 + ave_coor2[1]**2 + ave_coor2[2]**2))

unit_vector2 = [ave_coor2[0]/norm2,ave_coor2[1]/norm2,ave_coor2[2]/norm2]
```

```
bc_ox = np.dot(unit_vector2,vector_ox)

angle_bc_ox = math.degrees(math.acos(bc_ox))

norm3 = math.sqrt((ave_coor3[0]**2 + ave_coor3[1]**2 + ave_coor3[2]**2))

unit_vector3 = [ave_coor3[0]/norm3,ave_coor3[1]/norm3,ave_coor3[2]/norm3]

cd_ox = np.dot(unit_vector3,vector_ox)

angle_cd_ox = math.degrees(math.acos(cd_ox))

norm4 = math.sqrt((ave_coor4[0]**2 + ave_coor4[1]**2 + ave_coor4[2]**2))

unit_vector4 = [ave_coor4[0]/norm4,ave_coor4[1]/norm4,ave_coor4[2]/norm4]

de_ox = np.dot(unit_vector4,vector_ox)

angle_de_ox = math.degrees(math.acos(de_ox))

# The averages of all vector sizes

all_norm = [norm1,norm2,norm3,norm4]

ave_norm = sum(all_norm)/len(all_norm)

# The perpendicular vector about the ox vector (1.0, 0.0, 0.0) for all the average vectors

perp_ab_ox = np.cross(unit_vector1,vector_ox)

perp_bc_ox = np.cross(unit_vector2,vector_ox)

perp_cd_ox = np.cross(unit_vector3,vector_ox)

perp_de_ox = np.cross(unit_vector4,vector_ox)

# The average of a unit vectors

all_vectors = [perp_ab_ox,perp_bc_ox,perp_cd_ox,perp_de_ox]

x_vector = []

y_vector = []

z_vector = []

for k in all_vectors:

    x_vector.append(k[0])

    y_vector.append(k[1])

    z_vector.append(k[2])

sum_x = sum(x_vector)/len(all_vectors)

sum_y = sum(y_vector)/len(all_vectors)

sum_z = sum(z_vector)/len(all_vectors)

ave_vector = [sum_x,sum_y,sum_z]

ave_vector_size=np.linalg.norm(ave_vector)

ave_vector=ave_vector/ave_vector_size

# The average of all angles

all_angles = [angle_ab_ox,angle_bc_ox,angle_cd_ox,angle_de_ox]
```

```
ave_angle = -sum(all_angles)/len(all_angles)

# Producing Rotation matrix from average unit vector and average angle

rad= math.pi/180

a11 = ((math.cos(ave_angle*rad))+((ave_vector[0]**2)*(1-math.cos(ave_angle*rad))))

a12 = ((ave_vector[0]*ave_vector[1])*(1-math.cos(ave_angle*rad))-
((ave_vector[2])*(math.sin(ave_angle*rad))))

a13 = ((ave_vector[0]*ave_vector[2])*(1-
math.cos(ave_angle*rad))+((ave_vector[1])*(math.sin(ave_angle*rad))))

a21 = ((ave_vector[1]*ave_vector[0])*(1-
math.cos(ave_angle*rad))+((ave_vector[2])*(math.sin(ave_angle*rad))))

a22 = ((math.cos(ave_angle*rad))+((ave_vector[1]**2)*(1-math.cos(ave_angle*rad))))

a23 = ((ave_vector[1]*ave_vector[2])*(1-math.cos(ave_angle*rad))-
((ave_vector[0])*(math.sin(ave_angle*rad))))

a31 = ((ave_vector[2]*ave_vector[0])*(1-math.cos(ave_angle*rad))-
((ave_vector[1])*(math.sin(ave_angle*rad))))

a32 = ((ave_vector[2]*ave_vector[1])*(1-
math.cos(ave_angle*rad))+((ave_vector[0])*(math.sin(ave_angle*rad))))

a33 = ((math.cos(ave_angle*rad))+((ave_vector[2]**2)*(1-math.cos(ave_angle*rad))))

rotation_axis = [[a11,a12,a13],[a21,a22,a23],[a31,a32,a33]]

# Determining the rotation axis matrix determinat

b = np.array(rotation_axis)

det_rotation_axis = np.linalg.det(b)

# Divide the all the elements of the matrix by det_rotation_axis, so that the determinat
becomes 1

new_rotation_axis = []

for i in rotation_axis:

    new_rotation_axis.append(i/det_rotation_axis)

# The determinate of the new rotation axis determinat

new_det_rotation_axis = np.linalg.det(new_rotation_axis)
```

Appendix 7: Perl script PDB residue renumbering

```
#!/usr/bin/perl

my $firstatom=1;

my $firstresidue=1;

open(PDB,"< new-2nao.pdb");

open(PDBOUT,"> new-2nao_fxd.pdb");

my $atomnumber=$firstatom-1;

my $residuedifference=-1;

while(my $line = <PDB>)
```

```
{
   #print $line;
   if($line =~ m/ATOM/)
   {

   $atomnumber++;

#0        1         2         3         4         5         6         7         8
#12345678901234567890123456789012345678901234567890123456789012345678901234567890
#ATOM   1573  N   ALA A 211       7.208  20.043  54.197  1.00 60.93           N
#ATOM      2  CA  GLU F   1      -1.561   9.600 -19.812  1.00  0.00           C
#first part
#ATOM   1573  N   ALA A
#last part
#       7.208  20.043  54.197  1.00 60.93           N
#middle part
#211
   my $firstl=substr $line, 0,6;
   my $atno=substr $line,6,5;
   my $firstr=substr $line, 11,11;
   my $last=substr $line, 26, 1000;
   my $middle=substr $line, 22,4;
   if($residuedifference eq -1)
   {
      $residuedifference = $firstresidue-$middle;
   }
#   print "*$firstl*$atno*$firstr*$middle*$last";
   $middle += $residuedifference;
   my $resstring =sprintf("%4d",$middle);
   my $atomstring=sprintf("%5d",$atomnumber);
   print PDBOUT "$firstl$atomstring$firstr$resstring$last";
   print "$firstl$atomstring$firstr$resstring$last";
#   print PDBOUT $first;
#   printf PDBOUT "%4d",$middle;
#   print PDBOUT $last;
```

```
      ###need to number the thing correctly
    }
    else
    {
      print PDBOUT $line;
    }
}
close PDB;
close PDBOUT;
```

Appendix 7: Perl script PDB residue renumbering

```
* Minimize PDB
*
! read topology and parameter files
read rtf card flex name /home/onke/toppar/top_all36_prot.rtf
read param card flex name /home/onke/toppar/par_all36_prot.prm
stream toppar/toppar_water_ions.str
! read the psf and coordinate file
read psf card name /home/onke/neutralized_output/2mxu/2mxu-neutralized_cu.psf
read coor card name /home/onke/neutralized_output/2mxu/2mxu-neutralized_cu.crd
!patch segid resid segid resid
patch coppa COPP 3 CHAIN_G 35 noangle nodihedral
patch coppb COPP 3 CHAIN_H 67 noangle nodihedral
! set up SHAKE again
shake bonh param sele all end
! set up crystal and images
!set greaterval = 50.9261
!crystal define rhdo @greaterval @greaterval @greaterval 60. 90. 60.
crystal define orth 19.45 60.0 60.0 90.0 90.0 90.0
crystal build noper 0
! These segments are used for water and ions in bulk solvent
define bulks sele segid bwat .or. segid pot .or. segid cl .or. segid sod .or. -
  segid cal .or. segid mg .or. segid ces end
```

```
! You may need to change these depending on how you plan to do recentering

image byseg sele .not. resname tip3 .and. .not. bulks end

image byres sele resname tip3 .or. bulks end

! the total charge on the system must be 0 or else Ewald will not work correctly, we need
to test for this...

! we do the almost equal if test to avoid floating point rounding errors.

scalar charge stat sele all end

if ?stot .ae. 0 then goto okewald

! uh-oh, total charge != 0, we cannot proceed, set the bomlev to an absurdly high level

! to force a bailout.

bomlev 5

Achtung, particle-mesh ewald only works correctly on a structure with 0 total charge!!!!

label okewald

! set up nonbond correctly to the same values we will be using in dynamics

nbond inbfrq -1 imgfrq -1 -

      elec ewald pmew fftx 48 ffty 48 fftz 48 kappa .34 spline order 6 -

      vdw vswitch cutnb 16. cutim 16. ctofnb 12. ctonnb 10.

energy

coor copy comp

mini sd nstep 200

mini abnr nstep 1000 nprint 100 tolg 0.01

coor rms

ioform extended

write psf card name final_minimization_output/2mxu/2mxu-finalmini_cu_patch2.psf

* psf with additional constraints

*

write coor card name final_minimization_output/2mxu/2mxu-finalmini_cu_patch2.crd

* Final minimized coordinates, done with PME

*

write coor pdb card name final_minimization_output/2mxu/2mxu-finalmini_cu_patch2.pdb

* final minimization pdb

*

stop
```